Aus dem Lehrstuhl für Experimentelle Ultrahochfeld Magnet Resonanz
der Medizinischen Fakultät Charité – Universitätsmedizin Berlin

DISSERTATION

Studies on a Preclinical Model of Brain Autoimmunity using Emerging Magnetic Resonance Methods

zur Erlangung des akademischen Grades

Doctor rerum medicinalium (Dr. rer. medic.)

vorgelegt der Medizinischen Fakultät
Charité – Universitätsmedizin Berlin

von

Stefano Lepore

aus Trieste

Datum der Promotion: 04.09.2015

Table of contents

Zusammenfassung

Entzündungserkrankungen des zentralen Nervensystems (ZNS) wie Multiple Sklerose und Akute disseminierte Enzephalomyelitis sind verbunden mit der Aktivierung und Einwanderung von Immunzellen in das ZNS, was letztlich zu Demyelinisierung der weißen Gehirnsubstanz, Neurodegeneration und Entwicklung von neurologischen Symptomen führt. Eine klinische Diagnose wird jedoch oft erst gestellt, wenn neurodegenerative Prozesse bereits im Gange sind. In dieser Arbeit wurden drei Studien unter Einsatz modernster Methoden der Magnetresonanz (MR) im Experimentelle Autoimmun Enzephalomyelitis (EAE) Tiermodell durchgeführt, um die zugrunde liegenden Pathologien der ZNS-Entzündung zu untersuchen. Ziel der ersten Studie war es, Frühindikatoren der Krankheit ausfindig zu machen. Durch Verwendung kryogener Hochfeld (HF)-Spulen bei der *in vivo* MR-Bildgebung mit hervorragender räumlicher Auflösung im Mikrometer Bereich (μMRI) war es möglich, Gehirnpathologien als mikroskopische Veränderungen im Gehirnparenchym zu enthüllen. Durch μMRI wurden Läsionen als hyper- und hypo-intensive Regionen noch vor dem Auftreten klinischer Symptome enttarnt. Die Läsionen wurden im Kleinhirn (lat. Cerebellum) der weißen Substanz und im Cortex beobachtet, und deuten auf Immunzellinfiltration hin, was durch konventionelle Histologie bestätigt wurde. In der zweiten Studie wurden die zeitlichen und räumlichen Verteilungen der Gehirnveränderungen aus der vorherigen Studie während der Entwicklung von EAE systematisch untersucht. Durch die kryogen-gekühlte Empfangsspulen-Technologie war es möglich die Akquisitionszeit soweit zu reduzieren, dass eine große Anzahl von EAE-Mäusen untersucht werden konnte. Diese Studie offenbarte eine signifikante Vergrößerung des Ventrikels und eine Zunahme von freiem Wasser in die Liquor cerebrospinalis noch bevor sich die Krankheit klinisch bemerkbar macht. Abgesehen von diesen makroskopischen Veränderung zeigte diese Studie, dass sich mikroskopische Läsionen, die üblicherweise im Cerebellum beobachtet werden, schon vor Beginn der Erkrankung bemerkbar machen. Die Daten zeigten, dass eine frühzeitige Veränderungen der Ventrikelgröße und das Auftreten von Läsionen während der Autoimmunität im Gehirn ein Frühindikator sein könnte, noch bevor sich ein neurologisches Krankheitsbild herausbildet, was eine zusätzliche Untersuchung in präklinischen und klinischen Studien erforderlich macht. In der dritten Studie wurde die Dynamik der Entzündungszellen zwischen dem zentralen Nervensystem und dem lymphatischen System während der EAE-Ausbildung untersucht. Die Art und Weise der Immunzellinfiltration während der Gehirnentzündung wurde anhand einer neuartigen Fluor / Proton (^{19}F / ^{1}H) MR Neuro-

Bildgebungstechnik und der Verwendung von fluoreszierenden ^{19}F Nanopartikeln untersucht. In dieser Studie war es möglich, Änderungen in der Migration der Entzündungszellen durch Veränderungen des Fluorsignals in den ableitenden Lymphknoten und in den Entzündungsregionen des ZNS, wie Kleinhirn, Hirnstamm und Cortex, über einen ausgedehnten Zeitraum zu detektieren.

Abstract

Central nervous system (CNS) inflammatory disorders such as multiple sclerosis and acute disseminated encephalomyelitis are associated with the recruitment and invasion of immune cells into the CNS that ultimately leads to white matter demyelination, neurodegeneration and development of neurological symptoms. A clinical diagnosis is often made when neurodegenerative processes are already ongoing. In this work three main studies employing state-of-the-art Magnetic Resonance (MR) methods were performed in the animal model Experimental Autoimmune Encephalomyelitis (EAE), in order to study the underlying pathologies of CNS inflammation. In the first study, the goal was to seek early indicators of disease. By employing cryogenically-cooled RF coils to acquire micro MR imaging (μMRI) *in vivo*, with superior spatial resolution, it was possible to reveal brain pathology as microscopic changes in the brain parenchyma. μMRI revealed lesions as hyper-intense and hypo-intense regions, before the appearance of clinical symptoms. The lesions were observed in the cerebellum white matter and the cortex and were suggestive of immune cell infiltration as demonstrated by conventional histology. In the second study, the temporal and spatial distributions of brain modifications observed in the previous study were systematically investigated during inflammation throughout the development of EAE. Thanks to the reduced scan time achieved using the cryogenically-cooled coil technology it was possible to follow a large cohort of EAE mice. This study revealed significant enlargement in ventricle size and an increase in free water content within the cerebrospinal fluid (CSF) prior to disease clinical manifestation. Apart from this macroscopic change, this study demonstrated that microscopic lesions commonly observed in the cerebellum also became evident prior to disease onset. The data suggested that early changes in ventricle size and lesion presentation during brain autoimmunity could be an indicator of the events preceding neurological disease manifestation and necessitate additional exploration in preclinical and clinical studies. In the third study, the dynamics of inflammatory cells between central nervous system and lymphatic system were investigated during development of EAE. The nature of immune cell infiltration during brain inflammation was studied by a novel Fluorine/Proton ($^{19}F/^{1}H$) MR neuroimaging technique and application of fluorescently-tagged ^{19}F nanoparticles. In this study it was possible to detect changes in inflammatory cell migration over an extensive period of time by changes in the fluorine signal within the draining lymph nodes and regions of inflammation in CNS such as cerebellum, brain stem and cortex.

1. Introduction

Multiple Sclerosis (MS) is an inflammatory disorder of the Central Nervous System (CNS) caused by a chronic demyelination of axons in the brain and spinal cord. In Europe MS prevalence ranges from 20-200 per 100.000 and likewise the incidence varies between 10-100 per 100.000 depending on the European region, with a higher prevalence in women (2:1) [1]. MS is thought to be the result of a combination of different environmental factors (such as viruses, stress and dietary changes) that act in concurrence with genetic susceptibility to turn on the inflammatory response against self-antigenic determinants expressed in the CNS and result in multiple neurological dysfunctions (e.g. limb weakness, visual and sensory disability, bowel symptoms).

That MS is an autoimmune syndrome is corroborated by animal models studies indicating that autoreactive T cells can cause an inflammatory demyelination of CNS. These animal studies have implicated one or more myelin antigens in brain and spinal cord. Experimental autoimmune encephalomyelitis (EAE) is an inflammatory demyelinating disease of the CNS that can be induced in a number of species (e.g. rodents and primates) and is used as a model for the human CNS demyelinating disease since it shares clinical and pathological features with MS [2]. Commonly EAE is induced by immunization with one of a number of myelin antigens emulsified in complete Freund's adjuvant [3] or by transfer of effector T helper cells [4] in susceptible mouse strains. A widely used strain is the SJL/J; a relapsing/remitting form of EAE can be induced in these mice nine to thirteen days following immunization with the myelin proteolipid protein ($PLP_{139-151}$) peptide [3].

Under normal physiological conditions, the CNS is protected against potentially harmful intruders by immunologically competent CNS resident cells, such as microglia, or immune cells derived from the peripheral circulation; blood-borne immune cells, including memory T cells, are limited to the leptomeningeal, perivascular and ventricular CSF spaces [5]. The events that lead to MS lesion formation involve the invasion of activated CNS specific immune cells from the peripheral vascular compartment into the brain parenchyma resulting in tissue damage; this is best depicted by the presence of demyelinating lesions and plaques commonly located in the white matter, mostly periventricular, and in leukocortical, juxtacortial and cortical regions [6].

Organ-specific autoimmune diseases such as MS are thought to be mediated by T helper cells (T_H) which activate macrophages [7]. Naïve T_H cells ($CD4^+$ T cells) mature after interaction of their T cell receptor with antigen bound on the MHC II receptor of antigen presenting cells (APC). After

activation, T_H cells undergo proliferation and differentiation into several lineages of effector T_H cells, including encephalitogenic T_H17, which stimulate and interact with other leukocytes including regulatory T cells. The residual cell population will persist as long-living memory T_H cells [8]. In the healthy brain, immune cell such as memory T_H cells appear to be limited to the CSF compartment [5]. For this reason it was eventually assumed that the CSF compartment has a fundamental role for immune surveillance and is the place where activated T cells can interact with resident antigen-presenting cells during neuroinflammatory disease [9]. Memory T_H cells reach the CSF compartment by means of their extravasation via microvascular structures of the choroid plexus into the cerebral ventricles or alternatively via postcapillary venules into leptomeningeal and perivascular Virchow–Robin (VRS) spaces [10]. Inflammation and demyelination of white matter imply the entry of immune cells in the CNS. Two different studies showed that two waves of migratory T_H cells invading the CNS could exist. The first wave of T cells is through the choroid plexus, via the blood CSF barrier (BCSFB), leading to effector T_H cell (T_H17) restimulation by antigen in the subarachnoid space, early CNS inflammation and stimulation of the blood brain barrier vasculature. This activation triggers the second wave where a larger number of inflammatory cells invade the CNS parenchyma via their migration through the blood brain barrier (BBB) [11].

EAE has also been a necessary tool for the identification of new therapeutic compounds for MS, some of the therapies discovered through the model are established treatments for MS [12]. Particularly the discovery of antibodies against $\alpha 4\beta$l integrin (VLA-4) in EAE preventing traffic of mononuclear leukocytes across the vascular endothelium of the CNS through the inhibition of activated lymphocytes adhesion to brain blood vessels [13] has been shown to induce a rapid and sustained reduction in disease activity in MS [14] and this therapy is now FDA-approved.

The diagnosis of MS is usually based on the McDonald criteria. Accordingly, patients with a first clinical episode suggestive of MS (Clinically Isolated Syndrome or CIS) will be diagnosed with clinically definitive MS if the initial MRI findings fulfill the criteria for both dissemination in space and time [15]. However, a definitive diagnosis is based on a number of different clinical tools, including cerebrospinal fluid analysis for the identification of oligoclonal bands [16] and evoked potential testing [17]. MRI is becoming a common tool not only for diagnosing MS but also for follow-up studies and for defining endpoints when studying response to therapy in individual patients [18]. Although MR is a strong tool in the diagnosis, prognosis and therapeutic outcome of

MS, more reliable and robust image analysis methods are still needed to understand and fully exploit the amount of information that can be generated [19]. Animal models of brain inflammation are therefore also invaluable as benchmarks for new MRI technologies that could become clinical routine in the future.

In animal models of MS, MRI has been employed for several years to study non-invasively the progression of encephalomyelitis, particularly in association with anti-inflammatory treatment studies [20, 21] but also to identify signatures between different pathological lesions [22] and different anatomical regions of the CNS [23].

Although preclinical MRI has been valuable to study specific pathologies during brain autoimmunity, limitations in the technology exist. The most predominant problem is the anatomical dimensions of the typical animal species studied, which intrinsically restricts the achievable spatial resolution. By increasing the resolution to achieve a quality comparable to human MR imaging, a decrease in signal to noise ratio (SNR) is to be expected because of the reduced voxel size. To overcome this drawback averaging is necessary; this considerably increases scan time and ultimately limits the thoroughness of the study (i.e. frequency of MR scans per animal or number of animals per study). These limitations for small animal MRI, as well as those shared with human MRI (motion artifacts, field inhomogeneity at higher magnetic field strengths), represent major challenges for the execution of more intensive MR studies in animal models of disease.

Recently, cryogenically-cooled proton (^{1}H) coils have started gaining momentum in preclinical MR studies due to a boosted signal-to-noise ratio (SNR) compared to traditional room temperature ^{1}H coils [24]. With these coils µMRI can be achieved at reasonable scan times; µMRI is defined as MRI with a spatial resolution <100 µm. Coil resistance and therefore thermal noise are reduced due to coil cooling. The resulting SNR increase compares to an increase in the magnetic field (B_0) strength by a factor of at least 2, without the problems associated with higher B_0 strengths such as shorter wavelengths, B_1 and B_0 inhomogeneities and susceptibility artifacts.

Another emerging use of MRI is immune cell tracking in the lymphatic system and inflamed organs. Using nanoparticles rich in fluorine (^{19}F) – as MR active nucleus – it is possible to label cells and locate them with virtually background free signal due to the negligible endogenous presence of ^{19}F in the body. Fluorine compounds are commonly used in biomedical application e.g. as oxygen

carriers; usually these are synthetic chemically-inert perfluorocarbons (PFCs) that are insoluble in water and need to be emulsified for clinical use. The ^{19}F particles achieved by emulsification range from 100 nm to some hundreds nanometers. Since nanoparticles are easily taken up by cells of the mononuclear phagocyte system such as dendritic cells and macrophages [25], it is possible to detect ^{19}F signal in regions of inflammation and draining lymph nodes (LNs). Therefore ^{19}F nanoparticles in combination with $^{19}F/^{1}H$ MR methods have been used to study several models of inflammation such as post ischemia inflammation [26] and also to track immune cell types [27].

The goal of this work was to make good use of the above novel technologies and evolving MR methods to further understand the evolution of brain autoimmunity during EAE particularly the early stages of the pathophysiology. For this, both μMRI and ^{19}F MRI were implemented to study the early processes of inflammation in the EAE. The cryogenic MR technology was used during the first study to acquire high resolved images of mouse brain EAE lesions (μMRI) in an amount of time suitable for *in vivo* preclinical longitudinal study. In this first study brain pathology was observed in areas (such as the cerebral cortex), not commonly detected by conventional MRI and an excellent correspondence between μMRI findings and conventional histology was demonstrated. In the second study, the goal was to exploit the major advantages of employing the cryogenically-cooled coil technology in EAE studies (increased image resolution and reduced scan time) to closely follow longitudinally changes, especially microscopic alterations, in the brain during EAE, with the ultimate aim of identifying pathological changes prior to and during commencement of disease. On a microscopic level the evolution of MR hyper and hypo-intense regions were observed prior to EAE clinical manifestation. Surprisingly the most interesting finding of the second study was a macroscopic change; a prominent increase in ventricle volume was detected prior to disease onset and in parallel to an increase in T_2 relaxation time of CSF. The cryogenically-cooled technology permitted a significant reduction in acquisition time, thereby enabling closer and more critical observations of changes (that were otherwise previously concealed by conventional MR methods) in brain pathology during EAE.

The results of the first two studies were a precursor to my motivation to study immune cell trafficking into CNS during the development of EAE. For this, the evolving technologies around ^{19}F were developed and employed. A dual-tunable radiofrequency probe for combined ^{19}F and ^{1}H MR was developed for mouse neuroimaging. Fluorescently-tagged fluorine nanoparticles were also

prepared in-house to label immune cells during the inflammatory process. With these technologies, the *in vivo* dynamics of inflammatory cells between CNS and lymphatic system could be studied during EAE development. Immune cell infiltrations were observed in regions that are otherwise not easily visualized by conventional probes due to limited signal depth penetration.

2. Methodology

2.1. Magnetic resonance related methods

MR methods were performed using a 9.4 Tesla horizontal magnet small animal scanner (Biospec 94/20 USR, Bruker Biospin, Ettlingen, Germany) with a bore diameter of 200 mm. The system is equipped with an actively-shielded water-cooled BGA12 gradient system, gradient amplitude 440 mT/m, with an integrated shim set up to second order. To accommodate for the animal experiments in the three studies the animal cradles for the different coil setups used were connected to an automatic positioning system (AutoPac, Bruker Biospin). The MR system runs on a Linux-based software for multidimensional MR data acquisition, reconstruction and visualization (ParaVision® 5.1, Bruker Biospin, Ettlingen, Germany).

a. Coil technologies

Two different technologies were used to study brain inflammation in EAE by MR methods. High resolution of the brain was achieved by means of a cryogenically-cooled ^{1}H coil (Bruker, Ettlingen, Germany). Brain inflammation was studied by means of a dual-tunable $^{19}F/^{1}H$ birdcage in house built coil (Sci Rep. 2013; 3:1280).

i. Cryogenically-cooled surface coil

For micro MRI of the mouse EAE brain a cryogenically-cooled proton (^{1}H) coil, a Transceiver Mouse Brain CryoProbe (CP, Bruker BioSpin, Ettlingen, Germany) was employed. The CryoProbe is a half-cylindrical-shaped 2-channel transmit/receive quadrature-driven surface coil, for full mouse-brain coverage with a maximum field of view of c. 30×20×20 mm. cooled by a closed-cycle refrigeration system and operating at around 30 K. The surface of the probe that is in direct contact with the animal head is maintained at 37° C via a resistive heater unit (Bruker, BioSpin AG, Fällanden, Switzerland) that monitors and regulates the temperature.

ii. $^{19}F/^{1}H$ dual-tunable birdcage coil

To study brain inflammation, a dual-tunable $^{19}F/^{1}H$ birdcage coil was constructed. The probe is composed of 32 copper strips arranged in parallel to form a cylinder and overlapping with peripheral strips connected together by the end rings of the RF coil. In this way there was no need of solid chip capacitors (thereby reducing susceptibility artifacts) because the design itself provided capacitance at each overlapping section. Moreover the selected geometry resulted in improved transmission field homogeneity. A recognized limitation with our coil design is that the birdcage cannot be driven in

quadrature and dual-tunable mode at the same time due to its small size, resulting in a lower SNR (-41%) compared to quadrature driven coils.

b. MR acquisition

A number of RF pulse programs available on ParaVision® 5.1 scanner software (Bruker, Ettlingen, Germany) were tailored to achieve different contrasts in order to highlight and detect brain inflammation in EAE. In MRI the signal is generated by the reaction of proton (^{1}H) to the combination of two magnetic fields: the external static magnetic field (B_0) and the alternating magnetic field (B_1) generated by the coil system. This signal changes in different tissues thereby producing boundaries and contrast. The most important properties of protons that influence the signal are the proton density (PD), the spin-lattice relaxation time (T_1) and the spin-spin relaxation time (T_2). T_1 and T_2 contrast are related to the relaxation phenomenon. Relaxation describes the processes that occur when a sample placed inside B_0 returns to its equilibrium state (i.e. the initial magnetization) after a RF pulse excitation. T_1 is the time constant for the recovery of magnetization along the direction of B_0 and T_2 is the time constant for the decay of magnetization in the plane perpendicular to B_0. Several pulse methods exist to highlight the signal of different tissues e.g. white matter and gray matter. To achieve this purpose it is necessary to determine various parameters in the imaging technique such as the repetition time (TR), the echo time (TE), the flip angle (FA) and the inversion time (TI).

i. MR Imaging

Pre and post contrast T_1 weighted (T_1W) imaging was performed using Modified Driven-Equilibrium Fourier Transformation (3D MDEFT: TR = 3000 ms, TE = 3.9 ms, FA 20°, TI = 950 ms, matrix 384 × 384). Horizontal sections: Time of acquisition (TA) = 11 min, spatial resolution = 47 × 47 × 400 μm^3. Coronal sections: TA = 15 min, spatial resolution = 47 × 47 × 500 μm^3. As T_1-enhancing contrast agent gadolinium diethylenetriamine penta-acetate (Gd-DTPA, Magnevist, Bayer-Schering Pharma AG, Berlin, Germany) was administered intravenously at a dose of 0.2 mmol/kg.

T_2 weighted (T_2W) scans were performed using Turbo Rapid Acquisition with Relaxation Enhancement (2D TurboRARE: TR = 3000 ms, TE = 43 ms, matrix 384×384, TA = 5 min) were performed with geometry and spatial resolution identical to that of T_1W imaging.

To image brain tissue in association with the microvasculature a T_2^* weighted (T_2^*W) multislice fast low angle shot method (2D FLASH: TR = 473 ms, TE = 18 ms, FA 40°, matrix 512 × 512) was applied using an in plane resolution of (35 × 35) μm^2. Horizontal sections: TA = 8 min, slice thickness = 400 μm. Coronal sections: TA = 11 min, slice thickness = 500 μm.

T_2^*W phase maps were processed in order to generate susceptibility weighted imaging (SWI). SWI generates a different contrast compared to T_1 or T_2 exploiting the magnetic susceptibility of tissues since their signal will become out of phase with tissues that possess a different susceptibility.

A gradient echo with flow compensation (GEFC-3D FLASH: TR = 30 ms, TE = 5.9 ms, matrix 512 × 256 × 256, TA = 29 min) was performed 1 hr after contrast injection at an isotropic spatial resolution of 59 μm. Since this method is typically used for MR angiography it was employed to visualize only the brain vasculature excluding the parenchyma.

To study brain inflammation by combined ^{19}F/^{1}H MRI 3D TurboRARE was employed. ^{1}H: TR = 1500 ms, TE = 53 ms, FOV = 40 × 16 × 16 mm^3, matrix = 320 × 128 × 128, RARE Factor = 16, TA ≅ 25 min. ^{19}F: TR = 1000 ms, TE = 6 ms, FOV = 40 × 16 × 16 mm^3, matrix = 100 × 40 × 40, zero fill acceleration = 2, RARE Factor = 40, number of averages (NEX) = 128, TA ≅ 45 min. For overview scans and serving as a reference to the ^{19}F MRS, it was used a 2D FLASH method. ^{19}F: TR = 15 ms, TE = 3.3 ms, one sagittal 3 mm slice, in-plane resolution (400 × 400) μm^2, NEX = 2048, TA = 15 min; ^{1}H: TR = 473 ms, TE = 13 ms, 22 slices, in plane resolution (73 × 73) μm^2, NEX = 16, TA = 25 min was used.

ii. T_2 mapping

To investigate possible changes in water content of CSF, T_2 mapping was performed since changes in T_2 relaxation time directly correlate to water content. For this purpose a multislice-multi-echo technique (MSME: TR = 1500 ms, matrix = 256 × 256, FOV = 1.8 cm, NEX = 2, slice = 1, TA = 15 min) was used. For this purpose TE ranging from (10–80) ms were used to vary T_2-weighting in increments of 10 ms. The slice was positioned horizontally using as reference the horizontal TurboRARE geometry covering cortex, caudate putamen, hippocampus, cerebellum and lateral, third and fourth ventricles.

iii. Single voxel MR spectroscopy

For the *in vivo* quantification of fluorine in a specific region a single voxel spectroscopy (SVS) was performed. For this purpose a (3 × 3 × 3) mm^3 voxel was placed within the region of interest inside the mouse cerebellum. After employing the FastMap37 method from Paravision software, for volume specific magnetic field (B_0) shimming, the spectra where acquired using a SVS protocol for ^{19}F MRS (Point-RESolved Spectroscopy, PRESS: TR = 1500 ms, TE = 11.6 ms, NEX = 512, TA = 13 min). To quantify the ^{19}F signal *in vivo*, a ^{19}F MRS calibration curve was created using the same PRESS protocol with three 15 ml Falcon tubes containing different known concentrations of our PFCE Emulsion (10, 20 and 40 mM).

c. ^{19}F enriched nanoparticles preparation and characterization

Nanoparticles with high fluorine (^{19}F) content and DiI fluorescence were prepared for labeling inflammatory cells *in vivo*. These particles consisted of 600 mM perfluoro-15-crown-5-ether (PFCE, Fluorochem, Derbyshire, UK) and 630 µM 1,1'-Dioctadecyl-3,3,3',3'-Tetramethyl, indocarbocyanine Perchlorate (DiI, Molecular Probes®, Invitrogen, Darmstadt, Germany) and were prepared by first emulsifying PFCE in Pluronic F-68 (Sigma-Aldrich, Germany) via direct sonication, using a cell disrupting titanium sonotrode (Bandelin Sonopuls GM70, Bandelin, Berlin, Germany). After 1:1 (v/v) dilution with DPBS, the PFCE emulsion was further sonicated in the presence of 630 µM DiI to obtain a PFCE-DiI nanoparticle emulsion. In order to remove free DiI, the PFCE-DiI nanoparticle emulsion was then clarified on Sephadex G-50 (Sigma-Aldrich, Germany) columns. The nanoparticles physical characteristics such as z-average diameter, polydispersity index and zeta potential (ζ) were determined by dynamic light scattering using a Malvern Zetasizer Nano ZS instrument (Malvern Instruments, Worcestershire, UK). The particle size remained constant after incorporation of the DiI.

2.2. Animal experiments

All animal experiments were carried out in accordance with the guidelines provided and approved by the Animal Welfare Department of the LAGeSo State Office of Health and Social Affairs Berlin (Permit G-0172/10: MR Bildgebung d. Therapieansätze - EAE).

Experimental autoimmune encephalomyelitis (EAE) was induced in female SJL/J mice (Janvier SAS, Le Genest-St-Isle, France) as previously described [3]. Mice (12 weeks old) were immunized subcutaneously with 250 µg $PLP_{139-151}$ peptide (Pepceuticals Ltd., UK) and 800 µg mycobacterium

tuberculosis H37Ra (Difco) in 200 µl emulsion containing equal volumes of phosphate/buffered saline (PBS) and complete Freunds adjuvant (BD-Difco). Pertussis toxin (200 ng, List Biological Laboratories, US) was administered intraperitoneal on days 0 and 2. Mice were weighed and scored daily as follows: 0, no disease; 1, tail weakness and righting reflex weakness; 2, paraparesis; 3, paraplegia; 4, paraplegia with forelimb weakness or paralysis; 5, moribund or dead animal. Mice with a score of 2.5 or more received an intraperitoneal injection of 200 µl glucose (5%) daily and mice with a score of 3 for more than 24 hours were sacrificed. Animals used as controls were healthy untreated mice. For sham immunizations: the same protocol used for EAE was used except that the $PLP_{139-151}$ peptide was omitted from the immunization cocktail.

During MR experiments mice were positioned on a water circulated heated animal bed to ensure constant body temperature of 37 °C and were kept under constant anesthesia via a controlled continuous flow of air, oxygen and isoflurane 0.5–1.5% (Abbott GmbH & Co. KG, Wiesbaden, Germany. Body temperature and breathing rate were constantly checked by a remote monitoring system (Model 1025, SA instruments Inc., New York, USA).

3. Results

3.1. First study: Pilot study identifying cellular infiltration in the cerebellar cortex in early stage of EAE (PLoS One. 2012; 7(3):e32796)

Micro MRI of EAE animals (n = 9) was performed at baseline (prior to EAE induction) and on a daily basis starting from day 5 post immunization. All mice developed EAE. The average EAE score for all 9 mice was 1.7 ± 0.7 (± S.D.) and the average day of onset was 11.2 ± 1.6 days (± S.D.) with a range of 9–14 days post immunization.

The high spatial resolution achieved using a cryogenically cooled RF coil allowed us to identify lesions prior to the onset of disease symptoms. The T_2W TurboRARE method provided the best image contrast and enabled observation of lesions in multiple brain regions, particularly the *arbor vitae* of the cerebellum (white matter) but also in the cerebral cortex and subcortical regions. Lesions could be detected as early as 3 days prior to clinical manifestation. Seven out of 9 EAE mice exhibited lesions in the brain. In the cerebellum the lesions appeared first as hyper-intense regions in the white matter of the arbor vitae. Remarkably prior the manifestation of the disease hypo-intense islands indicative of cellular involvement became evident inside the hyper-intense lesions.

Also prior to manifestation of clinical symptoms, lesions could be detected in the cortex. Compared to the T_1W scans, T_2W imaging was valuable to detect punctuate lesions in multiple regions of the inflamed brain (Figure 1). T_2*W imaging revealed these signal changes in even greater detail, commonly in association with intracortical vessels. Moreover the susceptibility weighted imaging (SWI) processed from the T_2*W phase maps, further enhanced the contrast between normal tissue, inflammatory lesion and microvasculature enabling the visualization of small venous irregularities (Figure 1). The proximity of the structural irregularities to the vasculature in the cerebellum and cerebral cortex (detected using T_2W and T_2*W imaging) was suggestive of inflammatory cell pathology. These hypo-intense areas could indeed be corroborated with the presence of inflammatory cell foci in hematoxylin and eosin histology of the same region imaged *in vivo*. This strong correlation between the MRI data and the histology corroborates the µMRI data and underscores the utility of µMRI to reveal histologically relevant pathology sites *in vivo.*

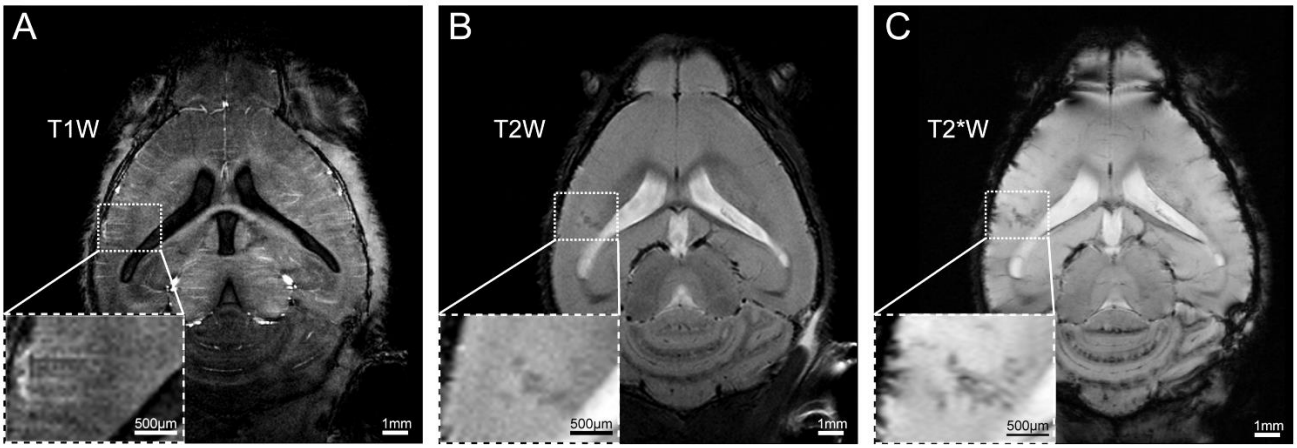

Figure 1 High resolution MRI reveals focal hypo-intense inflammation in the cerebral cortex of EAE mice. (A) T_1W horizontal scan using MDEFT (16 slices, FOV 18×18 mm, Matrix 384×384, 400 µm slice-thickness). **(B)** T_2W imaging using TurboRARE with geometry and resolution kept the same as for T_1W MDEFT. (C) T_2*W imaging using a FLASH multislice method with same slice thickness as in A and B.

To reveal diffuse contrast enhanced lesions in correspondence with T_2W lesions, T_1W imaging was preformed pre and post contrast (Gd-DTPA). Lesions in close proximity to the ventricular system (as detected by T_2W and T_2*W microstructural MRI), resulted in leakage of contrast agent (CA) in the ventricles following administration of Gd-DTPA. As a result the CA-enriched ventricular system could be visualized three-dimensionally together with the brain vasculature by using the GEFC-3D FLASH. The visualization of the ventricular system in association with the vasculature was only evident in EAE mice with periventricular lesions post CA and was not detectable in healthy control mice following CA application. While the precise mechanism still needs to be clarified, these results suggest that an inflammation-induced disruption of the BCSFB barrier might lead to extravasation of CA into the ventricular compartment such that the CSF flow could be captured by the GEFC-3D FLASH scan.

3.2. Second Study: Ventriculomegaly as early indicator of Encephalomyelitis (PLoS One. 2013 Aug 22; 8(8):e72841)

In this study brain modifications were investigated in EAE mice (n = 20) and control sham immunized mice (n=6). All mice immunized with specific CNS peptide eventually developed symptomatic EAE. The average day of disease clinical manifestation was 10.8 ± 1.1 (± S.D.) days post immunization, comparable to our previous study. Animals started losing weight 3-4 days before

disease onset and began reverting to normal 3-4 days after symptoms manifestation. Peak of disease (average score = 1.9 ± 0.7 (± S.D.)) was commonly reached after 3 days following the first clinical manifestation.

As shown in the previous study the most common lesions detected in T_2W µMRI are hyper- and hypo- intense regions in the white matter of the cerebellum. The temporal changes of these lesions were investigated over time. Out of 20 animals that developed EAE, 18 showed pre-symptomatic cerebellar lesions on average 2w.5 (±1.09 S.D.) days before the first manifestation of clinical signs. Lesion appearance could be observed up to 5 days before disease onset. Excluding two animals, that did not show any µMRI visible pathology within the cerebellum, EAE mice commonly displayed early cerebellar lesions at least one day before manifestation of clinical disease.

One surprising and consistent observation that was made during this longitudinal study was a distinct increase in cerebral ventricle size before the onset of disease symptoms. In 19 out of 20 immunized mice an increase in ventricular volume was observed and in 16 of these 19 animals, the ventricular expansion was detected prior to manifestation of clinical disease. This early volume change could be observed up to five days prior the first symptom. Changes in ventricle volume were synchronized to the first day of symptom manifestation, defined as time point 0. On average, EAE mice exhibited an increase in ventricle size 1.6 ± 1.2 (± S.D.) days before the first symptom. Figure 2A shows a representative mouse in which ventricle enlargement was detected two days (d -2) before start of symptoms. In this EAE mouse a decrease in ventricle size, three days (d +3) following the symptom onset, defined as the first day of evident motor impairment (tail weakness) was detected. Interestingly, one of the EAE mice that developed no evidence of microscopic changes (e.g. cerebellar lesions) in MRI — although clinical symptoms were observed — also exhibited no ventricle volume increase.

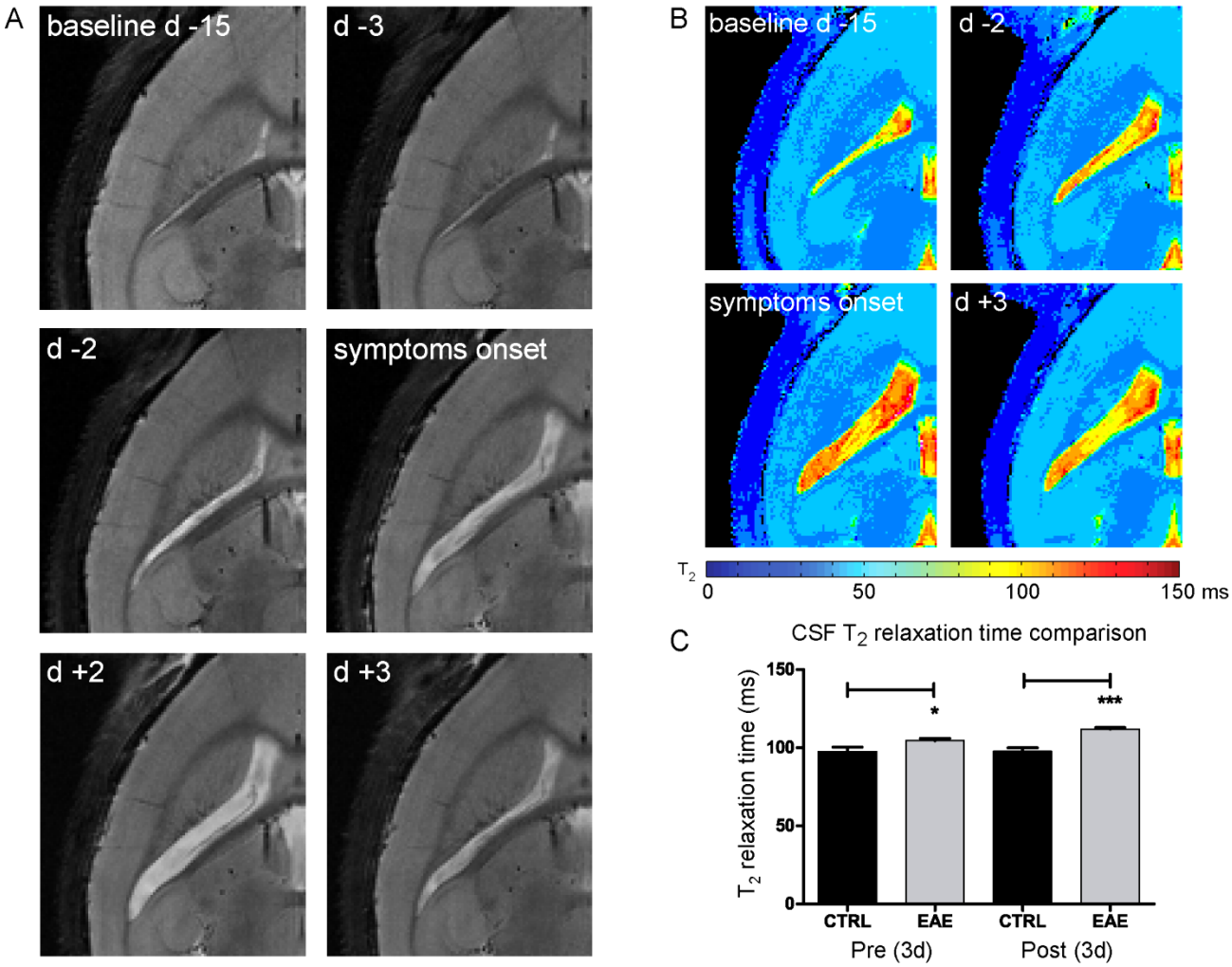

Figure 2. Pre-symptomatic ventricle volume changes in an EAE mouse model. (A) T_2-weighted horizontal views of the mouse brain show the evolution of changes in ventricle size of a representative mouse from baseline (pre EAE induction) 15 days prior (d-15) to disease manifestation up till 3 days after disease manifestation (d +3). **(B)** Representative maps of another mouse, depicting the absolute T_2 relaxation time (ms) prior to and after disease manifestation. **(C)** Differences in T_2 relaxation times between the control (CTRL) and EAE groups prior to (Pre (3d), $p = 0.0386$) and after (Post (3d), $p = 0.0002$) disease manifestation.

Ventricle volume was normalized to the baseline values (before EAE immunization). The average mean size of the ventricle at baseline was 10.7 ± 1.1 (± S.D.) mm^3. In EAE mice the ventricle size started to expand on average already 2 days before disease onset and in some cases growing 2 times more than baseline volume. Of note the ventricles in 3 EAE mice started to revert to normal volume values during disease remission. The size reduction started at the peak of symptoms on average 3 days after disease manifestation (peak of the disease) hence anticipating remission.

One possible explanation for the ventricular enlargement could be an impediment in cerebral CSF flow due to a physical obstruction at the interventricular foramen. Changes in volume in all four ventricles were thus measured separately to determine whether the ventricles downstream of the lateral ventricles also changed in size. The analysis of each separate ventricle revealed that each ventricular compartment significantly increased in size prior to clinical symptom onset, although the expansions of the third and fourth ventricle were less pronounced. These findings precluded physical obstruction at the foramina and suggested that the increase in volume could be the result of a dysregulation in CSF homeostasis.

The ventriculomegaly observed at such an early stage of disease was suggestive of an increase in water content within the ventricles. To investigate this, T_2 relaxometry was performed to measure water content within the ventricles during the volume changes. Data acquired on three consecutive days prior first symptoms were pooled and compared to the pooled data from the three days after first symptoms, age-matched control animals were also included for comparison. When compared to the CSF T_2 relaxation time of healthy animals, an increase in T_2 relaxation time was observed both prior to (controls = 106.4 ± 5.83 (± S.D.), EAE mice = 110.8 ± 4.18 (± S.D.), p = 0.0586) and following (controls = 107.3 ± 3.10 (± S.D.), EAE mice = 116 ± 4.29 (± S.D.), p = 0.0004) disease onset (Figure 2B, 2C).

3.3. Third study: Application of ^{19}F MRI to study brain inflammation in EAE (Sci Rep. 2013; 3:1280)

From the observations made in the first EAE studies using MR cryogenically-cooled coil technology there were indications of immune cell involvement during the early stages of EAE disease. In the first study, hypo-intense signals in close association with the ventricles were associated with a leakage into the ventricles and the early-stage ventriculomegaly in the second study was associated with increased water content (T_2 mapping). In the third study ^{19}F/^{1}H MR technologies were implemented to study the migration of inflammatory cells during EAE. Initially a single dose of nanoparticles containing 40 µmol PFCE was administered intravenously to EAE mice upon initiation of disease, 18 h prior to ^{19}F/^{1}H MRI. Combined ^{19}F/^{1}H MR measurements were made using an in-house built dual-tunable radiofrequency probe that allowed consecutive acquisition of both ^{19}F and ^{1}H images. In order to determine whether ^{19}F labeled inflammatory cells localize to the cerebellum, which is the region of the brain most commonly affected during EAE, a (3 × 3 × 3) mm³

voxel was localized around the cerebellum and PRESS performed in order to quantify the amount of ^{19}F within the inflammatory cells localizing within the specified region. Using 2D-FLASH, a slice thickness of 3 mm, the dimension used for the PRESS voxel, was used in order to increase the ^{19}F signal. The overlay of the T_2W ^{1}H sagittal image with the ^{19}F image from the same sagittal section revealed that the ^{19}F signal was localized within the brain stem and the white matter of the cerebellum. The imaging session was followed by the extraction of the cerebellum that underwent electron microscopy examination. Electron microscopy revealed that macrophage-like cells that were infiltrating the cerebellar lesion engulfed small round white fluorine particles within phagosomes.

To be able to achieve a high enough ^{19}F signal in the brain, the protocol for ^{19}F nanoparticle intravenous application was altered; the PFCE dose was reduced to 5 µmol and administered daily for 5 days, starting from day 5 following immunization. The scanning method was also altered. First an *in vivo* ^{1}H 3D TurboRARE was acquired to achieve a 125 μm^3 isotropic resolution. The ^{19}F MR TurboRARE with a reconstructed 400 μm^3 isotropic resolution was performed on the same mouse after it had undergone terminal anesthesia. The subsequent overlaying of the ^{19}F images with the ^{1}H scans revealed that the ^{19}F signal was mostly localized in areas of inflammatory cell involvement such as the spinal cord, the brain stem, the cerebellum and the cerebral cortex, also in close proximity to the ventricles. A strong ^{19}F signal was also observed in the cervical draining LNs, areas of expected high inflammatory cell activity.

To track the dynamics of inflammatory cells during EAE the ^{19}F method used in the *ex vivo* experiment was altered to reduce the acquisition time and adapt it to the *in vivo* study. In agreement with the ^{19}F signal observed post mortem, *in vivo* ^{19}F signals were localized within draining LNs, spinal cord, brain stem, cerebellum and cerebral cortex. Typically, between day 5 and day 8 post EAE induction, the draining LNs were the first to give a ^{19}F signal. Immune cell infiltration in the CNS was usually observed starting between day 8 and day 11 post immunization (Figure 3). By administering fluorescently-tagged fluorine nanoparticles, the distribution of distinct immune cell population in the inflammation areas detected by ^{19}F MRI could be studied ex vivo using fluorescence based methods. Following extraction of the brain after $^{19}F/^{1}H$ MRI, immunohistological staining for macrophages and lymphocytes was performed specifically in the cerebellum, a region where the ^{19}F signal was paramount. ^{19}F-DiI nanoparticle co-localized

primarily with macrophage-like cells (F4-80$^+$ and Mac-2$^+$ cells) although a co-localization of ^{19}F-DiI nanoparticles with CD4$^+$ T cells was also detected. These conclusions were in agreement with flow cytometry that in addition displayed a differential contribution to the 19F signal in LNs and CNS by myeloid cells (more pronounced in the CNS) and CD3$^+$ T cells (more pronounced in LNs).

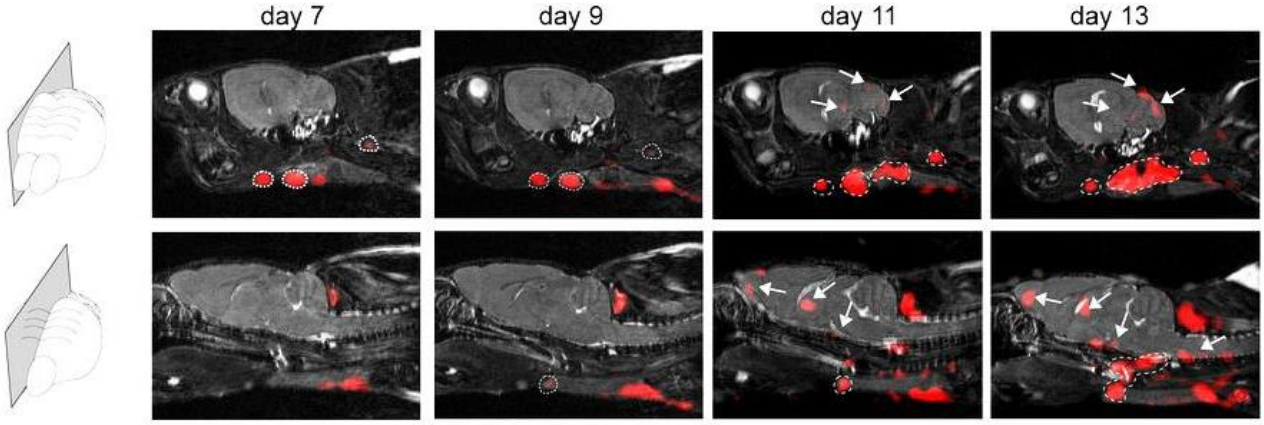

Figure 3. Visualization of inflammation in different CNS and lymphatic regions using *in vivo* ^{19}F/^{1}H MRI. Two different sagittal slices of a 3D Turbo RARE-scan show the kinetics of inflammatory cell migration (^{19}F MRI) over a period of 6 days in different CNS and lymphatic regions (^{1}H MRI).

4. Discussion

Experimental autoimmune encephalomyelitis is an animal model widely employed to examine the basic biology of CNS inflammatory processes, and to evaluate the effectiveness of nascent therapeutic approaches for multiple sclerosis [28]. In particular, EAE studies focusing on the early stages of brain inflammation have revealed new insights on the mechanisms involved in the different waves of immune cell entry during evolution of disease [11].

To gain a comprehensive and longitudinal view of brain inflammation – particularly during the early stages of EAE – methods employing high resolution brain imaging would be beneficial. However, longitudinal MRI studies (eg. to follow pathology during the course of EAE) are associated with long scanning procedure due to signal averaging to achieve enough signal and, as a result, less numbers of animals can be employed [29]. Therefore, methods that increase SNR are valuable to reduce scan time. Compared to room temperature coils, the gain in SNR achieved by cryogenically-cooled systems that reduce thermal noise [24] is a major advantage for studies with animal models, for two main reasons: (i) the acquisition of higher spatial resolution images within acceptable scan times is feasible and/or (ii) the imaging of larger numbers of animals with sufficient spatial resolution but within shorter times is possible. Depending on the design of the study it is possible to balance between both benefits.

Using this technology, in the first study, structural changes in EAE brains were observed prior to the onset of neurological symptoms; the cerebellum and cerebral cortex were affected. These detailed and highly resolved morphological changes were supported by subsequent histological examination, which showed clear evidence of infiltrated immune cells. With the cryogenically-cooled system it was feasible to apply imaging protocols for high spatial resolution (as small as $35 \times 35 \times 400$) μm^3, excellent grey matter–white matter contrast and high SNR with scan times not exceeding 15 min. The total scanning protocol length was suitable for longitudinal and *in vivo* studies, with acceptable sample sizes.

As a result of the improved spatial resolution gained, inflammatory cells were detected within the brain parenchyma. In combination with the CA Gd-DTPA, µMRI is valuable to differentiate lesions where the BBB is still intact (when CA enhancement is absent) and lesions with clear indication of BBB disruption (when CA leaks into the brain parenchyma).

In the second study the reduced scan time achieved by means of the cryogenically-cooled coil was capitalized to methodically follow the evolution of brain changes through the development of the EAE; both at a macroscopic and microscopic level, and using a large cohort of animals. Admittedly, the macroscopic changes that were observed in the second study (ventriculomegaly) should be expected to be observed by other room temperature coil systems. However use of the cryogenically-cooled coil resulted in significantly reduced scan times and permitted daily observations of the EAE brain.

Prior to the macroscopic changes in the ventricles, microscopic alterations in the brain parenchyma were detected. Microscopic changes involved evolving hyper- and hypo-intense regions in T_2-weighted images, particularly in the cerebellar white matter and as early as three days before symptom onset. The latter is in line with the first µMRI study in EAE mice where the presence of hypo-intense lesions in T_2-weighted images was confirmed as areas of immune cell infiltration using histology.

The microscopic cerebellar changes were shortly followed — at a macroscopic level — by an increase in ventricular size that was also accompanied by an increase in water content as indicated by increased T_2 relaxation times in the CSF. Since all ventricular compartments increased in size prior to disease onset, the possibility that the ventricular enlargement was the result of a physical obstruction was rejected. Alternatively, a disruption of the tight junctions (TJ) of the BBB and blood CSF barrier may increase the flux of solutes through the barrier leading to fluid leakage into the CSF-filled compartments. It has been demonstrated that during EAE and MS, an alteration of BBB tight junctions (TJ) occurs in association with the presence of inflammatory cells [30]. Besides, it was already suggested during the first study that a CA-enriched ventricular system is indicative of further leakage via the blood CSF barrier during EAE disease.

Several CSF drainage routes exist that might be involved in the communication between CNS and the lymphatic system. Important communication routes include anatomical sites (such as the cribriform plate) associated with nasal and cervical lymphatics [31]; immune cells, including memory $CD4^+$ T cells, follow these communication routes during autoimmune neuroinflammation [3232]. In agreement with this study, an extensive accumulation of inflammatory cells was shown on the ventral side of the forebrain, midbrain and brainstem using $^{19}F/^{1}H$ MRI in the third study.

By using fluorescently-labeled ^{19}F-rich particles, inflammatory cells could be discerned with ^{19}F/^{1}H MRI and the cell types subsequently identified with the help of fluorescent methods. From these results, it was possible to conclude that CD11c^{+} and CD11b^{+} myeloid cells are sequestered from the draining LN during early stages of the disease to enter the CNS, predominantly into cerebellum, brain stem and also cerebral cortex. Also CD4^{+} T cells labeled fluorescently-labeled ^{19}F-rich particles could be identified by immunohistological stains. The initial ^{19}F signals detected *in vivo* were mostly located within draining LN; typically the submandibular LN, superficial and deeper cervical LN, facial LN and internal jugular LN. These results further support the significance of the lymphatic system for initiation of CNS inflammation.

In summary, evolving MR technologies have been exploited in this work in order to further understand the kinetics and dynamics of inflammation during EAE. The use of a cryogenically-cooled coil allowed an increased image spatial resolution permitting the visualization of cellular infiltrates *in vivo*, as confirmed by the histology, also in the early stages of EAE disease progression. Taking advantage of the reduced acquisition time needed by the cryogenic system to scan the animal brain the collection of data from a large cohort of animals during the development of EAE was possible. The results in the EAE model provide first indications that the progression of encephalomyelitis goes together with substantial ventricle volume variation already in the earliest stages of disease before clinical signs manifestation and is accompanied with an increase of CSF T_2 relaxation time. By using ^{19}F-enriched nanoparticles and ^{19}F/^{1}H MR methods the dynamics of inflammatory cell migration could be visualized and followed during EAE. Throughout the disease progression, ^{19}F signal changes were observed in the draining LNs (starting at day 5 post immunization) and brain (particularly cerebellum, brain stem and cerebellar cortex) at later time points (day 8 post immunization). Moreover injected fluorescently labeled ^{19}F nanoparticles are taken up predominantly by macrophage-like cells but also CD4^{+} T cells as demonstrated by the immunohistological staining of the cerebellum. Further preclinical investigations are warranted to elucidate the basis leading to ventricular enlargement and ^{19}F/^{1}H MRI in autoimmune encephalomyelitis and other neurodegenerative disorders. Tagging of autoreactive T_H cells with ^{19}F, will be a particularly appealing method to further uncover the link between the CNS environment and the immune system.

5. Bibliography

1. Kingwell E, Marriott JJ, Jette N, Pringsheim T, Makhani N, Morrow SA, Fisk JD, Evans C, Beland SG, Kulaga S, Dykeman J, Wolfson C, Koch MW, and Marrie RA, *Incidence and prevalence of multiple sclerosis in Europe: a systematic review.* BMC Neurol, 2013. **13**: p. 128.

2. Constantinescu CS, Farooqi N, O'Brien K, and Gran B, *Experimental autoimmune encephalomyelitis (EAE) as a model for multiple sclerosis (MS).* Br J Pharmacol, 2011. **164**(4): p. 1079-106.

3. Aktas O, Waiczies S, Smorodchenko A, Dorr J, Seeger B, Prozorovski T, Sallach S, Endres M, Brocke S, Nitsch R, and Zipp F, *Treatment of relapsing paralysis in experimental encephalomyelitis by targeting Th1 cells through atorvastatin.* J Exp Med, 2003. **197**(6): p. 725-33.

4. Jager A, Dardalhon V, Sobel RA, Bettelli E, and Kuchroo VK, *Th1, Th17, and Th9 effector cells induce experimental autoimmune encephalomyelitis with different pathological phenotypes.* J Immunol, 2009. **183**(11): p. 7169-77.

5. Ousman SS and Kubes P, *Immune surveillance in the central nervous system.* Nat Neurosci, 2012. **15**(8): p. 1096-101.

6. Sinnecker T, Mittelstaedt P, Dorr J, Pfueller CF, Harms L, Niendorf T, Paul F, and Wuerfel J, *Multiple sclerosis lesions and irreversible brain tissue damage: a comparative ultrahigh-field strength magnetic resonance imaging study.* Arch Neurol, 2012. **69**(6): p. 739-45.

7. Gold R, Linington C, and Lassmann H, *Understanding pathogenesis and therapy of multiple sclerosis via animal models: 70 years of merits and culprits in experimental autoimmune encephalomyelitis research.* Brain, 2006. **129**(Pt 8): p. 1953-71.

8. Pepper M and Jenkins MK, *Origins of CD4(+) effector and central memory T cells.* Nat Immunol, 2011. **12**(6): p. 467-71.

9. Kivisakk P, Imitola J, Rasmussen S, Elyaman W, Zhu B, Ransohoff RM, and Khoury SJ, *Localizing central nervous system immune surveillance: meningeal antigen-presenting cells activate T cells during experimental autoimmune encephalomyelitis.* Ann Neurol, 2009. **65**(4): p. 457-69.

10. Kivisakk P, Mahad DJ, Callahan MK, Trebst C, Tucky B, Wei T, Wu L, Baekkevold ES, Lassmann H, Staugaitis SM, Campbell JJ, and Ransohoff RM, *Human cerebrospinal fluid central memory CD4+ T cells: evidence for trafficking through choroid plexus and meninges via P-selectin.* Proc Natl Acad Sci U S A, 2003. **100**(14): p. 8389-94.

11. Ransohoff RM, *Immunology: In the beginning.* Nature, 2009. **462**(7269): p. 41-2.

12. Robinson AP, Harp CT, Noronha A, and Miller SD, *The experimental autoimmune encephalomyelitis (EAE) model of MS: utility for understanding disease pathophysiology and treatment.* Handb Clin Neurol, 2014. **122**: p. 173-89.

13. Yednock TA, Cannon C, Fritz LC, Sanchez-Madrid F, Steinman L, and Karin N, *Prevention of experimental autoimmune encephalomyelitis by antibodies against alpha 4 beta 1 integrin.* Nature, 1992. **356**(6364): p. 63-6.

14. Derfuss T, Kuhle J, Lindberg R, and Kappos L, *Natalizumab therapy for multiple sclerosis.* Semin Neurol, 2013. **33**(1): p. 26-36.

15. Polman CH, Reingold SC, Banwell B, Clanet M, Cohen JA, Filippi M, Fujihara K, Havrdova E, Hutchinson M, Kappos L, Lublin FD, Montalban X, O'Connor P, Sandberg-Wollheim M, Thompson AJ, Waubant E, Weinshenker B, and Wolinsky JS, *Diagnostic criteria for multiple sclerosis: 2010 revisions to the McDonald criteria.* Ann Neurol, 2011. **69**(2): p. 292-302.

16. Stangel M, Fredrikson S, Meinl E, Petzold A, Stuve O, and Tumani H, *The utility of cerebrospinal fluid analysis in patients with multiple sclerosis.* Nat Rev Neurol, 2013. **9**(5): p. 267-76.

17. Kraft GH, *Evoked potentials in multiple sclerosis.* Phys Med Rehabil Clin N Am, 2013. **24**(4): p. 717-20.

18. Radue EW, O'Connor P, Polman CH, Hohlfeld R, Calabresi P, Selmaj K, Mueller-Lenke N, Agoropoulou C, Holdbrook F, de Vera A, Zhang-Auberson L, Francis G, Burtin P, and Kappos L, *Impact of fingolimod therapy on magnetic resonance imaging outcomes in patients with multiple sclerosis.* Arch Neurol, 2012. **69**(10): p. 1259-69.

19. Erbayat Altay E, Fisher E, Jones SE, Hara-Cleaver C, Lee JC, and Rudick RA, *Reliability of classifying multiple sclerosis disease activity using magnetic resonance imaging in a multiple sclerosis clinic.* JAMA Neurol, 2013. **70**(3): p. 338-44.

20. Van Lambalgen R and Jonker M, *Experimental allergic encephalomyelitis in rhesus monkeys: II. Treatment of EAE with anti-T lymphocyte subset monoclonal antibodies.* Clin Exp Immunol, 1987. **68**(2): p. 305-12.

21. Serres S, Bristow C, de Pablos RM, Merkler D, Soto MS, Sibson NR, and Anthony DC, *Magnetic resonance imaging reveals therapeutic effects of interferon-beta on cytokine-induced reactivation of rat model of multiple sclerosis.* J Cereb Blood Flow Metab, 2013. **33**(5): p. 744-53.

22. Serres S, Anthony DC, Jiang Y, Campbell SJ, Broom KA, Khrapitchev A, and Sibson NR, *Comparison of MRI signatures in pattern I and II multiple sclerosis models.* NMR Biomed, 2009. **22**(10): p. 1014-24.

23. Wuerfel J, Tysiak E, Prozorovski T, Smyth M, Mueller S, Schnorr J, Taupitz M, and Zipp F, *Mouse model mimics multiple sclerosis in the clinico-radiological paradox.* Eur J Neurosci, 2007. **26**(1): p. 190-8.

24. Baltes C, Radzwill N, Bosshard S, Marek D, and Rudin M, *Micro MRI of the mouse brain using a novel 400 MHz cryogenic quadrature RF probe.* NMR Biomed, 2009. **22**(8): p. 834-42.

25. Mattrey RF, Long DM, Multer F, Mitten R, and Higgins CB, *Perfluoroctylbromide: a reticuloendothelial-specific and tumor-imaging agent for computed tomography.* Radiology, 1982. **145**(3): p. 755-8.

26. Flogel U, Ding Z, Hardung H, Jander S, Reichmann G, Jacoby C, Schubert R, and Schrader J, *In vivo monitoring of inflammation after cardiac and cerebral ischemia by fluorine magnetic resonance imaging.* Circulation, 2008. **118**(2): p. 140-8.

27. Ahrens ET and Zhong J, *In vivo MRI cell tracking using perfluorocarbon probes and fluorine-19 detection.* NMR Biomed, 2013. **26**(7): p. 860-71.

28. Steinman L and Zamvil SS, *How to successfully apply animal studies in experimental allergic encephalomyelitis to research on multiple sclerosis.* Ann Neurol, 2006. **60**(1): p. 12-21.

29. Tysiak E, Asbach P, Aktas O, Waiczies H, Smyth M, Schnorr J, Taupitz M, and Wuerfel J, *Beyond blood brain barrier breakdown - in vivo detection of occult neuroinflammatory foci by magnetic nanoparticles in high field MRI.* J Neuroinflammation, 2009. **6**: p. 20.

30. Morgan L, Shah B, Rivers LE, Barden L, Groom AJ, Chung R, Higazi D, Desmond H, Smith T, and Staddon JM, *Inflammation and dephosphorylation of the tight junction protein occludin in an experimental model of multiple sclerosis.* Neuroscience, 2007. **147**(3): p. 664-73.

31. Walter BA, Valera VA, Takahashi S, Matsuno K, and Ushiki T, *Evidence of antibody production in the rat cervical lymph nodes after antigen administration into the cerebrospinal fluid.* Arch Histol Cytol, 2006. **69**(1): p. 37-47.

32. Giunti D, Borsellino G, Benelli R, Marchese M, Capello E, Valle MT, Pedemonte E, Noonan D, Albini A, Bernardi G, Mancardi GL, Battistini L, and Uccelli A, *Phenotypic and functional analysis of T cells homing into the CSF of subjects with inflammatory diseases of the CNS.* J Leukoc Biol, 2003. **73**(5): p. 584-90.

Affidavit

I, Stefano Lepore certify under penalty of perjury by my own signature that I have submitted the thesis on the topic: “Studies on a Preclinical Model of Brain Autoimmunity using Emerging Magnetic Resonance Methods”. I wrote this thesis independently and without assistance from third parties, I used no other aids than the listed sources and resources.

All points based literally or in spirit on publications or presentations of other authors are, as such, in proper citations (see "uniform requirements for manuscripts (URM)" the ICMJE www.icmje.org) indicated. The sections on methodology (in particular practical work, laboratory requirements, statistical processing) and results (in particular images, graphics and tables) correspond to the URM (s.o) and are answered by me. My contributions in the selected publications for this dissertation correspond to those that are specified in the following joint declaration with the responsible person and supervisor. All publications resulting from this thesis and which I am author of correspond to the URM (see above) and I am solely responsible.

The importance of this affidavit and the criminal consequences of a false affidavit (section 156,161 of the Criminal Code) are known to me and I understand the rights and responsibilities stated therein.

_____

Date Signature

Declaration of contribution to the selected publications

Stefano Lepore had the following share in the following publications:

Publication 1: *Identification of cellular infiltrates during early stages of brain inflammation with magnetic resonance microscopy*. Waiczies H, Millward JM, **Lepore S**, Infante-Duarte C, Pohlmann A, Niendorf T, Waiczies S, PLoS One, 2012. PLoS One. 2012;7(3):e32796.

Contribution in detail:

- Animal experiment (EAE, contrast agent iv. injection)
- Image acquisition
- Figure preparation
- Supporting manuscript preparation

Publication 2: *Enlargement of Cerebral Ventricles as an Early Indicator of Encephalomyelitis*. **Lepore S**, Waiczies H, Hentschel J, Ji Y, Skodowski J, Pohlmann A, Millward JM, Paul F, Wuerfel J, Niendorf T, Waiczies S., PLoS One, 2013. PLoS One. 2013 Aug 22;8(8):e72841.

Contribution in detail:

- Experimental design
- Animal experiment
- Image acquisition
- Data post-processing tool development
- Data analysis and statistical evaluation
- Manuscript and figure preparation

Publication 3: *Visualizing brain inflammation with a shingled-leg radio-frequency head probe for 19F/1H MRI*. Waiczies H, **Lepore S**, Drechsler S, Qadri F, Purfürst B, Sydow K, Dathe M, Kühne A, Lindel T, Hoffmann W, Pohlmann A, Niendorf T, Waiczies S., Scientific reports, 2013. Sci Rep. 2013;3:1280.

Contribution in detail:

- Animal experiment (EAE, ^{19}F injection, terminal surgery)
- ^{19}F nanoparticle preparation
- Image acquisition
- Supporting manuscript preparation

Signature, date and stamp of the supervising University teacher

_____

Prof. Dr. Thoralf Niendorf

Signature of the doctoral candidate

_____

Stefano Lepore

OPEN ACCESS Freely available online

PLoS one

Identification of Cellular Infiltrates during Early Stages of Brain Inflammation with Magnetic Resonance Microscopy

Helmar Waiczies[1,2☯], Jason M. Millward[1,3☯], Stefano Lepore[1,2], Carmen Infante-Duarte[1,3], Andreas Pohlmann[2], Thoralf Niendorf[1,2¶], Sonia Waiczies[1,2,4*¶]

1 Experimental and Clinical Research Center, a joint cooperation between the Charité Medical Faculty and the Max-Delbrück Center for Molecular Medicine, Berlin, Germany, **2** Berlin Ultrahigh Field Facility, Max-Delbrück Center for Molecular Medicine, Berlin, Germany, **3** Experimental Neuroimmunology, Charité Universitätsmedizin Berlin, Berlin, Germany, **4** Department of Anatomy, University of Malta, Msida, Malta

Abstract

A comprehensive view of brain inflammation during the pathogenesis of autoimmune encephalomyelitis can be achieved with the aid of high resolution non-invasive imaging techniques such as microscopic magnetic resonance imaging (μMRI). In this study we demonstrate the benefits of cryogenically-cooled RF coils to produce μMRI *in vivo*, with sufficient detail to reveal brain pathology in the experimental autoimmune encephalomyelitis (EAE) model. We could visualize inflammatory infiltrates in detail within various regions of the brain, already at an early phase of EAE. Importantly, this pathology could be seen clearly even without the use of contrast agents, and showed excellent correspondence with conventional histology. The cryogenically-cooled coil enabled the acquisition of high resolution images within short scan times: an important practical consideration in conducting animal experiments. The detail of the cellular infiltrates visualized by *in vivo* μMRI allows the opportunity to follow neuroinflammatory processes even during the early stages of disease progression. Thus μMRI will not only complement conventional histological examination but will also enable longitudinal studies on the kinetics and dynamics of immune cell infiltration.

Citation: Waiczies H, Millward JM, Lepore S, Infante-Duarte C, Pohlmann A, et al. (2012) Identification of Cellular Infiltrates during Early Stages of Brain Inflammation with Magnetic Resonance Microscopy. PLoS ONE 7(3): e32796. doi:10.1371/journal.pone.0032796

Editor: Pablo Villoslada, Institute Biomedical Research August Pi Sunyer (IDIBAPS) - Hospital Clinic of Barcelona, Spain

Received September 2, 2011; **Accepted** January 31, 2012; **Published** March 12, 2012

Funding: This study was funded by the Deutsche Forschungsgemeinschaft (DFG) to SW (DFG WA 2804) and a university grant to SW from the Experimental and Clinical Research Center, a cooperation of the Max Delbrück Center for Molecular Medicine and Charité Medical Faculty in Berlin. The position of JM is funded by DFG KFO 213. The funders had no role in study design, data collection and analysis, decision to publish, or preparation of the manuscript.

Competing Interests: The authors have declared that no competing interests exist.

* E-mail: sonia.waiczies@charite.de

☯ These authors contributed equally to this work.

¶ These authors also contributed equally to this work.

Introduction

Inflammatory diseases of the central nervous system (CNS) such as multiple sclerosis (MS) involve a recruitment of immune cells during the early stages of pathogenesis, prior to the onset of clinical symptoms [1 3]. Normally the blood-brain barrier (BBB) restricts migration of immune cells to the CNS, but during inflammation its function becomes altered. Immune cells gain access to CNS parenchyma via a complex, multi-step process that involves crossing both the vascular endothelium and the glia limitans [4,5]. The indirect detection of contrast-enhancing lesions (CEL) by Magnetic Resonance Imaging (MRI) at the site of BBB disruption as a result of contrast agent leakage into the CNS parenchyma is used as a primary end point in MS clinical trials [6,7] and in the EAE mouse model [8,9]. However, BBB disruption does not provide direct evidence of immune cell trafficking into the CNS [10], and may occur independently of the formation of new lesions [11]. There is therefore a need to pursue supplemental MRI techniques, to gain a more accurate and comprehensive view of the pathogenesis of CNS inflammation. One strategy has been to employ iron oxide nanoparticles [12], particularly as a means of studying immune cell infiltration in the animal model of CNS inflammation, experimental autoimmune encephalomyelitis (EAE) [13 16]. However the application of paramagnetic nanoparticles is hampered by a number of limitations, including the lack of an a priori knowledge of the specific time of immune cell migration into the brain parenchyma.

Microscopic MRI (μMRI or MR histology) defined as MRI with a spatial resolution <100 μm [17,18] is one means of amplifying image detail in order to observe even minor changes in brain pathology during the course of disease. MRI resolution depends on several factors including magnetic field strength, gradient strengths and digital resolution, but the main limiting factors are RF coil sensitivity and signal-to-noise ratio (SNR) [19]. Upon reducing voxel size to amplify spatial resolution, a loss in SNR is to be expected. This loss can be considerably compensated for by increasing signal averaging: this produces images with an impressive level of microscopic detail as shown in *ex vivo* fixed brain tissue samples [20]. However, increased signal averaging comes at a cost in scan time, and is hence not practical for studies with anesthetized animals. This along with the presence of movement artifacts makes it inherently difficult to achieve sufficient resolution to visualize brain pathology *in vivo*.

One approach to maximize effective spatial resolution is to increase signal sensitivity with cryogenically-cooled RF detection devices that boost SNR, the currency spent for image resolution and image quality [21]. Recently, RF coils made of superconducting material have been developed for animal micro-imaging, which reduce coil resistance and thermal noise and therefore increase SNR by up to a factor of up to 2.9 [22]. In essence such a system increases the field strength virtually by a factor of at least 2, according to MR principles, but without the disadvantages associated with higher field strengths, such as stronger susceptibility artifacts, B_0 inhomogeneities and shorter wavelengths. The effectiveness of this approach has been demonstrated in the healthy mouse brain [23].

Realizing the capabilities of μMRI, we focused here on high spatial resolution imaging of mice brain during the course of EAE in an attempt to visualize inflammatory pathology *in vivo* prior to and during commencement of disease. The ultimate aim of this study was to distinguish cellular infiltrates in microscopic detail at an early phase of disease. In this first study applying cryogenic MR technology to EAE, we demonstrate that brain pathology can be detected even without the use of contrast agents and show excellent correspondence between μMRI findings and conventional histology.

Results

Early detection of EAE pathology with high resolution cryogenic imaging

Using a cryogenically-cooled RF coil, we performed high spatial resolution brain imaging in EAE mice prior to and upon commencement of disease (**Figure S1**). The μMRI performed enabled us to detect lesions (as defined in Methods) already prior to clinical manifestation of disease. Using a T_2 weighted (T2W) TurboRARE sequence that results in better contrast between grey and white matter boundaries, we observed lesions in multiple regions of the EAE mouse brains, particularly the cerebellum, cerebral cortex and subcortical regions (thalamus and striatum). **Figure 1A** shows the anatomical distribution of the detected lesions as well as the time point of their first detection (relative to the starting point of disease). Out of 9 immunized mice, all of which developed EAE, 7 mice exhibited lesions in the brain (**Figure S2**). The average EAE score for all 9 mice was 1.7±0.7 (± S.D.) and the average day of onset was 11.2±1.6 days (± S.D.) with a range of 9 14 days post immunization. All mice were scanned 5 days post immunization; thus between 4 9 days prior to disease onset. Notably, lesions could be detected as early as 3 days (d-3) prior to the appearance of disease manifestations (**Figure 1A**). No lesions were observed earlier than 3 days prior to clinical manifestations. Lesions in the cerebellum were the most common, occurring between 1 to 3 days prior to onset of disease (**Figure 1A**, **Figure 1B** and **Figure S3**). The T2W images shown in **Figure 1B** and **Figure S3** represent the structural changes occurring in the cerebellum in a mouse during the 4 5 days prior to disease onset (d-5 d0) in comparison to baseline measurements (d-14) that were carried out prior to immunization. Hyperintense lesions in the white matter of the cerebellar *Arbor vitae* were already evident 2 days prior to neurological symptoms (d-2, upper and middle arrow head) and prominent on d-1 (along upper and lower arrowheads). Signal extinction that is indicative of cellular involvement became apparent on d-1 (dotted islands) but was more prominent upon onset of clinical symptoms (d0). To illustrate the potential for quantitative assessment of the lesions, we generated images in which we subtracted control baseline scans from scans showing brain pathology as changes in signal intensity (**Figure S4A**).

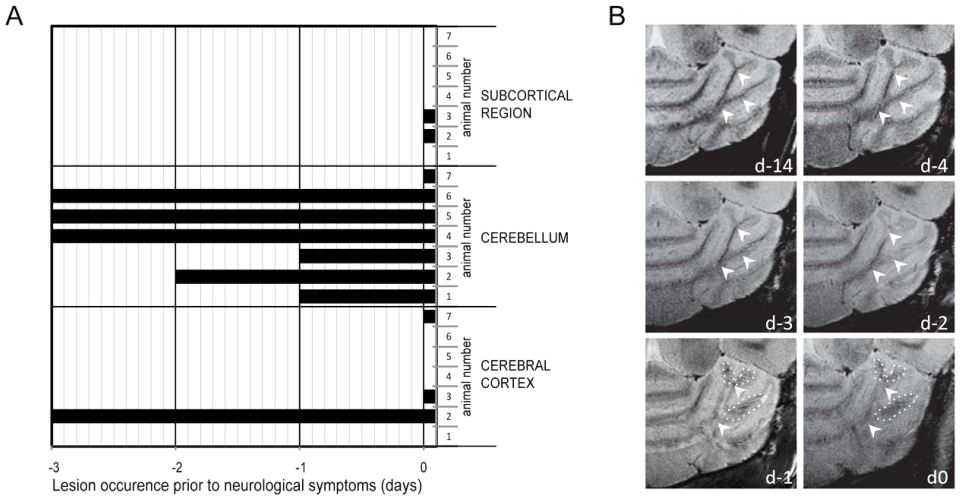

Figure 1. Anatomical distribution and evolution of lesions. EAE mice (n = 9) were immunized with $PLP_{139–151}$ peptide (EAE induction) and scored for neurological symptoms on a daily basis. Micro MRI was performed daily starting from d5 post immunization. (A) Shown are seven mice (1–7) exhibiting lesions within the brain – specifically cerebral cortex, cerebellum and subcortical areas (thalamus and striatum) – prior to or during onset of disease. The lower axis indicates the time-points prior to commencement of neurological symptoms (d0). (B) T2W images showing the evolution of cerebellar lesions (arrowhead) from baseline (pre EAE induction) 14 days prior to disease manifestation (d-14) until disease onset (d0). Arrowheads depict enhancement of signal intensity in the white matter over time and dotted islands depict signal extinctions in the vicinity.
doi:10.1371/journal.pone.0032796.g001

Hypointense lesions on T2W images represent cellular infiltrates

Early during disease progression, even prior to the onset of clinical manifestations, we also observed lesions in the cortex. **Figure 2** illustrates a representative mouse at onset of clinically observable signs of disease. Although major anatomical structures including the corpus callosum, striatum, ventricular system and hippocampus could be clearly resolved with T_1 weighted (T1W) scans (**Figure 2A**), no inflammatory pathology was observed with this method. T2W imaging, on the other hand, revealed focal hypo-intense lesions in multiple regions of the inflamed brains, mostly in the cerebellum (**Figure 1B**) but also in the somatosensory cortex (**Figure 2B**). T_2* weighted (T2*W) imaging revealed the signal extinctions observed by T2W imaging as punctate lesions, with greater detail and in association with intracortical vessels (**Figure 2C** and **Figure 3A**). We observed venous irregularities within the cortex in 3 out of the 7 mice that exhibited lesions in the brain. The irregularities were observed one day prior to symptoms or upon initiation of symptoms. Processing of T2*W phase maps for susceptibility weighted imaging (SWI) [24] has been employed in MS lesions to reveal superior detail in small anatomical structures such as the venous vasculature and structural variations within gray and white matter [25]. SWI of the phase maps derived from T2*W imaging yielded excellent visualization of the small venous irregularities and enhanced contrast between normal tissue, focal inflammatory lesions and the microvasculature as highlighted in **Figure 3B**. To make a more objective assessment of these structural changes we subtracted the images showing pathology from images obtained at baseline, prior to EAE immunization (**Figure S4B**). Notably, the structural irregularities observed in T2W or T2*W images corresponded with areas of inflammatory pathology – both in cerebrum (**Figure 3C**) and cerebellum (**Figure 3D**) – as revealed by conventional hematoxylin and eosin (H&E) histology. H&E stains corroborate the μMRI data and conform to the expected pattern of pathology in the EAE model. The EAE model has been extensively characterized, and it is well established that the lesions are comprised of immune cells, especially CD4+ T cells. Indeed, the lesions that we could visualize with μMRI show the same appearance and localization characteristics of CD4+ T cells (**Figure 3D**). The clear correlation between the MRI data and the histology underscores the utility of microscopic MRI to reveal histologically relevant pathology *in vivo* [24,25].

Contrast enhanced lesions in close proximity to ventricular system

Gadolinium contrast agents are frequently used in EAE studies, and Gd CEL have a typically diffuse appearance. T1W imaging post contrast (0.2 mmol/kg Gd-DTPA, Magnevist, Bayer-Schering Pharma AG, Berlin, Germany) revealed diffuse CEL (**Figure 4A** and **Figure 4B**) in all 7 mice exhibiting hyper- or hypo- intense lesions in the brain. These CEL, although more diffuse, corresponded in location to the T2W lesions shown by μMRI (**Figure 1, Figure 2, Figure 3**). This result corroborates the interpretation that the changes in signal intensities detected by T2W and T2*W microstructural MRI demonstrates the potential of microscopic MRI to reveal brain pathology with greater precision and detail than conventional contrast agents.

In EAE mice with lesions close to the ventricles, administration of Gd-DTPA enabled the visualization of the ventricular system (**Figure 4C**). The contrast-enriched ventricular system was visualized three-dimensionally together with the brain vasculature by performing a 29-minute 3D FLASH sequence with flow compensation (GEFC), typically employed for MR angiography, with an isotropic spatial resolution of 59 μm (**Figure 4C**). An overlay of the maximum intensity projections (MIP) of the 3D GEFC images with the MIP of post contrast T1W MDEFT CEL images shows the spatial relationship of the contrast-enhanced parenchyma (due to BBB disruption) with the ventricles and cerebral vasculature (**Figure 4D**). The visualization of the ventricular system together with the vasculature post contrast was only visible in EAE mice with periventricular lesions and was not visible in healthy non-immunized mice (**Figure S5**). While the precise mechanism still needs to be determined, these results suggest that an inflammation-induced disruption of the blood-cerebrospinal fluid barrier might lead to extravasation of contrast agent into the ventricular system.

Discussion

Experimental autoimmune encephalomyelitis is an animal model widely employed to examine the basic biology of CNS inflammatory processes, and to evaluate the effectiveness of nascent therapeutic approaches for multiple sclerosis [26–31]. In particular, EAE studies focusing on the early stages of brain inflammation have revealed new insights on the mechanisms

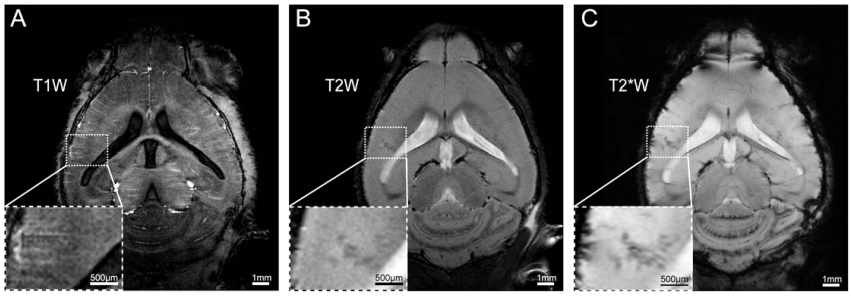

Figure 2. High resolution MRI reveals focal hypo-intense inflammation in the cerebral cortex of EAE mice. (A) T1W horizontal scan using an MDEFT sequence (TR/TE/TI 2600/3.9/950 ms, FOV 18×18 mm, Matrix 384×384, 2 averages) for 16 slices (400 μm slice-thickness). (B) T2W imaging using a TurboRARE sequence (TR/TE 3000/36 ms, FOV 18×18 mm, Matrix 384×384, RARE-factor 8) with same geometry and resolution as for T1W MDEFT. (C) T2*W imaging using a FLASH multislice sequence (TR/TE of 473/18 ms, FOV 18×18 mm, acquisition Matrix 512×256, reconstruction Matrix 512×512) with same slice thickness as in *A* and *B*.
doi:10.1371/journal.pone.0032796.g002

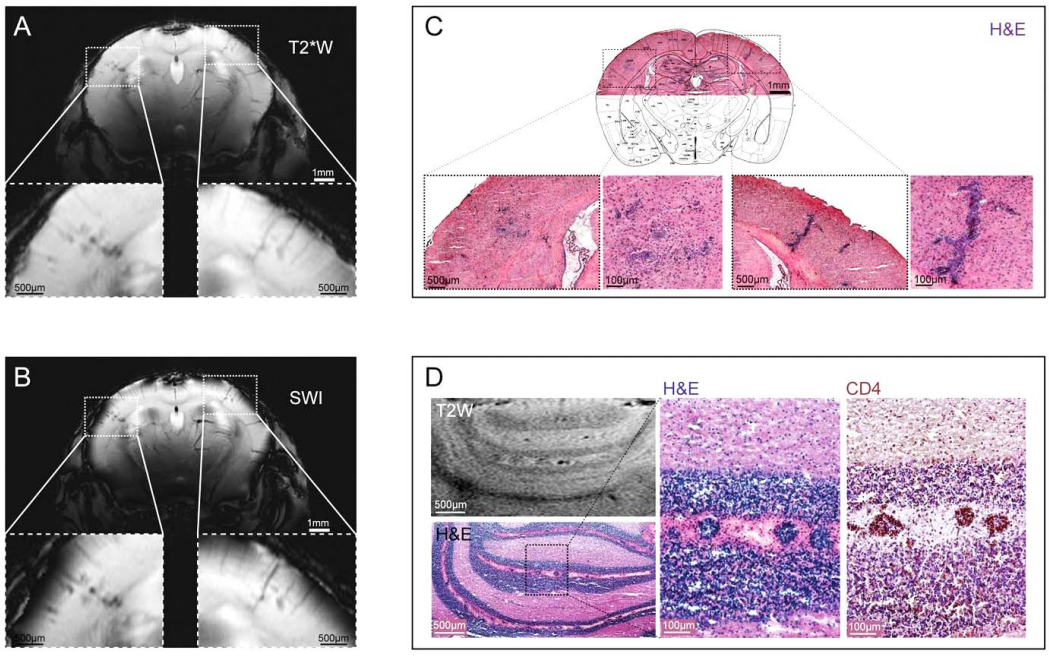

Figure 3. T2*W hypo-intense regions correspond to cellular infiltrates detected by histology. (A) Coronal T2*W imaging using the FLASH multislice sequence (22 slices with slice thickness of 500 μm). (B) Susceptibility weighted imaging (SWI) of T2*W scans using fully-automated post-processing by ParaVision 5.1 (Bruker, Ettlingen, Germany). (C) Cellular infiltrates in cerebral cortex; the overview of the H&E histology is overlaid with a coronal slice (plate 41) from Franklin K.B.J., Paxinos G: The Mouse Brain in Sterotaxic Coordinates. Academic Press; 2007 with kind permission from Elsevier. (D) Cellular infiltrates in cerebellar white matter lesions illustrated by CD4+ immunostaining and H&E staining.
doi:10.1371/journal.pone.0032796.g003

involved in the different waves of immune cell entry during evolution of disease [32].

To gain a comprehensive and longitudinal view of brain inflammation particularly during the early stages of EAE methods employing high resolution brain imaging would be advantageous. Several studies in EAE employing MRI have significantly contributed to our understanding of the pathology of brain inflammation [8,16,33,34]. However, in longitudinal MRI studies (eg. to follow pathology during the course of EAE) one main limiting factor is a restriction in the number of animals that can be employed due to the length of each scanning procedure. To overcome this, methods that increase SNR will be beneficial to enable shorter scans. The gain in SNR achieved by cryogenically-cooled systems that reduce thermal noise [22] is a major advantage for studies with animal models for two main reasons: (i) it enables the acquisition of images with greater spatial resolution within reasonable scan times; and (ii) it facilitates the imaging of larger numbers of animals with standard spatial resolution but within shorter times. Depending on the design of the study it is possible to compensate between both strengths.

The advantages and feasibility of cryogenically cooled coils particularly to image mouse brain anatomy has already been demonstrated at 4.7T [35] and 9.4T [22,23]. The scan time required using a conventional room-temperature coil to observe early pathological changes in the EAE brain (23 min for T2W imaging, 24 min for T2*W imaging) was at least three times longer than that of the currently employed cryogenically cooled coil (5 min for T2W imaging, 8 min for T2*W imaging) using the same magnetic field strength, considering the necessity to increase the number of excitations (NEX = 16 for RT coil compared with NEX = 1 for cryo coil) (**Figure S6**).

Handling of the currently available MRI cryogenic RF coils which evolved from NMR-spectroscopy [21] has significantly improved in recent years, and indeed is quite similar to any conventional RT RF-coil. One major drawback of the cryogenic probe used in this study is the transmission(TX)/reception(RX)-coil design, which leads to an inhomogeneous excitation field [22,35]. The non-uniform excitation field needs to be taken into account when applying quantification techniques such as relaxometry or spectroscopy, as well as magnetisation transfer ratio (MTR). Due to the variation of the flip-angle throughout the sample, the reference gain has to be carefully adjusted for the volume of interest to minimize these changes. In this case a RX-only design with a conventional actively de-tuned TX volume resonator for a homogeneous excitation would be beneficial [36].

The effective anatomical resolution we employed in this study is almost an order of magnitude higher than that attainable in human brain imaging using clinical MRI scanners. Using this technology we observed structural changes in EAE brains in regions including the cerebellum and cerebral cortex prior to the onset of neurological symptoms. These detailed and highly resolved morphological changes were corroborated by subsequent histological examination, which showed clear evidence of infiltrated immune cells. The general trend in lesion distribution

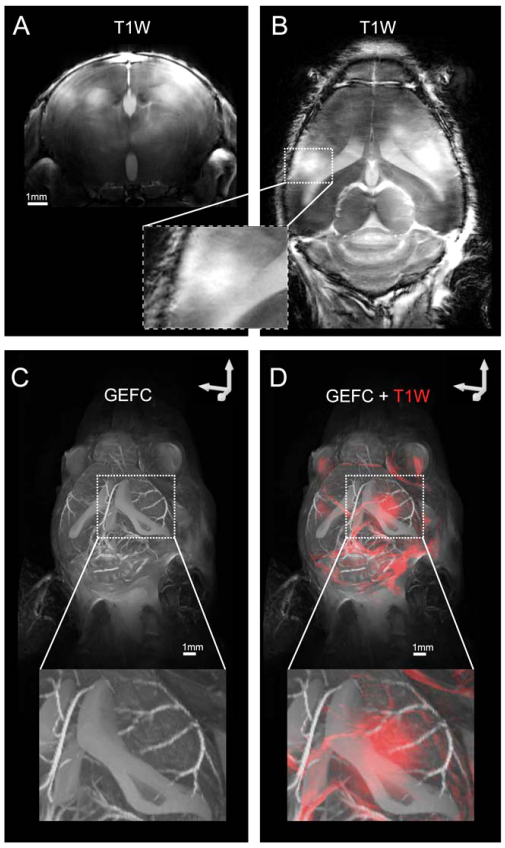

Figure 4. Three dimensional reconstruction of lesions in relation to the vascular and ventricular system. (A) Contrast-enhanced lesions (CEL) in coronal sections visualized by post Gd-DTPA contrast T1W MDEFT MRI (dotted line depicts horizontal slice in *B*). (B) CEL in horizontal sections imaged by post contrast T1W MDEFT (dotted line depicts coronal slice in *A*). (C) Maximum intensity projections (MIP) of images collected by 3D-GEFC showing the contrast-filled ventricular system and the cerebral vasculature (D) Overlay of a CEL 3D model (depicted in red) calculated from MIP of T1W MDEFT images on 3D ventricular and vascular system calculated from MIP of 3D-GEFC images.
doi:10.1371/journal.pone.0032796.g004

with the cerebellum being the predominant site of damage in the brain is in agreement with the ascending pattern of EAE. Disease progression in EAE shows a typical course of ascending paralysis, accompanied by inflammatory pathology that proceeds from the spinal cord initially affecting the tail and hind limbs, and subsequently precipitating complete paralysis. With this cryogenically-cooled system we were able to apply imaging protocols for high spatial resolution (as small as 35×35×400 μm), good grey matter white matter distinction and high SNR with scan times not exceeding 15 min. The entire scanning protocol presented herein requires at most 60 min pre contrast and 60 min post contrast, and is therefore suitable for both longitudinal and cross-sectional *in vivo* studies, with acceptable sample sizes.

Importantly, we were able to identify the presence of inflammatory cells within the brain parenchyma without the necessity of Gd-DTPA contrast agents. In contrast to the typical diffuse lesions revealed by Gd enhancement, the lesions detected by μMRI were more focused and more clearly demarcated. This represents a clear advantage of the cryogenic coil over the previous technology, as the ability to detect focal lesions by μMRI offers the potential for more precise quantification of inflammation severity, leading to more quantitatively robust EAE studies. However contrast agents are still powerful tools since they provide clear evidence of BBB disruption, although leakage of contrast agent in the parenchyma does not give definitive evidence of parenchymal damage. In situations where structural changes observed in the brain with μMRI are not accompanied by contrast enhancement, it is reasonable to speculate that immune cells may have penetrated the vascular endothelium thereby entering the pervascular spaces, but have not yet breached the glia limitans and infiltrated into the brain parenchyma. Such perivascular-restricted lesions are widely seen at the histological level in EAE but have not yet been detected by MRI. The possibility of μMRI with the cryogenic coil to detect such lesions, which are by definition not detectable by Gd leakage into the parenchyma, offers the potential for future investigations to observe pathological processes that would otherwise be invisible, and underscores the importance of this technology for MS research.

Another distinct advantage of the cryogenic RF coil for MS research is the possibility to include magnetic resonance angiography in the scanning protocol, in a quick and efficient manner, to monitor changes in the vasculature over the course of disease. Indeed, the present study represents the first application of MR angiography in the mouse EAE model. The observation of leakage of contrast agent into the ventricular system early in disease is interesting, in light of recent reports highlighting the importance of the choroid plexus [30] and the involvement of the circumventricular organs in EAE [37].

In summary, the visualization of cellular infiltrates by *in vivo* μMRI provides an opportunity to follow neuroinflammatory processes throughout disease progression. Thus in parallel to conventional histological examination and in combination with contrast agents, μMRI will be invaluable for longitudinal studies investigating immune cell infiltration during brain inflammation and evaluation of novel therapeutics. Future directions for μMRI studies in EAE will involve the application of techniques such as T2 mapping and MTR that provide valuable information on water/lipid content and myelin integrity during lesion development. These techniques have already been successfully employed in a model of oligodendrogliopathy [38,39] and will complement MR methods typically employed in EAE studies since they provide further knowledge regarding the neurodegenerative component of the disease.

Materials and Methods

Ethics Statement

Animal experiments were carried out in accordance with the guidelines provided and approved by the Animal Welfare Department of the *LAGeSo* State Office of Health and Social Affairs Berlin (Permit G0172/10).

Active EAE

To actively induce EAE, 6 8 week old female SJL/J mice (Janvier, France) were immunized subcutaneously with 250 μg $PLP_{139\ 151}$ purity >95% (Pepceuticals Ltd., UK) together with Complete Freund's Adjuvant and heat-killed Mycobacterium

tuberculosis (H37Ra, Difco). Bordetella pertussis toxin (250 ng; List Biological Laboratories, US) was administered intraperitoneally at days 0 and 2. Mice were assigned a clinical score daily: 0, no disease; 1, tail weakness; 2, paraparesis; 3, paraplegia; 4, paraplegia with forelimb weakness; 5, moribund or dead animals.

In vivo MRI

Shortly before and during the MR session, mice were anesthetized using a mixture of isoflurane as inhalation narcosis (0.5 1.5%), pressurized air and oxygen. All MRI-scans were performed on a Bruker Biospec 9.4T USR94/20 (Bruker, Ettlingen, Germany). Mice were imaged using a Transceiver Mouse Brain CryoProbe (Z106543, 400 MHz, Bruker BioSpin MRI, Ettlingen, Germany). The CryoProbe is a half-cylindrical-shaped 2-channel transmit/receive quadrature-driven surface coil, for full mouse-brain coverage with a maximum field of view of c. 30×20×20 mm. The temperature of the mice was regulated at 37°C. The breathing rate and temperature was monitored by a remote monitoring system (Model 1025, SA Instruments Inc., Syracuse, New York, USA). Images were acquired using T_1-weighted (T1W), T_2-weighted (T2W) and T_2*-weighted (T2*W) techniques. Slice positioning was kept fixed through longitudinal brain examination: axial slices were positioned parallel to the base of the brain, coronal slices were positioned perpendicular to axial slices and covering the brain from the olfactory bulb/frontal lobe fissure to the cervical spinal cord.

MRI sequences

Pre and post contrast T1W imaging was done with a Modified Driven-Equilibrium Fourier Transformation sequence (MDEFT) (3D MDEFT: TR/TE/TI: 3000/3.9/950 ms, FA 20°, matrix 384×384). Horizontal sections of the entire mice brain were performed in 11 min at a spatial resolution of (47×47×400) μm^3. Coronal sections were performed in 15 min at a spatial resolution of (47×47×500) μm^3. As T_1-enhancing contrast agent gadolinium diethylenetriamine penta-acetate (Gd-DTPA, Magnevist, Bayer-Schering Pharma AG, Berlin, Germany) was administered intravenously at a concentration of 0.2 mmol/kg. T2W scans (2D TurboRARE: TR/TE: 3000/43 ms, matrix 384×384) were performed in 5 min with geometry and spatial resolution identical to that of T1W imaging. To image brain tissue in association with the microvasculature we applied a T2*W multislice fast low angle shot (2D FLASH: TR/TE: 473/18 ms, FA 40°, matrix 512×512) sequence with an in plane resolution of (35×35) μm^2. For horizontal scans we used a slice thickness of 400 μm and 16 slices for full brain coverage with a scan time of 8 min and for coronal scans we used 22 slices of 500 μm with a scan time of 11 min to image the whole mouse brain. For mice showing leakage of contrast agent, a 29 min 3D FLASH sequence with flow compensation (GEFC: TR/TE: 30/5.9 ms, matrix 512×256×256) was applied, for visualization of the vasculature and ventricular system 1 hr after contrast injection at an isotropic spatial resolution of 59 μm.

The following MRI sequences were used for the baseline scans, prior to immunization: TurboRARE, MDEFT, 2D FLASH and 3D GEFC. Five days post-immunization, the mice underwent daily horizontal and coronal T2W (TurboRARE) scans. If no lesions or clinical signs were observed, the mouse was returned to the home cage and scanned again the next day. If hypo- or hyperintense lesions were detected, then 2D FLASH and MDEFT pre-contrast scans of that mouse were done immediately. The mouse was then injected i.v. with Gd-DPTA, and post-contrast MDEFT, TurboRARE and 3D GEFC scans were done (15, 45, and 55 minutes following contrast injection, respectively). If the mouse did not show clinical signs, regardless of the observation of lesions, it was returned to the home cage and scanned again the next day. If the mouse did show clinical signs, this was the pre-defined endpoint, the mouse was sacrificed on the same day, and the brain extracted for histological comparison. Given the inherent variability in the time of onset of EAE, we elected to use this design (**Figure S1**), customized for each individual animal, rather than use a pre-selected timetable.

Image analysis

Images from longitudinal experiments in mouse EAE were analyzed by three individuals who were blinded towards disease activity of corresponding mice. Lesions on T2W images were defined as described for T2W lesions in MS patients [40]. Briefly, lesions had to be clearly visible, non-artifactual areas of change in the signal intensity (signal enhancement or extinction on the grey background) of T2W images compared to baseline T2W images (taken prior to EAE immunization). To generate susceptibility weighted images post processing of the phase maps derived from T2*W imaging for was performed by fully-automated reconstruction using ParaVision 5.1 (Bruker, Ettlingen, Germany).

Histology

After terminal anesthesia, mice were transcardially perfused with 20 ml PBS, then with 20 ml zinc fixation solution (0.5% zinc acetate, 0.5% zinc chloride, 0.05% calcium acetate). Brains were then extracted and subsequently post-fixed in zinc solution for 3 d at room temperature. The tissues were then cryoprotected by incubation overnight at 4 degrees in 30% sucrose in PBS, then embeded in O.C.T. and frozen in methylbutane with dry ice. The tissues were cut into 12 um sections on a cryostat, and stained with hematoxylin and eosin according to standard procedures. For immunostaining, tissue sections were blocked with avidin, biotin, and normal goat serum, then incubated overnight at 4°C with rat anti-mouse CD4 antibody (Invitrogen). The sections were then incubated with biotinylated goat anti-rat IgG antibody (Vector Laboratories), then streptavidin-conjugated peroxidase, and visualized with Vector NovaRED Peroxidase substrate (Vector Laboratories) and counterstained with hematoxylin.

Supporting Information

Figure S1 Flow chart illustrating the design of the μMRI study in EAE mice. Following a baseline scan, mice were immunized and scanned daily (horizontal and coronal T2W MRI) 5 d post-immunization. More intensive scans were performed and contrast (Gd-DPTA) was i.v. applied when lesions were detected with T2W MRI.
(TIF)

Figure S2 EAE scores compared with day of lesion occurrence. The neurological score of each mouse is plotted against the day of first lesion occurrence (d-1 denotes that lesions were first observed one day prior to onset of symptoms).
(TIF)

Figure S3 Cerebellar changes during course of EAE. T2W images using a TurboRARE sequence (TR/TE 3000/43 ms, FOV 18×18 mm, Matrix 512×512 (384×384 for d-14), RARE-factor 8) showing the evolution of cerebellar lesions from baseline (pre EAE induction) 14 days prior to disease manifestation (d-14) until disease onset (d0) including daily scans starting from day 5 (d-5) prior disease onset. Dotted islands depict signal changes in the white-matter of the cerebellum.
(TIF)

Figure S4 Parenchymal and vascular changes following EAE induction. (A) T2W images using a TurboRARE sequence TR/TE 3000/43 ms, FOV 18×18 mm, Matrix 512×512 (384×384 for baseline), RARE-factor 8). Top row: baseline; middle row: pre-symptomatic image revealing a hyperintense lesion in the cortex; bottom row: subtracted image. (B) SWI processed T2*W images using a FLASH multislice sequence (TR/TE of 473/18 ms, FOV 18×18 mm, acquisition Matrix 512×512). Top row: baseline; middle row: pre-symptomatic image showing vascular irregularities in the region of the T2 hyperintense lesion shown in (A); bottom row: subtracted image.
(TIF)

Figure S5 Maximum intensity projections (MIP) pre and post contrast administration in a healthy non-immunized mouse. (A) Pre-contrast MIP of a 3D-GEFC sequence (TR/TE: 30/5.9 ms, matrix 512×256×256). (B) Post-contrast MIP of the same mouse.
(TIF)

Figure S6 Differences in quality and scan duration between images showing cortical hypointense lesions in EAE brains using either a cryogenically cooled coil (A, C) or a room temperature (RT) 18 mm mouse-head birdcage coil (B, D). (A) T2W images using a TurboRARE sequence with cryogenic coil (TR/TE 3000/36 ms, FOV 18×18 mm, Matrix 384×384) (B) T2W images using a TurboRARE sequence with RT coil (TR/TE 2000/30 ms, FOV 24×14 mm, Matrix 300×174) (C) T2*W images using a FLASH multislice sequence with cryo coil (TR/TE of 473/18 ms, FOV 18×18 mm, acquisition Matrix 512×512) (D) T2*W images using a FLASH multislice sequence with RT coil (TR/TE of 473/13 ms, FOV 24×14 mm, acquisition Matrix 330×192).
(TIF)

Acknowledgments

We thank Julia Skodowski, Bibiane Seeger and Stefanie Balz for excellent technical support.

Author Contributions

Conceived and designed the experiments: HW JM TN SW. Performed the experiments: HW JM SL. Analyzed the data: HW JM SL SW. Contributed reagents/materials/analysis tools: TN SW AP CID. Wrote the paper: SW HW JM AP TN.

References

1. Trapp BD, Nave KA (2008) Multiple sclerosis: an immune or neurodegenerative disorder? Annu Rev Neurosci 31: 247 269.
2. Stadelmann C (2011) Multiple sclerosis as a neurodegenerative disease: pathology, mechanisms and therapeutic implications. Curr Opin Neurol 24: 224 229.
3. Charil A, Filippi M (2007) Inflammatory demyelination and neurodegeneration in early multiple sclerosis. J Neurol Sci 259: 7 15.
4. Engelhardt B, Coisne C (2011) Fluids and barriers of the CNS establish immune privilege by confining immune surveillance to a two-walled castle moat surrounding the CNS castle. Fluids Barriers CNS 8: 4.
5. Alvarez JI, Cayrol R, Prat A (2011) Disruption of central nervous system barriers in multiple sclerosis. Biochim Biophys Acta 1812: 252 264.
6. Hauser SL, Waubant E, Arnold DL, Vollmer T, Antel J, et al. (2008) B-cell depletion with rituximab in relapsing-remitting multiple sclerosis. N Engl J Med 358: 676 688.
7. Paul F, Waiczies S, Wuerfel J, Bellmann-Strobl J, Dorr J, et al. (2008) Oral high-dose atorvastatin treatment in relapsing-remitting multiple sclerosis. PLoS ONE 3: e1928.
8. Wuerfel J, Tysiak E, Prozorovski T, Smyth M, Mueller S, et al. (2007) Mouse model mimics multiple sclerosis in the clinico-radiological paradox. Eur J Neurosci 26: 190 198.
9. Levy H, Assaf Y, Frenkel D (2010) Characterization of brain lesions in a mouse model of progressive multiple sclerosis. Exp Neurol 226: 148 158.
10. Vellinga MM, Oude Engberink RD, Seewann A, Pouwels PJ, Wattjes MP, et al. (2008) Pluriformity of inflammation in multiple sclerosis shown by ultra-small iron oxide particle enhancement. Brain 131: 800 807.
11. Wuerfel J, Bellmann-Strobl J, Brunecker P, Aktas O, McFarland H, et al. (2004) Changes in cerebral perfusion precede plaque formation in multiple sclerosis: a longitudinal perfusion MRI study. Brain 127: 111 119.
12. Weissleder R, Cheng HC, Bogdanova A, Bogdanov A (1997) Magnetically labeled cells can be detected by MR imaging. J Magn Reson Imaging 7: 258 263.
13. Dousset V, Gomez C, Petry KG, Delalande C, Caille JM (1999) Dose and scanning delay using USPIO for central nervous system macrophage imaging. MAGMA 8: 185 189.
14. Floris S, Blezer EL, Schreibelt G, Dopp E, van der Pol SM, et al. (2004) Blood-brain barrier permeability and monocyte infiltration in experimental allergic encephalomyelitis: a quantitative MRI study. Brain 127: 616 627.
15. Oude Engberink RD, Blezer EL, Dijkstra CD, van der Pol SM, van der TA, et al. (2010) Dynamics and fate of USPIO in the central nervous system in experimental autoimmune encephalomyelitis. NMR Biomed 23: 1087 1096.
16. Tysiak E, Asbach P, Aktas O, Waiczies H, Smyth M, et al. (2009) Beyond blood brain barrier breakdown - in vivo detection of occult neuroinflammatory foci by magnetic nanoparticles in high field MRI. J Neuroinflammation 6: 20.
17. Aguayo JB, Blackband SJ, Schoeniger J, Mattingly MA, Hintermann M (1986) Nuclear magnetic resonance imaging of a single cell. Nature 322: 190 191.
18. Benveniste H, Blackband S (2002) MR microscopy and high resolution small animal MRI: applications in neuroscience research. Prog Neurobiol 67: 393 420.
19. Hoult DI, Richards RE (1976) The signal-to-noise ratio of the nuclear magnetic resonance experiment. J Magn Reson (1969) 24: 71 85.
20. Cleary JO, Wiseman FK, Norris FC, Price AN, Choy M, et al. (2011) Structural correlates of active-staining following magnetic resonance microscopy in the mouse brain. Neuroimage 56: 974 983.
21. Kovacs H, Moskau D, Spraul M (2005) Cryogenically cooled probes - a leap in NMR technology. Prog Nucl Magn Reson Spectrosc 46: 131 155.
22. Nouls JC, Izenson MG, Greeley HP, Johnson GA (2008) Design of a superconducting volume coil for magnetic resonance microscopy of the mouse brain. J Magn Reson 191: 231 238.
23. Baltes C, Radzwill N, Bosshard S, Marek D, Rudin M (2009) Micro MRI of the mouse brain using a novel 400 MHz cryogenic quadrature RF probe. NMR Biomed 22: 834 842.
24. Haacke EM, Xu Y, Cheng YC, Reichenbach JR (2004) Susceptibility weighted imaging (SWI). Magn Reson Med 52: 612 618.
25. Haacke EM, Makki M, Ge Y, Maheshwari M, Sehgal V, et al. (2009) Characterizing iron deposition in multiple sclerosis lesions using susceptibility weighted imaging. J Magn Reson Imaging 29: 537 544.
26. Steinman L, Zamvil SS (2006) How to successfully apply animal studies in experimental allergic encephalomyelitis to research on multiple sclerosis. Ann Neurol 60: 12 21.
27. Ben Nun A, Wekerle H, Cohen IR (1981) Vaccination against autoimmune encephalomyelitis with T-lymphocyte line cells reactive against myelin basic protein. Nature 292: 60 61.
28. Hickey WF, Kimura H (1988) Perivascular microglial cells of the CNS are bone marrow-derived and present antigen in vivo. Science 239: 290 292.
29. Engelhardt B, Wolburg-Buchholz K, Wolburg H (2001) Involvement of the choroid plexus in central nervous system inflammation. Microsc Res Tech 52: 112 129.
30. Reboldi A, Coisne C, Baumjohann D, Benvenuto F, Bottinelli D, et al. (2009) C-C chemokine receptor 6-regulated entry of TH-17 cells into the CNS through the choroid plexus is required for the initiation of EAE. Nat Immunol 10: 514 523.
31. Bartholomaus I, Kawakami N, Odoardi F, Schlager C, Miljkovic D, et al. (2009) Effector T cell interactions with meningeal vascular structures in nascent autoimmune CNS lesions. Nature 462: 94 98.
32. Ransohoff RM (2009) Immunology: In the beginning. Nature 462: 41 42.
33. Budde MD, Kim JH, Liang HF, Russell JH, Cross AH, et al. (2008) Axonal injury detected by in vivo diffusion tensor imaging correlates with neurological disability in a mouse model of multiple sclerosis. NMR Biomed 21: 589 597.
34. Nessler S, Boretius S, Stadelmann C, Bittner A, Merkler D, et al. (2007) Early MRI changes in a mouse model of multiple sclerosis are predictive of severe inflammatory tissue damage. Brain 130: 2186 2198.
35. Ratering D, Baltes C, Nordmeyer-Massner J, Marek D, Rudin M (2008) Performance of a 200-MHz cryogenic RF probe designed for MRI and MRS of the murine brain. Magn Reson Med 59: 1440 1447.
36. Wright AC, Song HK, Wehrli FW (2000) In vivo MR micro imaging with conventional radiofrequency coils cooled to 77 degrees K. Magn Reson Med 43: 163 169.
37. Wuerfel E, Infante-Duarte C, Glumm R, Wuerfel JT (2010) Gadofluorine M-enhanced MRI shows involvement of circumventricular organs in neuroinflammation. J Neuroinflammation 7: 70.

38. Mueggler T, Pohl H, Baltes C, Riethmacher D, Suter U, et al. (2011) MRI signature in a novel mouse model of genetically induced adult oligodendrocyte cell death. Neuroimage.
39. Pohl HB, Porcheri C, Mueggler T, Bachmann LC, Martino G, et al. (2011) Genetically induced adult oligodendrocyte cell death is associated with poor myelin clearance, reduced remyelination, and axonal damage. J Neurosci 31: 1069 1080.
40. Tan IL, van Schijndel RA, Fazekas F, Filippi M, Freitag P, et al. (2002) Image registration and subtraction to detect active T(2) lesions in MS: an interobserver study. J Neurol 249: 767 773.

OPEN ACCESS Freely available online

PLOS ONE

Enlargement of Cerebral Ventricles as an Early Indicator of Encephalomyelitis

Stefano Lepore[1,2☯], Helmar Waiczies[1,2☯], Jan Hentschel[1], Yiyi Ji[1], Julia Skodowski[1,2], Andreas Pohlmann[1], Jason M. Millward[2,3], Friedemann Paul[4], Jens Wuerfel[4,5], Thoralf Niendorf[1,2], Sonia Waiczies[1,2*]

1 Berlin Ultrahigh Field Facility (B.U.F.F.), Max Delbrueck Center for Molecular Medicine, Berlin, Germany, **2** Experimental and Clinical Research Center (ECRC), a joint cooperation between the Charité Universitätsmedizin Berlin and the Max Delbrueck Center for Molecular Medicine, Berlin, Germany, **3** Institute for Medical Immunology, Charité Universitätsmedizin Berlin, Berlin, Germany, **4** NeuroCure Clinical Research Center, Charité Universitätsmedizin Berlin, Berlin, Germany, **5** Institute of Neuroradiology, University Medicine, Göttingen, Göttingen, Germany

Abstract

Inflammatory disorders of the central nervous system such as multiple sclerosis and acute disseminated encephalomyelitis involve an invasion of immune cells that ultimately leads to white matter demyelination, neurodegeneration and development of neurological symptoms. A clinical diagnosis is often made when neurodegenerative processes are already ongoing. In an attempt to seek early indicators of disease, we studied the temporal and spatial distribution of brain modifications in experimental autoimmune encephalomyelitis (EAE). In a thorough magnetic resonance imaging study performed with EAE mice, we observed significant enlargement of the ventricles prior to disease clinical manifestation and an increase in free water content within the cerebrospinal fluid as demonstrated by changes in T_2 relaxation times. The increase in ventricle size was seen in the lateral, third and fourth ventricles. In some EAE mice the ventricle size started returning to normal values during disease remission. In parallel to this macroscopic phenomenon, we studied the temporal evolution of microscopic lesions commonly observed in the cerebellum also starting prior to disease onset. Our data suggest that changes in ventricle size during the early stages of brain inflammation could be an early indicator of the events preceding neurological disease and warrant further exploration in preclinical and clinical studies.

Citation: Lepore S, Waiczies H, Hentschel J, Ji Y, Skodowski J, et al. (2013) Enlargement of Cerebral Ventricles as an Early Indicator of Encephalomyelitis. PLoS ONE 8(8): e72841. doi:10.1371/journal.pone.0072841

Editor: Robyn Klein, Washington University, United States of America

Received March 11, 2013; **Accepted** July 15, 2013; **Published** August 22, 2013

Funding: This work was supported by a university grant from the Experimental and Clinical Research Center (ECRC2010-2013), a research grant from Novartis and research grants from the German Research Foundation (DFG Exc 257 to FP, WA 2804/1-1 to SW). The funders had no role in study design, data collection and analysis, decision to publish, or preparation of the manuscript.

Competing interests: The authors have declared that no competing interests exist.

* E-mail: sonia.waiczies@charite.de

☯ These authors contributed equally to this work.

Introduction

Under normal physiological conditions, immunologically competent CNS resident cells, such as microglia, or immune cells derived from the peripheral circulation serve to protect the CNS against potentially harmful infectious agents or traumatic events [1–3]. Blood-borne immune cells, including memory T cells, are limited to the leptomeningeal, perivascular and ventricular cerebrospinal fluid (CSF) spaces [2,3]. In the healthy brain, the CSF compartment appears to be the only site where memory T cells localize to in the CNS [4], their presence persisting for several years [3]. The CSF compartment indeed assumes an important role for immune surveillance [5,6] as the site where activated T cells can communicate with resident antigen-presenting cells [7,8]. The passage of CD4+ memory T cells into the CSF compartment occurs following their extravasation via microvascular structures of the choroid plexus into the cerebral ventricles or alternatively via postcapillary venules into leptomeningeal and perivascular Virchow–Robin (VRS) spaces [5].

Although CD4+ memory T cells can easily enter the CSF compartment, their entry into the CNS parenchyma is restricted by the blood brain barrier (BBB), which consists of the cerebral vessel endothelial cells and surrounding glia limitans. During autoimmune encephalomyelitis, such as occurs in multiple sclerosis (MS), the BBB is transformed and its function altered, e.g. by the action of several inflammatory molecules [9,10]. Following activation of the BBB, T cells now gain access to the brain parenchyma via a multi-step process that involves crossing both, the vascular endothelium and the glia limitans [11]. This inflammatory cell invasion into the VRS precedes perivascular cuffing that ultimately leads to inflammatory and

demyelinating lesions. These prominent pathological patterns have long been documented histologically in MS autopsy material [12]. Specific pathological changes such as enlargement of the VRS, can be detected in MS brains with magnetic resonance imaging (MRI) [13], making it possible to detect [14] and quantify [15] these changes during the development of MS disease.

Recently, cryogenically-cooled ^{1}H coils have started gaining momentum in preclinical microscopic (micro) MR neuro- and cardiovascular imaging due to an improved signal-to-noise ratio compared to traditional room temperature ^{1}H coils [16–18]. Using the experimental model of autoimmune encephalomyelitis (EAE) and a cryogenically-cooled ^{1}H coil, we recently were able to detect and follow pathological changes in the CNS prior to onset of clinically detectable disease signs [19]. In this study we were able to define changes in the brain of immunized mice that corresponded to cellular infiltrates in immunohistology. Moreover, after Gd-DTPA administration we observed that contrast agent (CA) distributed not only into lesions but also into the ventricular compartment in most EAE animals [19].

Here, we employed the cryogenically-cooled ^{1}H coil to identify both micro- and macroscopic changes prior to clinical onset and during manifestation of disease in EAE using a larger cohort of animals. To study microscopic changes, we focused on the evolution of cerebellar lesions, which are the most common pre-symptomatic lesions in the EAE. The main macroscopic alteration in the EAE brain is a prominent and sustained increase in cerebral ventricle size. We therefore followed up changes in ventricle volume as well as T_2 relaxation times of ventricular CSF (since this has been shown to correlate with methods measuring direct water concentration in the brain [20,21]) prior to and after clinical disease onset.

Material and Methods

Induction of EAE

Female SJL/J mice were purchased from Janvier (Janvier SAS, Le Genest-St-Isle, France). For active EAE, 22 mice (12 weeks old) were immunized subcutaneously with 250 µg PLP (Pepceuticals Ltd., UK) and 800 µg mycobacterium tuberculosis H37Ra (Difco) in 200 µl emulsion containing equal volumes of phosphate/buffered saline (PBS) and complete Freunds adjuvant (BD-Difco), as previously described [22] 200 ng pertussis toxin (List Biological Laboratories, US) were administered intraperitoneally at days 0 and 2. Six mice were used as normal controls. An additional 6 mice were used for sham immunizations; for this we employed the same protocol used for EAE induction but omitted PLP. Mice were weighed and scored daily as follows: 0, no disease; 1, tail weakness and righting reflex weakness; 2, paraparesis; 3, paraplegia; 4, paraplegia with forelimb weakness or paralysis; 5, moribund or dead animal. Mice with a score of 2.5 or more received an intraperitoneal injection of 200 µl glucose (5%) daily and mice with a score of 3 for more than 24 hours were sacrificed. Animals used as controls were healthy untreated mice. Animal experiments were carried out in accordance with the guidelines provided and approved by the Animal Welfare Department of the LAGeSo State Office of Health and Social Affairs Berlin (Permit G-0172/10: MR Bildgebung d. Therapieansätze - EAE 09.2010 - 09.2013).

Magnetic Resonance Imaging

Mice were imaged before EAE immunization and daily (at the same time of day) between 5 and 18 days after active EAE induction. MRI was performed using a 9.4 Tesla animal scanner (Biospec 94/20 USR, Bruker Biospin, Ettlingen, Germany) and a cryogenically-cooled quadrature-resonator (CryoProbe, Bruker Biospin, Ettlingen, Germany). Mice were placed on a water circulated heated holder to ensure constant body temperature of 37 °C and kept anesthetized using a mixture of isoflurane 1–1.5% (Abbott GmbH & Co. KG, Wiesbaden, Germany), air and oxygen. Body temperature and breathing rate were constantly checked by a remote monitoring system (Model 1025, SA instruments Inc., New York, USA).

Horizontal and coronal fat suppressed turbo spin echo T_2-weighted TurboRARE (TE = 36 ms, TR = 3000 ms, matrix = 384 × 384, FOV = 1.8 cm, NEX = 2, coronal slices = 22, slice thickness = 0.5 mm, scan time = 5 min, axial slices = 16, slice thickness = 400 µm, scan time = 5 min) brain images were acquired. Slice positioning was kept fixed through the longitudinal brain examination: horizontal slices were positioned parallel to the base of the brain, coronal slices were positioned perpendicularly to horizontal slices and covering the brain from the olfactory bulb/frontal lobe fissure to the cervical spinal cord. For parametric mapping of the relaxation time T_2 a multislice-multi-echo (MSME) technique (TR = 1500 ms, matrix = 256x 256, FOV = 1.8 cm, NEX = 2, slice = 1, scan time = 15 min) was used. For this purpose echo times (TE) ranging from (10–80) ms were used to vary T_2-weighting in increments of 10 ms. The slice was positioned horizontally using as reference the horizontal TurboRARE geometry covering cortex, caudate putamen, hippocampus, cerebellum and lateral, third and fourth ventricles.

Brain Segmentation

Quantification of ventricle size was performed using FSL5.0 (FMRIB's Software Library, www.fmrib.ox.ac.uk/fsl) [23–25]. All T_2-weighted images were corrected for bias field inhomogeneity and cleared of non-brain tissue using the brain extraction tool (BET) of FSL [26]. One brain image set was chosen as reference and processed using an automated image segmentation tool (FAST) to obtain a ventricle mask [27]. Subsequently all other brain images were registered to the reference brain using FMRIB's Linear Image Registration Tool (FLIRT) to generate an inverse transformation matrix [28]. This matrix was afterwards applied to the reference ventricles mask to map the ventricle size of each animal. To investigate volume changes in each ventricle separately a mask for each different ventricle was generated starting from the ventricle reference mask. The obtained masks were then used to calculate the single ventricle volume as described above. Ventricle size was calculated as total µl volume within segmented ventricles and the ventricle volume changes was estimated as a ratio of each day ventricle volume to pre immunization ventricle volume.

Brain tissue volume was manually measured by three independent investigators in 2 animals per group (EAE mice, ventricle normalizing mice and control group), on 2 adjacent slices where it was possible to clearly depict the lateral ventricles and the caudate putamen, the most evident brain regions subjected to volume changes. For each slice, the parenchymal volume was calculated subtracting the volume of the ventricles from the volume of the whole brain area.

MR Relaxometry

Maps of absolute T_2 relaxation times were calculated by pixel-wise mono-exponential fitting, implemented in an in-house developed MATLAB program. To quantify the T_2 relaxation times in the CSF within the ventricular compartment for each obtained map, a mask of the ventricles cleared of the choroid plexus was generated using the FAST tool of FSL. To minimize the influence of partial volume effects generated from neighboring brain tissue, we eroded the automatically generated mask by two voxels. T_2 relaxation time of the ventricular CSF was calculated as the mean T_2 relaxation time for all pixels within the mask.

Data analysis

Three independent blinded investigators were involved in the analysis of the MRI data. All data were thereafter statistically analyzed using GraphPad Prism (GraphPad Software, Inc., La Jolla, CA, USA). The onset of cerebellar lesions was determined by manual inspection. With regards to the onset of ventricle enlargement, a minimum of 10% volume increase from the pre-immunization (baseline) volume was used as threshold. The ventricle normalizing animals were defined as those showing a 10% reduction from the maximum observed ventricular volume. Differences between EAE mice and controls regarding ventricular enlargement and T_2 relaxation time were analyzed by the student t-test. To compare the onset of cerebellar lesions and ventricular enlargement with the onset of disease we employed a paired t-test since these parameters represent repeated measurements of the same individual mice over time. A p-value of $p<0.05$ was considered to be statistically significant. A log-rank (Mantel-Cox) test was used to analyze the time-to-event curves and compare the onset of clinical symptoms, cerebellar lesions and ventricle enlargement.

Results

Ventricle enlargement before manifestation of neurological disease

In this study we followed brain modifications during the development of active EAE in a large group of mice (n=20). The first distinct macroscopic change we observed on T_2-weighted images was an increase in cerebral ventricle size without manifestation of clinical disease (Figure **1A, 1B**). Figure 1A shows a representative mouse (mouse 8 in Figure **1B**) in which ventricle enlargement was detected two days before start of symptoms (d -2). In this EAE mouse we also observed a decrease in ventricle size, three days (d +3) following the symptom onset, defined as the first day of evident motor impairment (tail weakness). Figure 1B summarizes the time-line for all investigated EAE mice and indicates the first day of volume changes in the ventricles in relation to the symptom onset post EAE induction (immunization with CNS antigen).

All immunized mice eventually developed symptomatic EAE. The average day of disease clinical manifestation was 10.8 ± 1.1 (± S.D.) days post immunization, comparable to previous studies [19]. 19 out of 20 mice studied showed an increase in ventricle size and in 16 of these 19 animals, the ventricle enlargement was observed prior to disease manifestation, notably the increase could be detected even up to five days prior to symptom manifestation (mouse 1). In two cases the ventricle enlargement coincided with the symptom onset. On average, EAE mice exhibited an increase in ventricle size 1.6 ±1.2 (± S.D.) days before the first symptom.

Cerebellar lesion evolution during disease development

Both hyperintense and hypointense lesions could be detected in multiple brain areas prior to disease manifestation in EAE, however, most commonly hyperintense lesions in the cerebellum [19]. We here investigated the temporal changes of these lesions by T_2-weighted micro MRI, keeping our main focus on the cerebellum (Figure **2**). Figure 2A shows a representative EAE mouse (mouse 7 in Figure **2B**), in which lesions were identified in the white matter of the cerebellum as hyper-intense regions (Figure **2A**, asterisks) on T_2-weighted images; these lesions were detected already 3 days before clinical disease onset (d -3). The shape and spatial distribution of these lesions changed over time, also involving other areas of the *arbor vitae* (d -2 and d -1). Some lesions, especially those surrounding small vessels, turned hypo-intense (Figure **2A**, white arrows) and appeared to partially resolve two days after the first neurological symptoms (d +2). Figure 2B recapitulates the temporal differences between the time of first appearance of cerebellar lesions and the time of first symptom manifestation in all EAE mice. Out of 20 animals that developed EAE, 18 showed pre-symptomatic cerebellar lesions on average 2.5 (±1.09 S.D.) days before the first manifestation of clinical signs. Lesion appearance could be observed up to 5 days before disease onset (mouse 1). With the exception of two animals, that did not develop micro MRI visible pathology within the cerebellum, EAE mice commonly manifested early lesions at least one day before appearance of clinical symptoms. Of note, the only mouse that developed clinical disease but no evident changes on MRI (mouse 20) was not only devoid of cerebellar lesions but also exhibited no ventricle enlargement.

The average day of first ventricle size increase was 8.7 ± 2.7 days (± S.D.) post immunization (p.i.) and the average day of first cerebellar lesion occurrence was 7.3 ± 2.8 days (± S.D.) p.i., in comparison to the average day of clinical disease onset, which was 10.8 days p.i. (see above) (Figure **S1A**). We next wanted to determine the fraction of EAE mice undergoing each of these events over the period of time after immunization. We plotted time-to-event curves for first appearance of (i) clinical signs, (ii) ventricular enlargement and (iii) cerebellar lesions

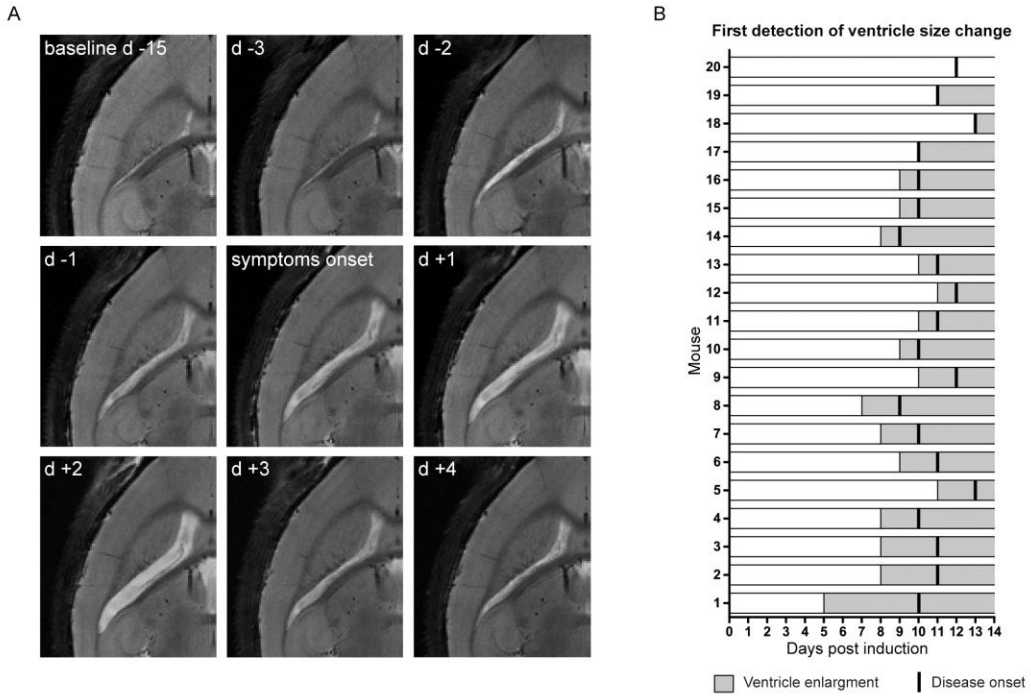

Figure 1. Pre-symptomatic changes in ventricle size in an EAE mouse model. (A) T_2-weighted horizontal views of the mouse brain show the evolution of changes in ventricle size of a representative mouse from baseline (pre EAE induction) 15 days prior (d-15) to disease manifestation up till 4 days after disease manifestation (d +4). (B) Shown are 20 mice (1–20) exhibiting increase in ventricle volume prior to or concurrent to disease onset. For each animal, gray bars represent the first occurrence of ventricle enlargement and ensuing time points following EAE induction and black vertical lines indicate the symptom onset post immunization. The animals were sorted according to the time difference between first changes in ventricle size (light gray bars) and onset of clinical symptoms post immunization (black vertical lines). Mouse 1 exhibited ventricle enlargement 5 days prior to clinical symptoms, Mouse 17 – Mouse 19 exhibited ventricle enlargement on the same day as clinical symptoms and Mouse 20 showed no ventricle enlargement.

doi: 10.1371/journal.pone.0072841.g001

against the time span after immunization (Figure **S1B**). We observed that both cerebellar lesions and ventricular enlargement occurred significantly earlier than the appearance of clinical signs (Figure **S1B**); cerebellar lesions vs. clinical signs, $p < 0.0001$; ventricular enlargement vs. clinical signs, $p = 0.0064$.

Changes in clinical scores are preceded by changes in ventricle size

Next we compared the changes in ventricle volume with EAE signs and symptoms (weight and EAE score) during the progression of disease. Hence, for each mouse, we synchronized all 3 parameters (weight, clinical score and ventricle volume) to the day of first neurological symptoms, defined as time point 0 (Figure **3**). The animal weight started decreasing 3-4 days before disease manifestation and started returning to normal 3-4 days after initiation of symptoms (Figure **3A**). The average score at peak of disease severity was 1.9 ± 0.7 (± S.D.). The maximum was usually reached within the first 3 days following disease manifestation (Figure **3B**).

We normalized the ventricle volumes of each time point to the baseline values (d -15) and plotted the changes in ventricle size over the disease course (Figure **3C**), similar to the weight and score curves. The average mean size of the ventricles at baseline was 10.7 ± 1.1 (± S.D.) mm^3. In contrast to the non-immunized control mice, the ventricle size of EAE animals started to increase in size on average already two days before clinical symptoms and in some cases expanding 2 times more than baseline volume. For all EAE animals, we compared (i)

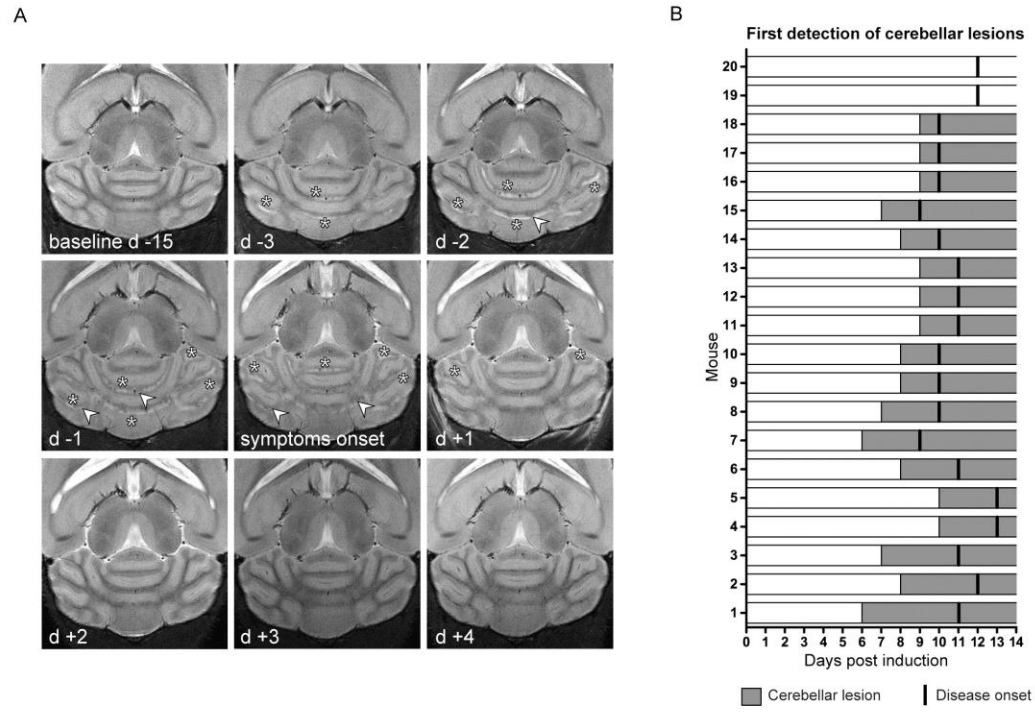

Figure 2. Pre-symptomatic development of cerebellar lesion in an EAE mouse model. (A) T_2-weighted horizontal views of the mouse cerebellum, which show the temporal progression of lesions in the *arbor vitae* of the cerebellum of a representative mouse starting from pre EAE induction 15 days before clinical symptoms (baseline d-15) up till 2 days after disease manifestation (d +2); stars highlights hyperintense lesion appearance, arrowheads points to the hypointense lesions. (B) Graph showing the first day when cerebellar modifications were observed (gray bars) and the symptom onset (black vertical lines) for all animals in the study. The *x*-axis indicates the time points after EAE induction (0). The animals were sorted according to the time difference between first occurrence in cerebellar lesions and the onset of clinical symptoms post immunization. Mouse 1 exhibited cerebellar lesions 5 days prior to clinical symptoms, Mouse 19 and Mouse 20 showed no cerebellar lesions.

doi: 10.1371/journal.pone.0072841.g002

disease severity and magnitude of ventricular enlargement (Figure **S2A**), (ii) weight loss and magnitude of ventricular enlargement (Figure **S2B**) and (iii) disease severity and onset of ventricular enlargement (Figure **S2C**). However, we did not observe any correlation between the onset or magnitude of ventricular enlargement and the different clinical disease measures.

Notably, in 3 EAE mice (8, 9 and 14 in Figure **1B**), the ventricle size started returning to normal values during disease remission (Figure **3F**). In these EAE mice a reduction in ventricle size started on average 3 days after disease manifestation, at the same time as the peak of symptoms, thus preceding disease remission (Figure **3F**). Although these three mice showed a significant reduction in ventricle size during the remission of the disease (in parallel to the increase in average weight (Figure **3D**), and a decrease in disease score (Figure **3E**), we could not observe any significant differences in the disease scores between these three cases and the rest of the cohort.

Although the present findings occur at an early stage of disease, several days prior to symptom onset, it remains to be excluded that ventricle enlargement occurs as a consequence of brain atrophy, i.e. cell death. Therefore, we followed changes over time in the brain parenchyma volume in mice within the ventricle non-normalizing group and those within the ventricle normalizing group. In comparison to control mice, the group of mice with sustained ventricular enlargement showed a significant decrease in brain volume (Figure **S3A**), interestingly after the time point showing significant enlargement in ventricles (Figure **3C**). In the ventricle normalizing animal group, relative brain parenchymal volumes remained constant. These results suggest that ventricular expansion may be

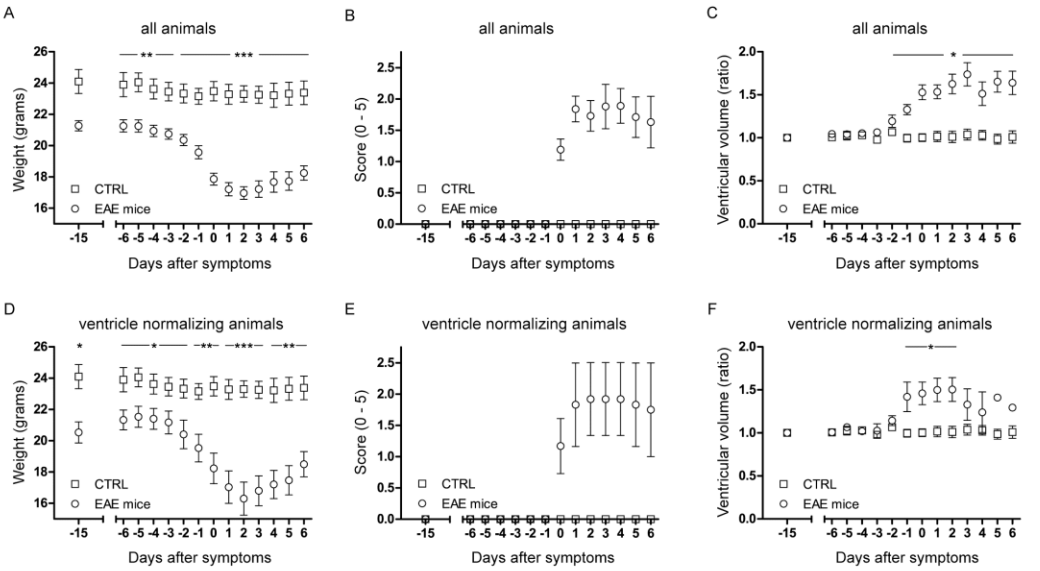

Figure 3. Time-line for weight, score and ventricle volume during EAE development. All the animals were weighed and scored before EAE induction and daily starting from the day of immunization onwards. At baseline and then starting from day 5 after EAE induction micro MRI measurements were performed and the ventricle volumes measured. Graph shows the temporal changes in weight (A), score (B) and ventricle volume (C) for control mice (n=6) and EAE mice (n=20) synchronized to the first day of clinical symptoms. (D) Weight, (E) score and (F) ventricle volume changes of EAE animals that showed remission in ventricle enlargement (n=3) against control animals (n=6).

doi: 10.1371/journal.pone.0072841.g003

accompanied by compression of the brain parenchyma (Figure **S3B**).

To investigate the possibility that mechanical obstruction between the ventricles (e.g. due to lesion formation) could explain the changes in ventricular volume we calculated the size of each of all four ventricles independently and over time (Figure **4**). All ventricles showed a volume increase before the symptom onset. However, the change in volume in the combined lateral ventricles (Figure **4A**), left ventricle alone (Figure **4B**) and right ventricle alone (Figure **4C**) was much more pronounced than the change in volume in the third (Figure **4D**) and fourth ventricle (Figure **4E**).

In order to exclude the possibility of ventricular changes occurring due to non-specific effects of the adjuvants used during immunization [29], we immunized 6 mice following the same protocol used for the EAE immunization but excluding the PLP peptide. We followed these mice for 10 days after immunization. We could not detect weight loss (Figure **S4A**), disease symptoms (Figure **S4B**), changes in ventricle size (Figure **S4C**) or occurrence of cerebellar lesions in these animals during this time window.

Ventricle volume increase is related to changes in T_2 relaxation time of cerebrospinal fluid

To investigate possible changes in water content in the cerebrospinal fluid (CSF), we performed T_2 relaxometry, which correlates with methods of direct water content quantification in the brain [20,21]. As shown in a representative mouse within the group, a significant increase in T_2 relaxation time of the CSF also occurred at early stages of the disease and persisted until after disease onset (Figure **5A**). In order to compare the changes in ventricle volume and changes in T_2 relaxation time, we pooled the data acquired on three consecutive days prior to first clinical symptoms and data acquired during the three days after first clinical symptoms, and compared the changes to age-matched healthy control mice. These control animals were measured in parallel to the EAE mice. When compared to the ventricle size of control animals (volume = 12.7 ± 1.1 (± S.D.) mm^3), we observed a significant increase in ventricle size in EAE mice prior to clinical disease onset and an even more prominent increase following disease manifestation (Figure **5B**). Also when comparing the CSF T_2 relaxation times between EAE and control mice, we observed an increase in CSF T_2 relaxation time both prior to (controls = 106.4 ± 5.83 (± S.D.), EAE mice = 110.8 ± 4.18 (± S.D.), p = 0.0586) and

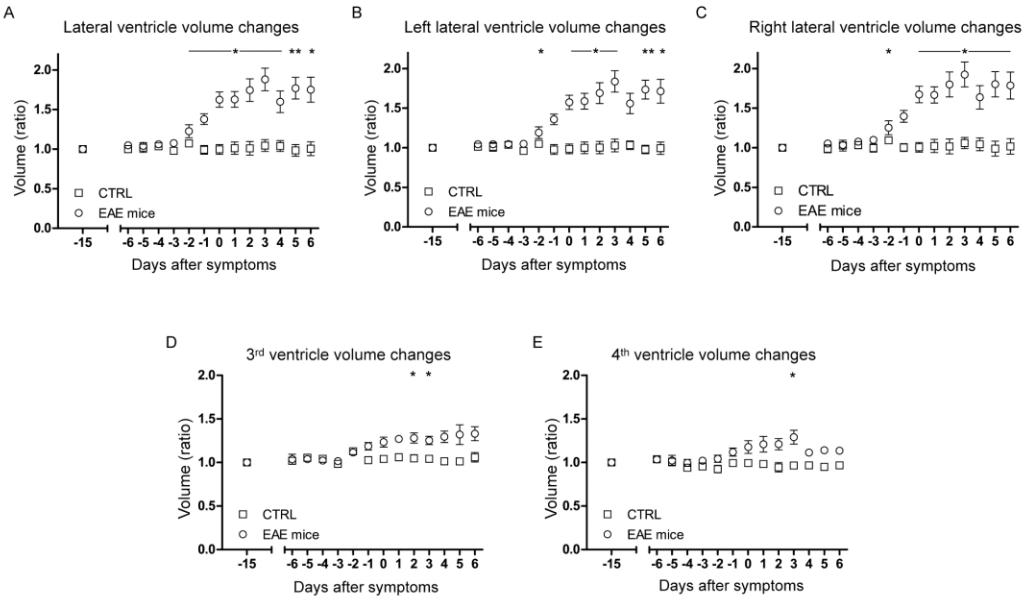

Figure 4. Changes in volume for the single ventricular compartments. Shown is a graphical representation of the temporal changes in volume for both lateral (A), left lateral (B), right lateral (C), third (D) and fourth (E) ventricles for all EAE (n=20) and control (n=6) mice. All points represent a ratio of the daily ventricle volume to the ventricle volume prior to immunization (baseline d-15) and are synchronized to the day of clinical disease onset.

doi: 10.1371/journal.pone.0072841.g004

following (controls = 107.3 ± 3.10 (± S.D.), EAE mice = 116 ± 4.29 (± S.D.), $p = 0.0004$) disease onset (Figure **5C**).

Discussion

Studying the early processes during CNS inflammation is important to gain a better insight into how immune cell invasion may affect the autoimmune response. In this study we identified an early ventricular enlargement prior to cerebral disease manifestation in a mouse model of encephalomyelitis.

In the animal model, the increase in ventricular size was accompanied by increased free water content in CSF as demonstrated by increased T_2 relaxation times in the CSF compartment. In some EAE mice we observed a contraction in ventricle size at the time between disease peak and prior to remission, indicating a possible reversibility in the factor contributing to enlargement of the ventricles. Likely as a consequence to ventricular enlargement, in the group of animals with sustained ventricular enlargement we observed a decrease in brain parenchyma volume. In contrast, this finding did not hold true in the ventricle normalizing animals. In the non-normalizing animals the brain volume reduction occurred after ventricle enlargement. Thus, we may exclude brain atrophy as primary source of ventricular enlargement in our study – a finding further supported by the very early time point ventricular enlargement is detectable. Prior to the macroscopic changes in the ventricles, we also detected microscopic alterations in the brain parenchyma. Microscopic changes involved evolving hyper- and hypo-intense regions in T_2-weighted images, particularly in the cerebellar white matter and as early as three days before symptom onset. The latter is in line with our first micro MRI study in EAE mice where we corroborated using immunohistology the presence of hypo-intense lesions in T_2-weighted images to areas of immune cell infiltration [19].

One possible explanation for the ventricular enlargement could be an impediment in cerebral CSF flow resulting from a physical obstruction at the interventricular foramen (Monro), such as in obstructive hydrocephalus. We therefore measured the changes in volume in all four ventricles to determine whether the ventricles downstream of the lateral ventricles also changed in size. The analysis of each separate ventricle revealed that each ventricular compartment increased in size prior to clinical symptom onset. Also a few days before disease manifestation, we detected an increase in CSF water content within the ventricles as reflected from the T_2 relaxation time. Several previous reports have demonstrated a linear correlation between spin-spin relaxation time (T_2) measurements and *ex vivo* desiccation methods to quantify tissue water content in brain [20,21] and other tissue [30]. As

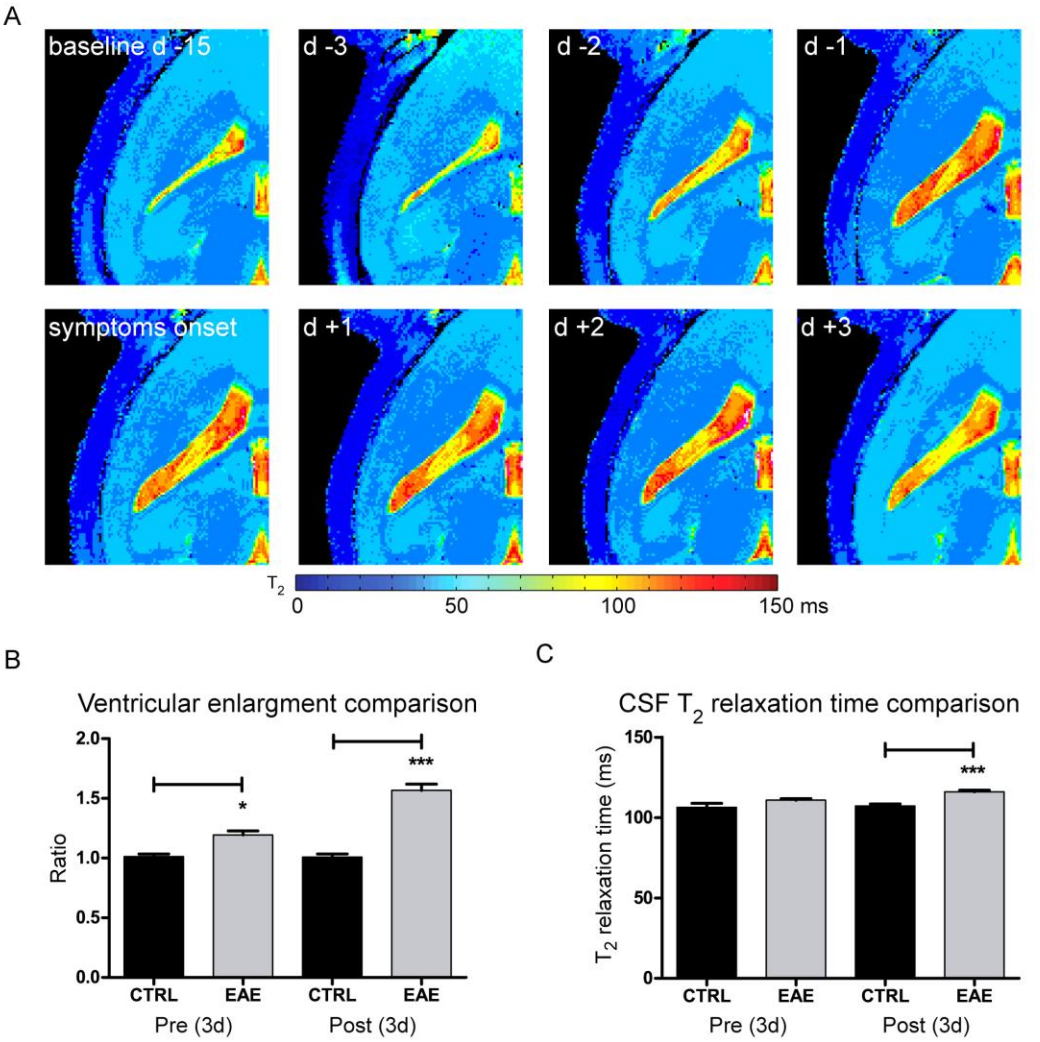

Figure 5. Pre- and post- symptomatic changes in ventricle size and cerebrospinal fluid T_2 relaxation time. (A) Maps depicting the absolute T_2 relaxation time (ms) prior to and after disease manifestation. (B) Values for the ventricle volume were grouped into two groups for all EAE animals (3 days before and 3 days after first symptom) and compared with control animals. Shown are the differences in ventricle volume between the control (CTRL) and EAE groups prior to (Pre (3d), $p = 0.0180$) and after (Post (3d), $p = 0.0003$) disease onset. (C) Values for the CSF T_2 relaxation time were also grouped as above and compared with control animals. Shown are the differences in T_2 relaxation times between the control (CTRL) and EAE groups prior to (Pre (3d), $p = 0.0386$) and after (Post (3d), $p = 0.0002$) disease manifestation.

doi: 10.1371/journal.pone.0072841.g005

reference, *in vitro* modifications in water content from 70% to 85% were reported to change T_2 relaxation time from 100 ms to 200 ms [20].

Our results appear to preclude the hypothesis that volume increase in the ventricles could be the result of an obstruction in one of the foramina connecting the ventricles. These results

rather suggest that the increase in ventricular size could be either the result of a dysregulation in CSF homeostasis (e.g. a deficit in CSF reabsorption or an increase in CSF production). Alternatively, a disruption of the tight junctions (TJ) of the BBB and blood CSF barrier may increase the flux of solutes through the barrier leading to fluid leakage into the CSF-filled compartments. In this perspective it has been shown that an alteration of BBB TJ proteins and changes in microcirculation, associated with the presence of inflammatory cells, occur during EAE and MS [13,31–33]. On the other hand, we recently reported a contrast agent-enriched ventricular system in EAE suggesting a leakage into the ventricles possibly via the blood CSF barrier during disease [19]. Using a flow compensated gradient echo technique, we observed an outflow of Gd-DTPA into the ventricles of EAE but not healthy animals [19]. Either of these possibilities suggests that ventricle size may serve as a potential indicator of the level of inflammation in the CNS, even prior to other more conventional measures (e.g. contrast enhancing lesions).

Several CNS routes exist for CSF drainage that might be involved in the communication with the lymphatic system. The relevance of immune cell trafficking between the lymphatic system and CNS has been described in models of spontaneous EAE [34]. Important communication routes include anatomical sites (such as the cribriform plate) associated with lymphatics (eg. those associated with the olfactory or other cranial nerves) [35]. Immune cells, including memory CD4+ T cells, follow these communication routes during autoimmune neuroinflammation [2]. More recently, it was also shown that leukocytes infiltrate periventricular tissue as well as perivascular spaces prior to clinical symptom onset [36]. In agreement with this study, we have also recently shown an extensive accumulation of inflammatory cells on the ventral side of the forebrain, midbrain and brainstem as shown by fluorine/proton MRI [37].

In all of our EAE cases, the fluctuations in ventricular volume were relatively fast and cannot be explained by brain atrophy that is a slow and gradual process occurring over several years [38]. Furthermore, in a recent study with MS patients that were followed up MRI for a period of 5 years after first diagnosis, the percentage ventricular volume change was found to be higher during the first 2 years compared to the ensuing 3 years [39]. The rate of early ventricular enlargement was also suggested in this study to be more predictive of disease progression than lesion measures or whole brain atrophy rate [39].

In summary, our present findings in the EAE model provide first indications that the progression of encephalomyelitis is accompanied by substantial fluctuations in ventricle size already in the earliest stages of disease. Several mechanisms could be involved in this observation, including a disruption in CSF homeostasis or fluctuations in the edematous milieu of inflammatory cells and their products. Further preclinical and clinical investigations are warranted to elucidate the basis leading to ventricular enlargement and to explore the mechanisms and causative factors that could precipitate these macroscopic changes during encephalomyelitis.

Supporting Information

Figure S1. Overview of the pre-symptomatic brain alterations.
(A) Shown are, for each animal, the first day of cerebellar lesion appearance ($p < 0.0001$) and the first day of ventricle enlargement ($p < 0.0001$) are shown, compared to the days of symptom onset (n= 20). (B) Time-to-event curves to compare the first occurrence of ventricle enlargement and cerebellar lesions relative to clinical onset. Statistical significance: cerebellar lesions vs. clinical signs, $p < 0.0001$; ventricular enlargement vs. clinical signs, $p = 0.0064$.
(TIF)

Figure S2. No relation between magnitude or occurrence of ventricle enlargement and clinical disease measures.
(A) Comparison between disease severity and magnitude of ventricular enlargement. (B) Comparison between weight loss and magnitude of ventricular enlargement. (C) Comparison between disease severity and occurrence of ventricular enlargement.
(TIF)

Figure S3. Time-line of changes in brain parenchyma volume during EAE development.
Brain parenchyma was measured in slices depicting the caudate putamen and lateral ventricles. The parenchymal volumes for all animals were centered on day of symptom onset. Temporal changes in the parenchymal volume of mice with sustained ventricle enlargement (A) and parenchymal volume of mice with normalizing ventricles (B) were compared to controls.
(TIF)

Figure S4. Timeline of weight and ventricle size and score of sham immunized animals.
All the animals were weighed and scored before sham immunization and daily thereafter. Micro MRI measurements were performed at baseline and then from day 5 to day 10 after sham immunization and the ventricle volumes measured. Temporal changes in weight (A), score (B) and ventricle volume (C) are shown (n=6).
(TIF)

Acknowledgements

We thank Antje Els for excellent technical support.

Author Contributions

Conceived and designed the experiments: SL HW TN SW. Performed the experiments: SL HW JS. Analyzed the data: SL HW JH YJ SW. Contributed reagents/materials/analysis tools: JH AP TN SW. Wrote the manuscript: SL HW JM JW FP TN SW.

References

1. Sallusto F, Impellizzieri D, Basso C, Laroni A, Uccelli A et al. (2012) T-cell trafficking in the central nervous system. Immunol Rev 248: 216-227. doi:10.1111/j.1600-065X.2012.01140.x. PubMed: 22725964.
2. Giunti D, Borsellino G, Benelli R, Marchese M, Capello E et al. (2003) Phenotypic and functional analysis of T cells homing into the CSF of subjects with inflammatory diseases of the CNS. J Leukoc Biol 73: 584-590. doi:10.1189/jlb.1202598. PubMed: 12714572.
3. Ruiz-Cabello J, Barnett BP, Bottomley PA, Bulte JW (2011) Fluorine (19F) MRS and MRI in biomedicine. NMR Biomed 24: 114-129. doi: 10.1002/nbm.1570. PubMed: 20842758.
4. Ousman SS, Kubes P (2012) Immune surveillance in the central nervous system. Nat Neurosci 15: 1096-1101. doi:10.1038/nn.3161. PubMed: 22837040.
5. Kivisäkk P, Mahad DJ, Callahan MK, Trebst C, Tucky B et al. (2003) Human cerebrospinal fluid central memory CD4+ T cells: evidence for trafficking through choroid plexus and meninges via P-selectin. Proc Natl Acad Sci U S A 100: 8389-8394. doi:10.1073/pnas.1433000100. PubMed: 12829791.
6. Wilson EH, Weninger W, Hunter CA (2010) Trafficking of immune cells in the central nervous system. J Clin Invest 120: 1368-1379. doi: 10.1172/JCI41911. PubMed: 20440079.
7. Greter M, Heppner FL, Lemos MP, Odermatt BM, Goebels N et al. (2005) Dendritic cells permit immune invasion of the CNS in an animal model of multiple sclerosis. Nat Med 11: 328-334. doi:10.1038/nm1197. PubMed: 15735653.
8. Kivisäkk P, Imitola J, Rasmussen S, Elyaman W, Zhu B et al. (2009) Localizing central nervous system immune surveillance: meningeal antigen-presenting cells activate T cells during experimental autoimmune encephalomyelitis. Ann Neurol 65: 457-469. doi:10.1002/ana.21379. PubMed: 18496841.
9. Kerfoot SM, Kubes P (2002) Overlapping roles of P-selectin and alpha 4 integrin to recruit leukocytes to the central nervous system in experimental autoimmune encephalomyelitis. J Immunol 169: 1000-1006. PubMed: 12097407.
10. Piccio L, Rossi B, Scarpini E, Laudanna C, Giagulli C et al. (2002) Molecular mechanisms involved in lymphocyte recruitment in inflamed brain microvessels: critical roles for P-selectin glycoprotein ligand-1 and heterotrimeric G(i)-linked receptors. J Immunol 168: 1940-1949. PubMed: 11823530.
11. Engelhardt B, Coisne C (2011) Fluids and barriers of the CNS establish immune privilege by confining immune surveillance to a two-walled castle moat surrounding the CNS castle. Fluids Barriers CNs 8: 4. doi: 10.1186/2045-8118-8-4. PubMed: 21349152.
12. Dawson JW (1916). XVIII—Histol Disseminated Sclerosis Transactions R Soc Edinb 50: 517-740. doi:10.1017/S0080456800027174.
13. Plumb J, McQuaid S, Mirakhur M, Kirk J (2002) Abnormal endothelial tight junctions in active lesions and normal-appearing white matter in multiple sclerosis. Brain Pathol 12: 154-169. PubMed: 11958369.
14. Achiron A, Faibel M (2002) Sandlike appearance of Virchow-Robin spaces in early multiple sclerosis: a novel neuroradiologic marker. AJNR Am J Neuroradiol 23: 376-380. PubMed: 11901003.
15. Wuerfel J, Haertle M, Waiczies H, Tysiak E, Bechmann I et al. (2008) Perivascular spaces--MRI marker of inflammatory activity in the brain? Brain 131: 2332-2340. doi:10.1093/brain/awn171. PubMed: 18676439.
16. Nouls JC, Izenson MG, Greeley HP, Johnson GA (2008) Design of a superconducting volume coil for magnetic resonance microscopy of the mouse brain. J Magn Reson 191: 231-238. doi:10.1016/j.jmr.2007.12.018. PubMed: 18221901.
17. Baltes C, Radzwill N, Bosshard S, Marek D, Rudin M (2009) Micro MRI of the mouse brain using a novel 400 MHz cryogenic quadrature RF probe. NMR Biomed 22: 834-842. doi:10.1002/nbm.1396. PubMed: 19536757.
18. Wagenhaus B, Pohlmann A, Dieringer MA, Els A, Waiczies H et al. (2012) Functional and morphological cardiac magnetic resonance imaging of mice using a cryogenic quadrature radiofrequency coil. PLOS ONE 7: e42383. doi:10.1371/journal.pone.0042383. PubMed: 22870323.
19. Waiczies H, Millward JM, Lepore S, Infante-Duarte C, Pohlmann A et al. (2012) Identification of Cellular Infiltrates during Early Stages of Brain Inflammation with Magnetic Resonance Microscopy. PLOS ONE 7: e32796. doi:10.1371/journal.pone.0032796. PubMed: 22427887.
20. Kamman RL, Go KG, Brouwer W, Berendsen HJ (1988) Nuclear magnetic resonance relaxation in experimental brain edema: effects of water concentration, protein concentration, and temperature. Magn Reson Med 6: 265-274. doi:10.1002/mrm.1910060304. PubMed: 3362061.
21. Qiao M, Malisza KL, Del Bigio MR, Tuor UI (2001) Correlation of cerebral hypoxic-ischemic T2 changes with tissue alterations in water content and protein extravasation. Stroke 32: 958-963
22. Aktas O, Waiczies S, Smorodchenko A, Dorr J, Seeger B et al. (2003) Treatment of relapsing paralysis in experimental encephalomyelitis by targeting Th1 cells through atorvastatin. J Exp Med 197: 725-733. doi: 10.1084/jem.20021425. PubMed: 12629065.
23. Smith SM, Jenkinson M, Woolrich MW, Beckmann CF, Behrens TE et al. (2004) Advances in functional and structural MR image analysis and implementation as FSL. NeuroImage 23 Suppl 1: S208-S219. doi: 10.1016/j.neuroimage.2004.07.051. PubMed: 15501092.
24. Woolrich MW, Jbabdi S, Patenaude B, Chappell M, Makni S et al. (2009) Bayesian analysis of neuroimaging data in FSL. Neuroimage 45: S173-S186. doi:10.1016/j.neuroimage.2008.10.055. PubMed: 19059349.
25. Jenkinson M, Beckmann CF, Behrens TE, Woolrich MW, Smith SM (2012) Fsl. NeuroImage 62: 782-790. doi:10.1016/j.neuroimage.2011.09.015. PubMed: 21979382.
26. Jenkinson M, Pechaud M, Smith S (2005) BET2: MR-based estimation of brain, skull and scalp surfaces. Eleventh Annual Meeting of the Organization for Human Brain Mapping.
27. Zhang Y, Brady M, Smith S (2001) Segmentation of brain MR images through a hidden Markov random field model and the expectation-maximization algorithm. IEEE Trans Med Imaging 20: 45-57. doi: 10.1109/42.906424. PubMed: 11293691.
28. Jenkinson M, Bannister P, Brady M, Smith S (2002) Improved optimization for the robust and accurate linear registration and motion correction of brain images. NeuroImage 17: 825-841. doi:10.1006/nimg.2002.1132. PubMed: 12377157.
29. Rivest S (2003) Molecular insights on the cerebral innate immune system. Brain Behav Immun 17: 13-19. doi:10.1016/S0889-1591(02)00055-7. PubMed: 12615045.
30. Lüsse S, Claassen H, Gehrke T, Hassenpflug J, Schünke M et al. (2000) Evaluation of water content by spatially resolved transverse relaxation times of human articular cartilage. Magn Reson Imaging 18: 423-430. doi:10.1016/S0730-725X(99)00144-7. PubMed: 10788720.
31. Wolburg H, Wolburg-Buchholz K, Kraus J, Rascher-Eggstein G, Liebner S et al. (2003) Localization of claudin-3 in tight junctions of the blood-brain barrier is selectively lost during experimental autoimmune encephalomyelitis and human glioblastoma multiforme. Acta Neuropathol 105: 586-592. PubMed: 12734665.
32. Morgan L, Shah B, Rivers LE, Barden L, Groom AJ et al. (2007) Inflammation and dephosphorylation of the tight junction protein occludin in an experimental model of multiple sclerosis. Neuroscience 147: 664-673. doi:10.1016/j.neuroscience.2007.04.051. PubMed: 17560040.
33. Wuerfel J, Paul F, Zipp F (2007) Cerebral blood perfusion changes in multiple sclerosis. J Neurol Sci 259: 16-20. doi:10.1016/j.jns.2007.02.011. PubMed: 17382348.
34. Furtado GC, Marcondes MC, Latkowski JA, Tsai J, Wensky A et al. (2008) Swift entry of myelin-specific T lymphocytes into the central nervous system in spontaneous autoimmune encephalomyelitis. J Immunol 181: 4648-4655. PubMed: 18802067.
35. Ransohoff RM, Kivisäkk P, Kidd G (2003) Three or more routes for leukocyte migration into the central nervous system. Nat Rev Immunol 3: 569-581. doi:10.1038/nri1130. PubMed: 12876559.
36. Schmitt C, Strazielle N, Ghersi-Egea JF (2012) Brain leukocyte infiltration initiated by peripheral inflammation or experimental autoimmune encephalomyelitis occurs through pathways connected to the CSF-filled compartments of the forebrain and midbrain. J Neuroinflammation 9: 187. doi:10.1186/1742-2094-9-187. PubMed: 22870891.
37. Waiczies H, Lepore S, Drechsler S, Qadri F, Purfurst B et al. (2013) Visualizing brain inflammation with a shingled-leg radio-frequency head probe for 19F/1H MRI. Sci Rep. p. 3: 1280
38. Miller DH, Barkhof F, Frank JA, Parker GJ, Thompson AJ (2002) Measurement of atrophy in multiple sclerosis: pathological basis, methodological aspects and clinical relevance. Brain 125: 1676-1695. doi:10.1093/brain/awf177. PubMed: 12135961.
39. Lukas C, Minneboo A, de Groot V, Moraal B, Knol DL et al. (2010) Early central atrophy rate predicts 5 year clinical outcome in multiple sclerosis. J Neurol Neurosurg, Psychiatry 81: 1351-1356. doi:10.1136/jnnp.2009.199968. PubMed: 20826873.

SCIENTIFIC REPORTS

OPEN

SUBJECT AREAS:
BIOMEDICAL ENGINEERING
NEUROIMMUNOLOGY
BIOMARKER RESEARCH
ELECTRICAL AND ELECTRONIC ENGINEERING

Received
4 December 2012

Accepted
29 January 2013

Published
15 February 2013

Correspondence and requests for materials should be addressed to H.W. (helmar.waiczies@mdc-berlin.de)

Visualizing Brain Inflammation with a Shingled-Leg Radio-Frequency Head Probe for $^{19}F/^{1}H$ MRI

Helmar Waiczies[1,2], Stefano Lepore[1,2], Susanne Drechsler[1,2], Fatimunnisa Qadri[2,3], Bettina Purfürst[4], Karl Sydow[5], Margitta Dathe[5], André Kühne[6], Tomasz Lindel[6], Werner Hoffmann[6], Andreas Pohlmann[1], Thoralf Niendorf[1,2] & Sonia Waiczies[1,2]

[1]Berlin Ultrahigh Field Facility (B.U.F.F.), Max Delbrück Center for Molecular Medicine, [2]Experimental and Clinical Research Center, a joint cooperation between the Charité Medical Faculty and the Max Delbrück Center for Molecular Medicine, [3]Molecular Biology of Peptide Hormones, Max Delbrück Center for Molecular Medicine, [4]Electron Microscopy Core Facility, Max Delbrück Center for Molecular Medicine, [5]Peptide Lipid Interaction/Peptide Transport, Leibniz-Institut für Molekulare Pharmakologie (FMP), [6]Department of Medical Physics and Metrological Information Technology, Physikalisch Technische Bundesanstalt (PTB).

Magnetic resonance imaging (MRI) provides the opportunity of tracking cells *in vivo*. Major challenges in dissecting cells from the recipient tissue and signal sensitivity constraints albeit exist. In this study, we aimed to tackle these limitations in order to study inflammation in autoimmune encephalomyelitis. We constructed a very small dual-tunable radio frequency (RF) birdcage probe tailored for ^{19}F (fluorine) and ^{1}H (proton) MR mouse neuroimaging. The novel design eliminated the need for extra electrical components on the probe structure and afforded a uniform B_1^+-field as well as good SNR. We employed fluorescently-tagged ^{19}F nanoparticles and could study the dynamics of inflammatory cells between CNS and lymphatic system during development of encephalomyelitis, even within regions of the brain that are otherwise not easily visualized by conventional probes. $^{19}F/^{1}H$ MR Neuroimaging will allow us to study the nature of immune cell infiltration during brain inflammation over an extensive period of time.

Inflammation is a key player in several disorders of the central nervous system (CNS). In autoimmune encephalomyelitis a recruitment of immune cells to the CNS occurs early during the pathogenesis, prior to the onset of neurological symptoms[1–3]. The tracking of immune cells into the brain and spinal cord is thus pivotal for understanding the development of CNS inflammation in preclinical animal models such as experimental autoimmune encephalomyelitis (EAE). Strategies for following cells in the CNS during EAE have commonly made use of iron oxide nanoparticles that reduce T2* relaxation[4–7]. One drawback of these contrast agents is the difficulty to distinguish the negative contrast created by the labeled cells from other intrinsic tissue contrasts. This, together with the lack of an *a priori* knowledge of the kinetics of immune cell migration during inflammation, makes the localization of immune cells in the CNS a challenging task. The use of fluorine (^{19}F)-rich nanoparticles to track inflammatory cells, in conjunction with $^{19}F/^{1}H$ MRI, is an emerging approach for cell tracking[8]. Due to the absence of organic ^{19}F *in vivo*, $^{19}F/^{1}H$ MRI is advantageous for localizing transplanted cells *in vivo* since it permits background-free images with complete signal selectivity and specificity. The possibility of quantifying the cell signal by ^{19}F MR spectroscopy is another advantage.

One major limitation when tracking immune cells in the CNS with $^{19}F/^{1}H$ MRI is the low signal-to-noise ratio (SNR) for both ^{19}F and ^{1}H signals. The SNR and the sensitivity of the radio frequency (RF) probe used are indeed main determinants that dictate the level of spatial resolution[9]. Factors to be kept in mind when designing a probe include the geometry, the filling factor and the homogeneity of the B_1^+-transmit field. Small-sized birdcage probes are ideal for mouse neuroimaging but are quite challenging to build due to size and increased risk of inaccurate assembly of chip capacitors that could distort the circuit symmetry and RF homogeneity. The millipede design was developed to eliminate the necessity of chip capacitors[10]. However millipede probes are too complex to be modified as double-tunable probes; an assembly of two spiral coils would need to be constructed to achieve a double resonant setup[10] but this results in an undesirable sensitivity difference between outer and inner coils. In order to track inflammatory cells *in vivo* with $^{19}F/^{1}H$ MRI, a dual-tunable RF probe is desirable in order to

safeguard sensitivity and B_1-field homogeneity on both frequencies and to avoid inaccurate co-registration of both signals[11].

In this study we constructed a novel dual-tunable $^{19}F/^{1}H$ birdcage probe with a shingled-leg design in order to detect immune cell infiltration in the mouse brain during encephalomyelitis. Thirty two copper strips were arranged in parallel to form a cylinder and overlapped with strips extending from the end rings of the RF probe. This provided plate capacitance on each leg, thereby eliminating the necessity of solid chip capacitors. With our RF probe we were able to detect inflammatory cell infiltrates as ^{19}F signal in EAE mice following *in vivo* administration of fluorescently-labeled ^{19}F-rich particles. We observed immune cell penetration even in regions of the CNS e.g. anterior region of brainstem and spinal cord that are otherwise not easily visualized by conventional RF probes due to limited depth penetration.

Results

Electromagnetic field simulations and performance of the RF head. We first performed simulations with a finite integration technique (MWS) using a shield diameter of 58 mm and determined that we require a capacitance of 1.14 pF in order to tune to 400 MHz (^{1}H frequency at 9.4 Tesla). These results were in close agreement with those calculated using an analytical method (Birdcage Builder), in which we determined a required capacitance of 1.17 pF (<3% deviation). Since the calculated capacitor values were small (**Figure 1**) and considering the need for accuracy, especially in the increments between the capacitors, we decided to circumvent conventional chip capacitors during construction of the birdcage. Instead we introduced a shingled birdcage design, in which capacitors were built, with high accuracy, into the structure of the RF probe. For this the copper milling on either side of the PCB was done

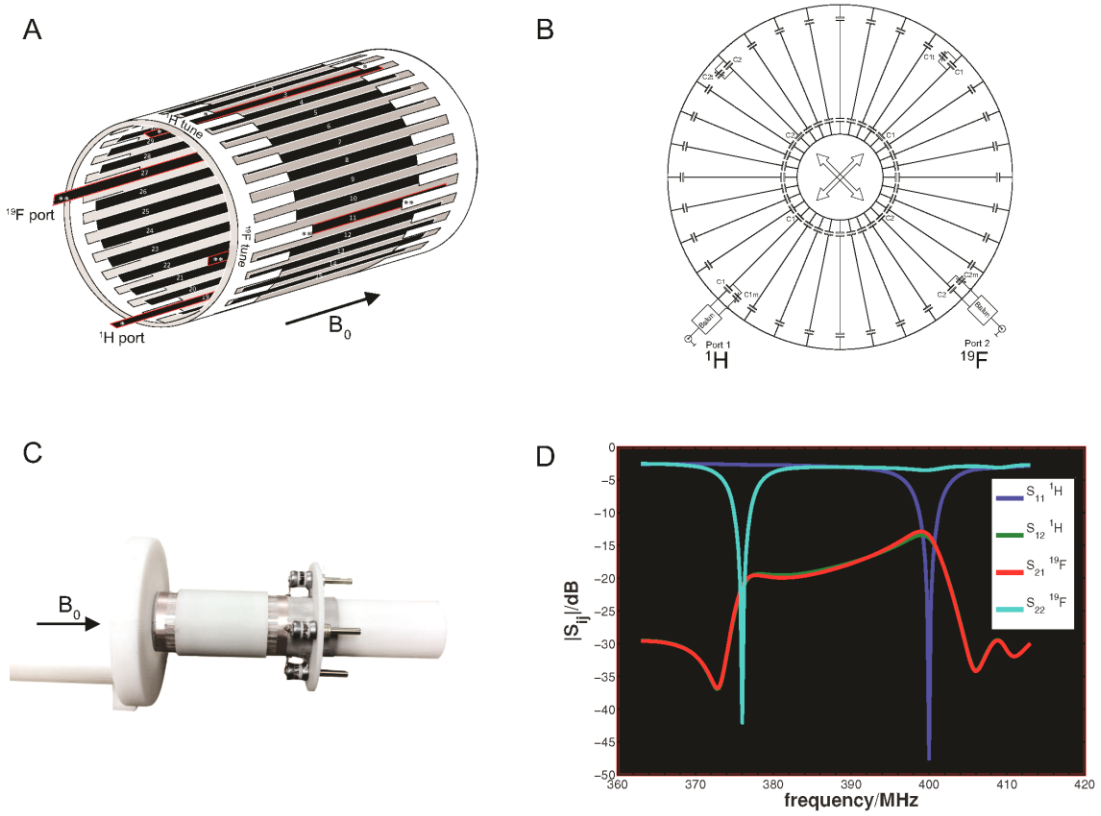

Figure 1 | Design and Construction of the $^{19}F/^{1}H$ RF Birdcage Mouse Head Probe. (A) Sketch of the 32 leg low-pass birdcage probe shows the main setup consisting of long copper strip-lines (shown in black) that overlap with the peripheral copper strip-lines (shown in white) connected together by the end rings. Out of 32 legs, 28 copper-strips were uniformly overlapped by an area of 6.27 mm^2 to achieve a center frequency of 388 MHz, 2 strip-lines (marked with *) overlapped by a smaller area (3.14 mm^2) to tune for ^{1}H at 400 MHz (for 9.4 Tesla) and 2 strip-lines (marked with **) overlapped by an area of 9.39 mm^2 to tune for ^{19}F at 376 MHz (for 9.4 Tesla). The probe axis is aligned with the direction of the static magnetic field B_o. (B) Circuit diagram of the birdcage probe showing the 56 capacitors (C_{legs} = 1.38 pF, resulting from the above uniformly overlapped 28 legs) that adjust the birdcage to the center frequency (388.35 MHz), C1 (0.69 pF) capacitors (created by the 2 legs with 3.14 mm^2 overlap) that tune one port to ^{1}H mode and C2 (2.08 pF) capacitors (created by the 2 legs with 9.39 mm^2 overlap) that tune the other port to ^{19}F mode. C1m/C2m are the matching capacitors and C1t/C2t the tuning capacitors in the range of 1–6 pF. (C) Photograph of the constructed birdcage (without shield) in correct alignment with the direction of the static magnetic field B_o. Arrow also indicates the access point and direction of the prone-positioned mouse for head imaging. (D) Examination of RF performance with respect to the scattering (*S*) parameters shows that port 1 (^{1}H) resonates at 400 MHz and Port 2 (^{19}F) at 376 MHz. The reflection coefficients on both ports (S_{11} and S_{22}) are shown to be lower than −40 dB and the coupling between the ports (S_{12} and S_{21}) is shown to be lower than -15 dB.

in a way to create an overlap between the inner and outer copper strips, thereby creating plate capacitors along the length of the birdcage legs (**Figure 1A–1C**). To fine tune to the exact ^{1}H (400 MHz) and ^{19}F (376 MHz) frequencies required at 9.4 Tesla, the shield diameter was reduced from 58 mm (used for the first simulations) to 48 mm. This shield diameter was used for the construction of the coil design as well as for the final EMF simulations. Based on the required capacitance results calculated from MWS and the Birdcage Builder, an overlap of 6.27 mm^2 (equivalent to 1.38 pF) was used for the simulation (**Figure 2A–2D**) and ultimate construction (**Figure 1C**) in order for the birdcage to resonate at a main frequency of 388 MHz that is approximately half way between ^{1}H and ^{19}F when calculating the square root of the product of both frequencies ($\sqrt{400 * 376} = 387.81$ MHz).

Upon evaluation of the B_1^+ profiles in the EMF simulations for this setup (**Figure 2A**), we observed high B_1^+ homogeneity throughout the whole birdcage probe for both ^{1}H and ^{19}F modes (**Figure 2B and Supplementary Figure 1**). However, EMF simulations (particularly B_1^+ distribution) are only an estimation for a given setup, which does not take power losses into consideration. We therefore compared the B_1^+ field values achieved from the EMF simulation with real B_1^+ field values measured with the constructed birdcage probe in a 9.4 Tesla animal scanner for the ^{1}H channel (**Figure 2C**). For both simulation and measurement experiments, the same input power and absorbed tissue power in the phantom were employed (ignoring powers losses in cables, plugs and baluns). We calculated a maximum B_1^+ profile of 40 $\mu T/\sqrt{W}$ for the simulations and 31 $\mu T/\sqrt{W}$ for the measurement at the center of the slice (**Figure 2C, 2D**). The B_1^+ profile over the cross-section of the cylindrical phantom ranged from 38–40 $\mu T/\sqrt{W}$ for the measurement and 29–31 $\mu T/\sqrt{W}$ for the simulation (**Figure 2D**). The factor of 1.66 between B_1^+ simulations and B_1^+ measurements translates to a power attenuation of about 2.2 dB. This power attenuation is in agreement with losses in the RF chain (from amplifier to probe) that we could estimate from the properties of the cable and using the network analyzer.

Owing to the shingled design of the birdcage with variable overlaps between the copper strips, the RF probe could be tuned to both ^{1}H and ^{19}F frequencies. With this setup, the reflection coefficients (S_{11} and S_{22}) were below −40 dB for both frequencies (**Figure 1D**). The transmission coefficients (S_{12} and S_{21}) determine the extent of power lost via transmission between the 2 ports and was below −15 dB thereby not necessitating additional decoupling capacitors. Using the reflection coefficients we could measure the RF probe/coil quality as QFactor. This determines the extent of noise contribution coming from the RF probe or sample. We thus measured the QFactor of both loaded (Q_L) and unloaded (Q_U) RF probe using the formula "$Q = f_r/BW$" where f_r is the specific resonance frequency (400 MHz for ^{1}H) and BW is the corresponding bandwidth frequency at half maximum peak. We calculated Q_U to be 130. Q_L was calculated to be 80–110, depending on the load of the probe, the size of the mouse or conductivity of the phantom). For 376 MHz (^{19}F), Q-values were similar ($Q_U \approx 150$).

^{19}F/^{1}H MR tracking of cell infiltrates in experimental autoimmune encephalomyelitis (EAE). We performed ^{19}F/^{1}H MR imaging and spectroscopy of EAE mouse brains using the constructed head birdcage ^{19}F/^{1}H RF probe. For the first set of experiments (**Figure 3**) we induced EAE in SJL/J mice and administered ^{19}F-rich nanoparticles (Z-Average Diam. = 160 nm) intravenously in these mice only upon the first signs of neurological symptoms. Using the constructed ^{19}F/^{1}H RF probe and a 2D T_2-weighted gradient echo (FLASH) sequence for ^{1}H MRI, we observed hypointense lesions as previously reported[12] in the cerebellum (**Figure 3A, 3C**) and cerebral cortex (**Figure 3D, 3F**) of sick mice. In these experiments we decided

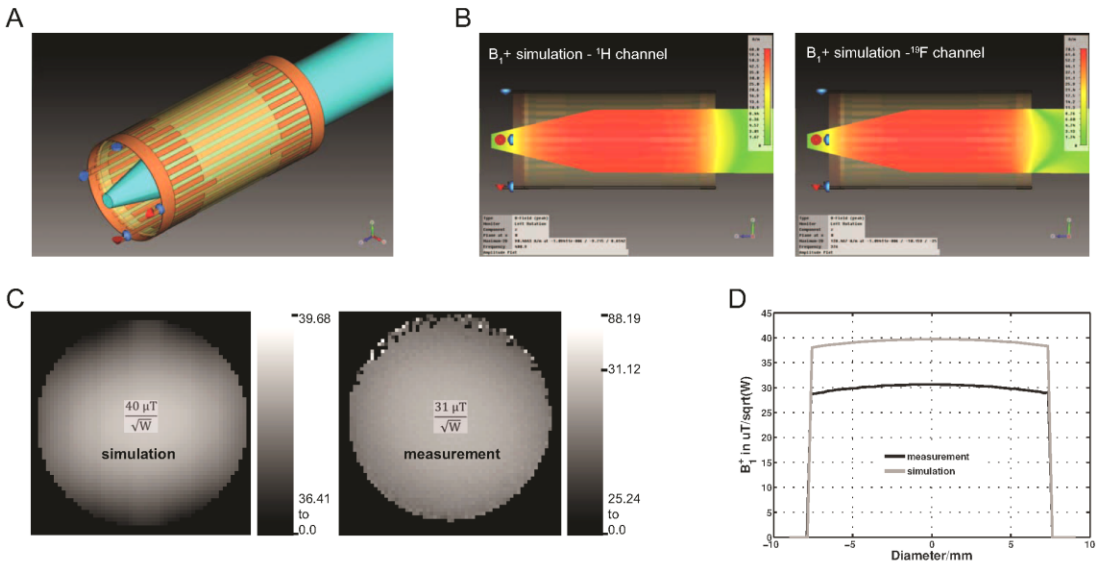

Figure 2 | B_1^+-Field Distribution for the ^{19}F/^{1}H RF Birdcage Probe. (A) Three dimensional design of the ^{19}F/^{1}H RF birdcage probe holding a phantom (turquoise) simulated with a finite integration technique (CST Studio Suite). For the measurements a phantom with similar dielectric properties and geometry was used. (B) Sagittal cross-section through the simulated B_1^+-field within the phantom. (C) Comparison of B_1^+-field measurement of the ^{1}H channel with the simulation of a central slice, scaled to the same input power and absorbed tissue-power in the object, not considering cable losses, plugs and baluns. (D) Shows a line-plot through the center of the simulated and measured B_1^+-field, with a maximum of 40 $\mu T/\sqrt{W}$ in the simulation and 31 $\mu T/\sqrt{W}$ for the measurement at the center. B_1^+-profile over the center slice ranges from 38–40 $\mu T/\sqrt{W}$ in the simulation and 29–31 $\mu T/\sqrt{W}$ in the measurement.

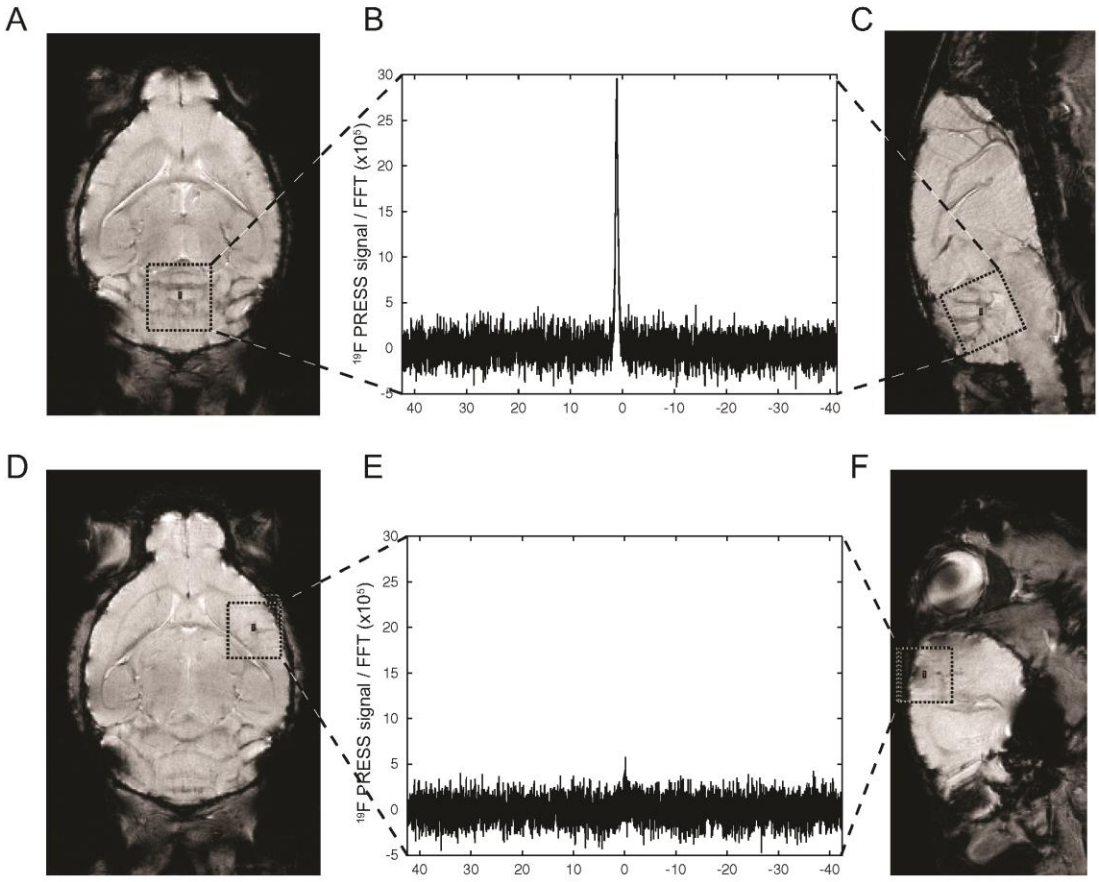

Figure 3 | In Vivo ^{19}F Quantification in an EAE mouse Brain using Single Voxel ^{19}F Spectroscopy. EAE was induced in SJL/J mice and 160 nm ^{19}F-rich nanoparticles (40 μmoles ^{19}F) were administered on the first signs of neurological symptoms. (A) Horizontal and (C) sagittal slices identifying lesions in the cerebellum; dotted box depicts the location of the 3 mm^3 PRESS voxel around the lesion of interest within the cerebellum. (B) ^{19}F MRS spectrum of the PRESS voxel in the cerebellum. (D) Horizontal and (F) sagittal slices identifying lesions in the cortex; dotted box depicts the location of the 3 mm^3 PRESS voxel around the hypointense lesion within the cortex. (E) ^{19}F MRS spectrum of the PRESS voxel in the cortex.

to administer one single shot of ^{19}F-rich nanoparticles with high ^{19}F content (corresponding to 40 μmoles) at the start of disease. Following 24 hours of nanoparticle application, we performed ^{19}F PRESS to determine the ^{19}F signal in the regions where we could detect hypointense lesions. For this, we localized a 3 mm^3 PRESS voxel around the cerebellum (**Figure 3A, 3C**) and another PRESS voxel around the hypointense lesion within the cortex (**Figure 3D, 3F**). In contrast to the selected region within the cortex (**Figure 3E**), we could detect a strong ^{19}F signal in the PRESS voxel in the cerebellum (**Figure 3B**), where we also observed larger areas of anatomical alterations using the ^{1}H gradient echo sequence (**Figure 3A**). With the help of a calibration measurement we calculated the ^{19}F content within the cerebellum to be c. 60 nmoles.

Next, we wanted to determine the location of the ^{19}F signal distributed within the cerebellum using ^{19}F/^{1}H MRI. To do so, we selected a 3 mm sagittal slice through the brain (**Figure 4A**), which encloses the 3 mm^3 PRESS voxel, and acquired ^{19}F gradient echo (FLASH) images. When we overlaid the T_2-weighted ^{1}H image (in-plane spatial resolution (73 × 73) μm^2) of the median sagittal slice (**Figure 4B**) with the ^{19}F image (**Figure 4C**) of the same sagittal section we observed co-localization of the ^{19}F signal to the brain stem and mostly the cerebellum, particularly in the white matter (**Figure 4D**). Following these ^{19}F/^{1}H MRI measurements we extracted the brain and prepared the cerebellum for electron microscopy. Already with the help of Differential Interference Contrast microscopy, we observed small, round and white particles engulfed within macrophage-like cells that were infiltrating the cerebellar lesions (**Figure 4E**). Electron microscopy revealed these particles as bright smooth spheroids clustered within phagosomes in the cytoplasm of macrophage-like cells (**Fig 4F–4H**).

Considering the highly homogeneous field provided by our MR head probe, we decided to implement accelerated spin echo techniques that are otherwise very sensitive to fluctuations in the B_1^+ field[13,14]. Apart from altering the scanning method, we also changed the protocol of systemic ^{19}F nanoparticle administration. We injected nanoparticles (same particle size but 5 μmoles ^{19}F content) daily, starting from day 5 following immunization. The first MRI measurements were performed on the first day of symptoms. First we acquired an *in vivo* ^{1}H 3D TurboRARE sequence using a standard protocol (TR = 1500 ms, TE = 53 ms, FOV = (40 × 16 × 16) mm^3, Matrix = 320 × 128 × 128, RARE Factor = 16, NEX = 1 (scan time = 25 min) to achieve a T_2-weighted image with an isotropic resolu-

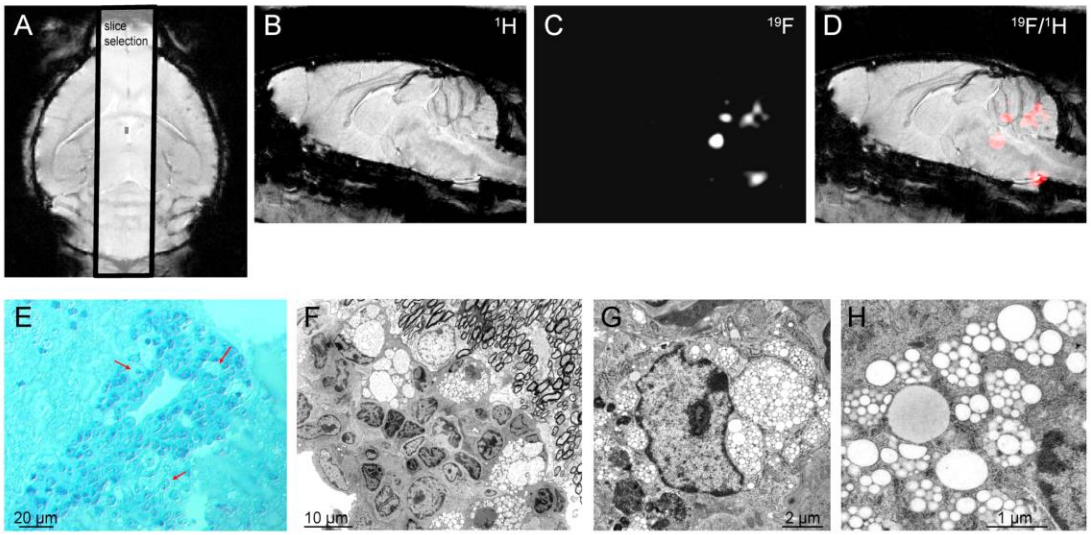

Figure 4 | ^{19}F/^{1}H MRI and Electron Microscopy of the ^{19}F-rich Particles within the Cerebellum of an EAE Mouse Brain. (A) Horizontal slice of the previous SJL/J mouse-brain using 2D-FLASH imaging: TR = 473 ms, TE = 13 ms, 22 slices, in-plane resolution 73 µm^2, NEX = 16 (scan time = 25 min). The black outlined box depicts the slice selection for the ^{19}F acquisition. (B) Median sagittal slice of the same mouse brain. (C) ^{19}F image of the 3 mm central slice using 2D FLASH TR = 15 ms, TE = 3.3 ms, 1 3 mm slice, in-plane resolution (400 × 400) µm^2, NEX = 2048 (scan time = 15 min) and (D) an overlay of (C) (in gray) and (D) (in red). (E) to (H) Histological slices of the extracted cerebellum. (E) Differential interference contrast image of a cerebellar lesion (toluidine blue staining) which shows small round and white nanoparticles engulfed into macrophage like cell structures (red arrows). (F) to (H) high resolution electron microscopy images of adjacent regions.

tion of 125 µm^3. Following this, we performed a ^{19}F MR TurboRARE sequence in the same mouse after it had undergone terminal anesthesia. For this, we employed the following ^{19}F MR protocol: TR = 1000 ms, TE = 6 ms, scan time = 690 min, FOV = (40 × 16 × 16) mm^3, Matrix = 100 × 40 × 40, zero fill acceleration = 2, RARE Factor = 40, NEX = 2048, leading to a reconstructed isotropic resolution of 400 µm^3. When we overlaid the acquired ^{19}F scans with the previous ^{1}H images, we observed that areas of inflammatory cell involvement were mostly within the spinal cord, brain stem, cerebellum and cerebral cortex (also in close proximity to the ventricles) as shown in horizontal (**Figure 5A**) and sagittal (**Figure 5B**) serial images of the brain. We also detected a strong ^{19}F signal within the cervical draining lymph nodes, areas of expected high inflammatory cell activity. These scans were the first to reveal the uptake of ^{19}F nanoparticles by immune cells and their extensive infiltration of these cells throughout the CNS and secondary lymphatic organs as shown by ^{19}F MRI.

In order to follow the dynamics of inflammatory cells during EAE *in vivo*, we altered the above ^{19}F MR protocol to reduce the acquisition time to 68 min. Following acquisition of the above ^{1}H 3D TurboRARE sequence, we performed an *in vivo* ^{19}F MRI using the following protocol: TR = 800 ms, TE = 6 ms, FOV = (40 × 16 × 16) mm^3, Matrix = 100 × 40 × 40, zero fill acceleration 2, RARE Factor = 40, NEX = 256. Similarly to the longer ^{19}F scans in the previous *ex vivo* experiments, the ^{19}F signals that we detected *in vivo* were mostly located within draining lymph nodes, the spinal cord, brain stem, cerebellum and cerebral cortex (**Figure 6A**). Typically, the draining lymph nodes were the first to give a ^{19}F signal (between day 5 and day 8); the ^{19}F signal extended from the submandibular and superficial cervical lymph nodes into the deeper cervical, facial and internal jugular lymph nodes. Between day 8 and day 11 we observed immune cell infiltration in the CNS.

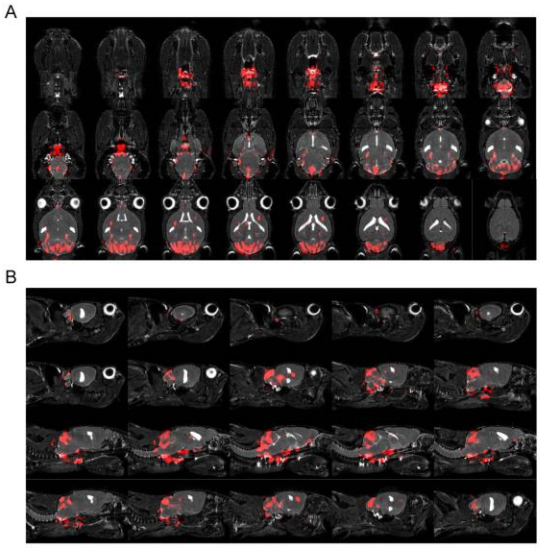

Figure 5 | In Vivo ^{1}H (grey) and Post Mortem ^{19}F MR(red) Images. EAE was induced in SJL/J mice and 160 nm ^{19}F-rich nanoparticles (5 µmoles ^{19}F) were administered daily, starting from day 5 following immunization.(A) Horizontal and (B) sagittal slices of a 3D TurboRARE-scan for *in vivo* ^{1}H (grayscale): TR = 1500 ms, TE = 53 ms, FOV = (40 × 16 × 16) mm^3, Matrix = 320 × 128 × 128, RARE Factor = 16, NEX = 1 (scan time = 25 min) and for *ex vivo* ^{19}F (red): TR = 1000 ms, TE = 6 ms, FOV = (40 × 16 × 16) mm^3, Matrix = 100 × 40 × 40, zero fill acceleration 2, RARE Factor = 40, NEX = 2048 (scan time = 690 min).

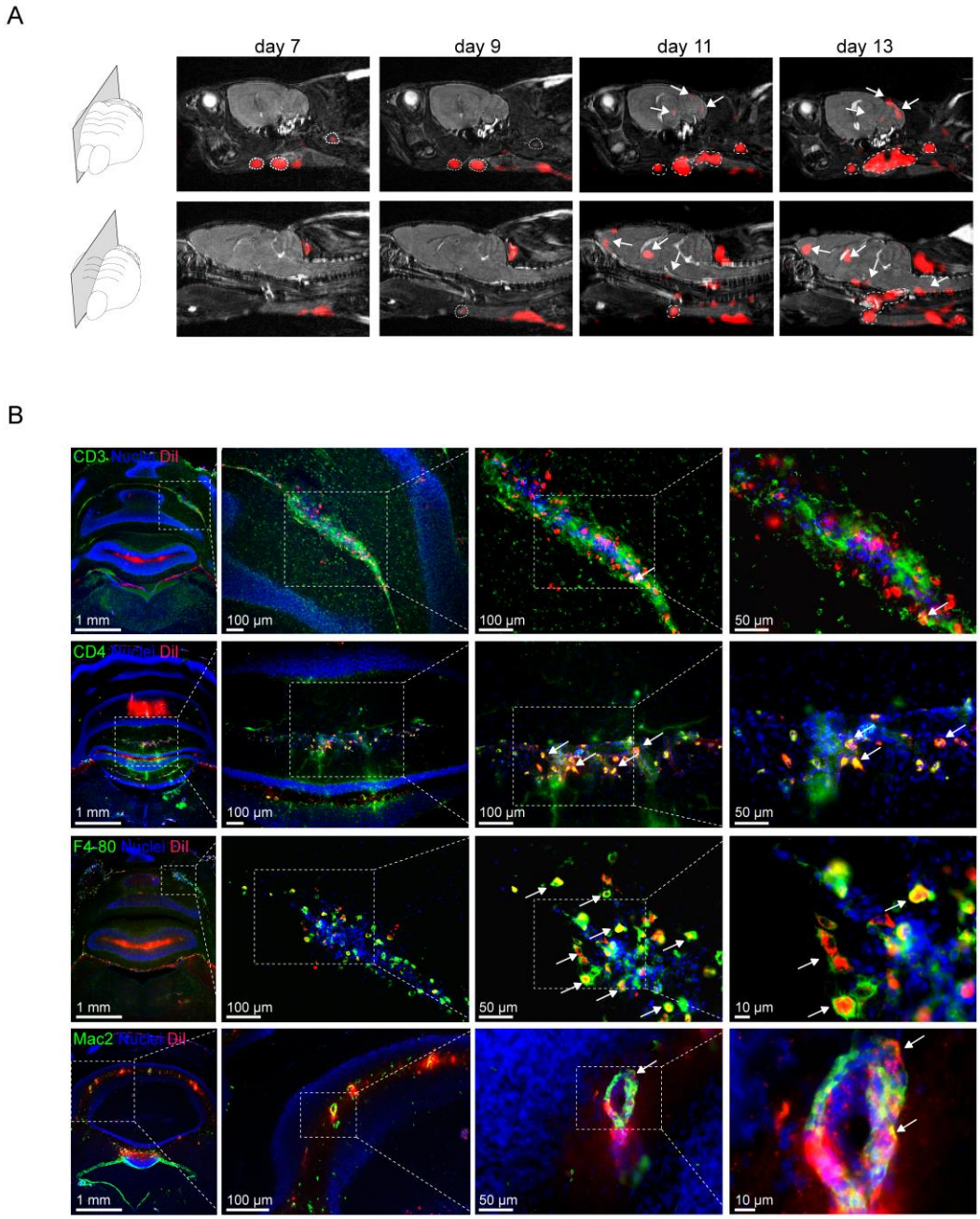

Figure 6 | Visualization of Inflammatory Cells in different CNS and Lymphatic Regions using In Vivo ^{19}F/ ^{1}H MRI. EAE was induced in SJL/J mice and 170 nm ^{19}F-rich and DiI-labeled nanoparticles (5 µmoles ^{19}F) were administered daily, starting from day 5 following immunization. (A) Two different sagittal slices of a 3D Turbo RARE-scan show the kinetics of inflammatory cell migration (^{19}F MRI) over a period of 6 days in different CNS and lymphatic regions (^{1}H MRI). *In vivo* ^{1}H sequence (as above) and ^{19}F MRI sequence: TR = 800 ms, TE = 6 ms, FOV = (40 × 16 × 16) mm^3, Matrix = 100 × 40 × 40, zero fill acceleration 2, RARE Factor = 40, NEX = 256 (scan time = 68 min). (B) Distribution of inflammatory cells (specifically CD3$^+$, CD4$^+$, F4-80$^+$ and Mac-2$^+$cells) in EAE tissue that gave a strong ^{19}F signal in MRI. Shown in coronal sections of the cerebellum are specific cell populations (green) and their corresponding uptake of ^{19}F-DiI nanoparticles (red). Arrows indicate colocalization (yellow) of signal from specific immune cell markers (green) and ^{19}F-DiI nanoparticles (red).

We next wanted to study the distribution of distinct immune cell populations in these areas of inflammation. Thus, we fluorescently tagged the ^{19}F nanoparticles for follow up in post fixation experiments and employed the same *in vivo* $^{19}F/^{1}H$ MR protocol as above. The ^{19}F nanoparticles were tagged with DiI as fluorescent marker but the ^{19}F content (5 μmoles PFCE per injection) and size (Z-Average Diam. = 170 nm) was kept constant. Following visualization of ^{19}F signal by $^{19}F/^{1}H$ MRI, we extracted CNS and performed immunohistological staining for macrophages and lymphocytes in CNS regions where the ^{19}F signal was predominant, specifically cerebellum (**Figure 6B**). We observed a main co-localization of DiI-labeled ^{19}F nanoparticles with F4-80$^+$ and Mac-2$^+$cells, indicating that the ^{19}F–DiI nanoparticles are primarily taken up by macrophage-like cells from the periphery into the CNS. However we also observed a co-localization of ^{19}F–DiI with CD4$^+$ T cells in the cerebellum (**Figure 6B**). We also performed FACS of the CNS tissue and secondary lymphoid organs. As expected, we observed a large percentage of CD3$^+$ T cells, CD19$^+$ B cells as well as CD11c$^+$ and CD11b$^+$ myeloid cells in the CNS; most of the latter CD11c$^+$ and CD11b$^+$ cells were sequestered from the draining lymph nodes (**Supplementary Figure 2** *left panel: no DiI-labeled 19F nanoparticles*). Also with FACS, we observed that CD11c$^+$ (30%) and CD11b$^+$ (42%) myeloid cells are the predominant immune cells types that transport the ^{19}F–DiI nanoparticles in the CNS (**Supplementary Figure 2,** *right panel: DiI-labeled 19F nanoparticles*). Interestingly, CD3$^+$ T cells and CD19$^+$ B cells, although present in large quantities, take up a small amount of the ^{19}F–DiI nanoparticles in the CNS and therefore do not contribute significantly to the ^{19}F MR signal we observe in the CNS *in vivo*. In contrast 7% of CD3$^+$ T cells and 41% of CD19$^+$ B cells were labeled with ^{19}F–DiI nanoparticles in the draining lymph nodes and therefore appear to contribute to the ^{19}F MR signal we observed in the lymph nodes *in vivo*. More detailed *ex vivo* and *in vivo* longitudinal studies will help further identify the rich dynamics of the different immune cell populations that serve as communicating envoys between immune system and CNS during encephalomyelitis.

Discussion

The main motivation for constructing the dual-tunable $^{19}F/^{1}H$ RF birdcage probe for brain imaging was to increase the sensitivity required to non-invasively follow immune cells in the CNS during inflammation with MRI. The potential applications for ^{19}F in MRI and MR spectroscopy (MRS) have long been recognized[15,16]. The possibility of employing ^{19}F MRI for tracking cells *in vivo* was however first implemented in the last decade. At present, nanoparticles rich in ^{19}F atoms are employed to study immune cell or stem cell migration *in vivo* with the help of $^{19}F/^{1}H$ MRI[17–22]. However, major challenges particularly signal sensitivity constraints exist. In the present study we prepared nanoparticles (160–170 nm range) from perfluoro-15-crown-5-ether (PFCE) and labeled them with a fluorescent dye (DiI) prior to systemic administration in EAE mice. Thereafter we followed the uptake of the particles by immune cells during the course of the CNS inflammation using the constructed dual-tunable $^{19}F/^{1}H$ birdcage RF head probe.

The geometry chosen for the present $^{19}F/^{1}H$ RF probe was very favorable to boost transmission field homogeneity (B_1^+). Indeed, we showed very encouraging results for mouse neuroimaging. One of the benefits of the highly homogenous transmission field was the significant signal improvement in ventral regions of the CNS, particularly in the brain stem and spinal cord, as well as the draining lymph nodes. These areas are otherwise not easily accessible by conventional commercially-available RF head probes (such as small surface coils or phased-array coils) due to depth penetration constraints. The high degree of cylindrical symmetry as well as the absence of chip capacitors also prevented the manifestation of susceptibility artifacts[23]. The elimination of chip capacitors – as improvement to the original birdcage probe designs – was introduced with the millipede probes[10]. One main advantage of the present 32-leg birdcage probe over the millipede probe is the lower number of legs required due to the shingled design, which makes multiple tuning possible. With the constructed RF probe we achieved a uniform B_1^+ field almost identical for both ^{19}F and ^{1}H channels (3.5% difference in the maximum B_1^+ between both channels in favor of the ^{19}F-channel). The simulations of the ^{1}H channel for the $^{19}F/^{1}H$ dual-tunable resonator were similar to the ones for a single-tuned ^{1}H linear birdcage resonator with the same dimension. The homogeneous field was indispensable to perform spin echo imaging that is sensitive to changes in power and fluctuations in the B_1^+ field[13,14].

From an RF engineering point of view, the quality of the constructed birdcage probe showed a SNR gain with respect to other coil designs with larger diameters and fewer legs, including those for $^{19}F/^{1}H$ mouse body imaging (32 mm diameter, 16 legs)[21] in our lab. The electrical measurements – specifically S Parameters – give a quantitative assessment of the quality of the probe. Probes with a high Q Factor have an improved SNR, considering that $SNR \propto \sqrt{Q}$[9,24]. The Q Factor for the unloaded probe (Q_U) was measured to be 130 and when loaded (Q_L) it was 80 – 110. It should be noted that Q_U decreases with increasing number of legs in a birdcage probe[25]. The Q_{ratio} (Q_L/Q_U) gives an indication of the noise dominance, whether it is from the sample or the probe. It should be ideally smaller than 0.5 in order to achieve predominantly sample noise. However, small probes usually have an increased Q_{ratio} since size is inversely proportional to inductance (L) and directly proportional to resistance (R), according to the formula $Q=(w_0 \cdot L)/R$ (ω_0 = resonance frequency)[26,27]. The Q_{ratio} for the constructed 32 leg probe was calculated to be 0.6 – 0.8. Since the noise contribution for our birdcage probe is predominantly probe dependent ($Q_{ratio} > 0.5$), it was imperative to minimize dielectric losses and coil resistance by using low loss PCB material. Furthermore the design of our birdcage probe – in which plate capacitors were built into its structure – reduced resistance by minimizing the soldering connections required for assembling chip capacitors; added soldering also significantly increases resistive losses in small birdcages[25].

The similarity between ^{19}F and ^{1}H NMR properties is an advantage since the same pulse power settings can be used for both nuclei. After power calibration and adjustments for the ^{1}H channel, the same settings can be applied for the ^{19}F channel. For our birdcage probe we altered the overlapping areas between the copper legs to achieve both frequencies. To fine tune to the ^{1}H (400 MHz) and ^{19}F (376 MHz) frequencies the reflection coefficient for both frequencies needed to be tweaked by altering the distance of the RF shield to the probe. We used a shield diameter of 48 mm to achieve the best results. According to a previous study investigating the shielding effect on field homogeneity, the ratio between $\text{diameter}_{\text{shield}}$ and $\text{diameter}_{\text{coil}}$ should be between 2 and 3; if the shield is closer (ratio < 2) the RF field is disrupted[26]. For the present setup the ratio between $\text{diameter}_{\text{shield}}$ and $\text{diameter}_{\text{coil}}$ was 2.4 for the measurements and final simulations. Indeed the B_1^+ field distributions were homogenous across the cross section of the phantom for both simulations and measurements. The deviation of the measured B_1^+ field over the center slice was calculated to be in the range of 6 – 7%, which made this birdcage particularly suitable for 3D fast spin-echo sequences such as RARE since these are more susceptible to B_1^+ field in homogeneities than gradient echo sequences. A variation in flip angle of less than 10% has no significant influence on spin echo sequences[13,14].

A recognized limitation with our coil design is that the birdcage cannot be driven in quadrature and dual-tunable mode at the same time. Compared to a linear driven birdcage, a quadrature driven coil would add another 41% to SNR gain or reduce the acquisition time to 50% at no cost to SNR. Due to the small size of the coil and space constraints, it is not possible for us (at the current stage) to construct the birdcage in dual-tunable and quadrature driven mode, as has

been shown for human application[28]. Another problem with the quadrature driven mode is the decoupling of the two channels. Potential improvements are to make each channel dual-resonant[29] or to make use of alternate-tuned birdcage elements[11]. Since the proposed design exploits the similarity of proton and fluorine nuclei it might not be possible to apply this technology to low-gamma nuclei.

By using fluorescently-labeled ^{19}F-rich particles we could selectively detect inflammatory cells with ^{19}F/^{1}H MRI and then identify the cell types with the help of fluorescent methods, namely confocal microscopy and flow cytometry. Although the spatial resolution for ^{19}F/^{1}H MRI (μm-range) is not comparable with the high resolution that can be achieved with microscopy (nm-range), it is still possible to study the nature of immune cell infiltration with this technique. Furthermore these experiments can also be done *in vivo* and over a longer period of time; due to the non-invasiveness of the technique it is possible to monitor the migration of immune cells for several days without the necessity of sacrificing the mouse after investigation.

From our study, we could conclude that CD11c^{+} and CD11b^{+} myeloid cells are sequestered from the draining lymph nodes (LN) during early stages of the disease to enter the CNS, predominantly into cerebellum, brain stem and also cerebral cortex. The initial ^{19}F signals detected *in vivo* were mostly located within draining LN; typically the submandibular LN, superficial and deeper cervical LN, facial LN and internal jugular LN. These results further support the significance of the lymphatic system for initiation of CNS inflammation. While the role of the draining lymphatic system on priming immune cells to target the CNS has long been known[30], the kinetics of lymphatic drainage in and out of the CNS is still unclear. In this study we start to uncover some of these dynamics between immune system and CNS with the help of ^{19}F/^{1}H MRI. Further elaborate studies need to be undertaken to study the movement of immune cells into the CNS during encephalomyelitis. While it is appealing to employ ^{19}F/^{1}H MRI to study the impact of the immune system on the development of CNS injury during autoimmune encephalomyelitis, it would be also very interesting to employ ^{19}F/^{1}H MRI to study the impact of neuronal damage or degeneration on the outcome of lymphatic drainage. Recently, light has been shed upon the route taken – namely the cribriform plate– by myeloid cells from the site of neuronal injury to the draining cervical LN[31]. These results favor the application of *in vivo* non-invasive approaches such as ^{19}F/^{1}H MRI to monitor the trafficking of immune cells real-time after traumatic injury[32].

In summary, we developed a birdcage RF probe for ^{19}F/^{1}H neuroimaging with a design that promotes signal to noise ratio, a symmetrical cylindrical geometry, a high filling factor and a homogeneous B_1^+-transmit field. The first *in vivo* experiments performed in EAE mice using ^{19}F/^{1}H MRI are promising in that we are in a position to non-invasively follow the kinetics of inflammation specifically due to the near-to-complete absence of ^{19}F in living tissue. Further experiments with ^{19}F/^{1}H MRI in autoimmune encephalomyelitis and also neurodegenerative disorders are warranted to further understand the communication channels between CNS and the immune system.

Methods

Electromagnetic field simulations and probe design. Prior to construction, various probe designs were simulated with Microwave Studio (MWS) (CST, Darmstadt; Germany) and Penn State Birdcage Builder (BB)[33]. After analysis of the EMF simulation results, a 32-leg low pass (LP) probe design was chosen. The details and dimensions for the simulation were chosen as close as possible to the desired birdcage size: diameter = 18.4 mm, total length = 39 mm, leg width = 1 mm, leg length = 33 mm, end ring width = 3 mm, RF shield diameter = 58 mm. Since the capacitance values required for the construction estimated from Birdcage Builder were very small (e.g. for ^{1}H (400 MHz) C = 1.17 pF), it was not possible to design such a birdcage using chip capacitors. Thus we chose to build the capacitors into the structure of the RF probe by preparing copper strips milled on either side of a double sided copper clad PCB (printed circuit-board) with an area of overlap in between. Figure 1A shows a sketch of the 32-leg ^{19}F/^{1}H LP birdcage design, which was then simulated in MWS. On each side of the PCB, copper strips were arranged in a way to overlap only a few mm depending on the capacitance and thus frequency required. The long inner copper strips (shown in black) overlap with the outer peripheral copper strips (shown in white) that are connected together by the end rings. We first calculated the overlap required to achieve a basic birdcage frequency (birdcage mode) of 388 MHz (frequency midway between the ^{19}F and ^{1}H frequency). According to the Birdcage Builder this basic frequency necessitates a capacitance of 1.38 pF. To calculate the area of overlap between the strips required in order to achieve the necessary capacitance (C), we used the formula for plate capacitors:

$$C = \varepsilon_0 \cdot \varepsilon_r \cdot A/d$$

where ε_0 = vacuum permittivity constant (8.85418*10^{-12} F/m), A = area of overlap, d = thickness of the PCB that corresponds to the distance between the overlapping strips. For the ensuing probe construction we opted for a special flexible PCB with a high relative permittivity ($\varepsilon_r \approx 10$) and a thickness of 400 μm. Using these values, a capacitance of 0.22 pF is achieved per mm^2 overlap. For the basic frequency of 388 MHz (1.38 pF), we calculated an overlapping area of 6.27 mm^2 and applied this for 28 strips. We then degenerated the basic frequency mode symmetrically to achieve the desired ^{1}H and ^{19}F modes. For the ^{1}H mode, 2 strips were overlapped by an area of 3.14 mm^2 to tune to 400 MHz and for the ^{19}F mode, 2 strips were overlapped by an area of 9.39 mm^2 to tune to 376 MHz. Figure 1B shows a circuit diagram displaying the distribution of all capacitors built into the structure of the RF probe and the corresponding ports.

To construct the 32-leg LP head RF probe, we employed a CNC (computer numerical control) machine Protomat S100 (LPKF, Garbsen, Germany) to mill the 32 copper strips on the PCB cladded with 18 μm copper on both sides (thickness = 400 μm; Taconic CER-10). The PCB is made of low loss material (dissipation factor at 400 MHz tanδ = 0.0025) and has a high permittivity ($\varepsilon_r \approx 10$). Relying on the simulations and calculations, 28 strips were overlapped by 6.27 mm^2 to achieve a capacitance of 1.38 pF and therefore a basic frequency of 388 MHz. For the ^{1}H mode (port 1, marked with * in **Figure 1A**) the overlap was reduced by 3.13 mm^2 to 3.14 mm^2 (C1 = 0.69pF) and for the ^{19}F mode (port 2, marked with **) the overlap was increased by 3.12 mm^2 to 9.39 mm^2 (C2 = 2.08 pF). For fine-tuning the shield diameter was reduced stepwise from 58 mm to 48 mm. Furthermore for load-dependent tuning (C1t and C2t) and matching (C1m and C2m) four small trimmer-capacitors (1-10pF) were used. Figure 2A shows the constructed birdcage RF probe. The dimensions of the RF probe are as follows: outer diameter = 20.42 mm; inner diameter of head probe = 16 mm, total length = 43.29 mm, width of each strip = 1.11 mm, length of each leg = 36.63 mm, width of end rings = 3.33 mm, diameter of RF shield (not shown) = 48 mm. All parts for the housing of the 32-leg LP head RF probe were designed using Autodesk Inventor 2011 (Autodesk Inc., San Rafael, CA, USA) and built with a 3D Printer BST 1200es (Dimension Inc., Eden Prairie, MN, USA). The RF performance of the head RF probe – including the measurement of the full set of scattering parameters (S-parameter) that determine the reflection coefficients as well as coupling between the two ports (**Figure 1D**) – was tested with a 2channel vector network analyzer (Rhode & Schwarz GmbH & Co. KG, Memmingen, Germany).

To block unwanted coaxial shield currents, we used baluns on each channel connected as close as possible to the birdcage probe. The baluns were built from semi-rigid cable (diameter 1.5 mm), bent into a loop with a radius of 7.5 mm and soldered on a small piece of printed circuit board. Two 3 mm chip capacitors in the range of 2.2 pF–2.7 pF were used to tune the baluns to 376 MHz and 400 MHz.

B_1^+ simulations and measurements. For B_1^+ simulations we applied a 3D model using MWS (**Figure 2A**) in which a 15-ml Falcon tube (conductivity: σ = 0.33 S/m, relative permittivity: ε = 78) was used as phantom for loading the RF probe; we simulated the load an average mouse head would add to the probe. The transmit-active component (B_1^+) of RF probes can be measured by several flip-angle mapping techniques[34]. For B_1^+ measurements, the probe was loaded with a 15 ml tube filled with saline solution doped with $CuSO_4$ (0.3 g/L) to decrease the T_1 relaxation time to c. 600 ms. This diminishes T_1 related effects and thus reduces measurement time. For the phantom measurements, we applied a time-consuming but simple and accurate technique based on a set of rectangular non-selective preparation pulses (pulse length = 1 ms) followed by spoiler gradients to destroy any transversal magnetization[35]. This way a 3D distribution of longitudinal magnetization (M_z) was produced for the whole volume of interest with 7 different power settings for the preparation pulses. After each preparation step, the M_z-distribution of a central slice was mapped, using a standard 2D gradient-echo sequence with a small flip-angle and long TR (TR min. 5*T_1 = 3 s) to avoid T_1-related effects: TR = 3000 ms, TE = 6 ms, slice thickness 1 mm, FOV = (15 × 15) mm^2, Matrix 64 × 64, NEX = 1, 7 preparation pulses (attenuators = 150 dB, 56.4 dB, 44.4 dB, 39.5 dB, 36.4 dB, 32.3 dB, 31.3 dB), scan time = 35 min.

Preparation of ^{19}F-rich DiI-labeled nanoparticles. For the ensuing *in vivo* ^{19}F/^{1}H MRI in EAE mice and post fixation experiments (histology and flow cytometry), we prepared nanoparticles with high fluorine (^{19}F) content and DiI fluorescence, respectively. These particles consisted of 600 mM perfluoro-15-crown-5-ether (PFCE, Fluorochem, Derbyshire, UK) and 630 μM 1,1'-Dioctadecyl-3,3,3',3'-Tetramethyl, indocarbocyanine Perchlorate (DiI, Molecular Probes®, Invitrogen, Darmstadt, Germany) and were prepared by first emulsifying PFCE in Pluronic F-68 (Sigma-Aldrich, Germany) via direct sonication, using a cell disrupting titanium sonotrode (Bandelin Sonopuls GM70, Bandelin, Berlin, Germany) as previously

described[21]. After 1 : 1 (v/v) dilution with DPBS, the PFCE emulsion was further sonicated in the presence of 630 μM DiI to obtain a PFCE-DiI nanoparticle emulsion containing 600 mM PFCE. In order to remove free DiI, the PFCE-DiI nanoparticle emulsion was then clarified on Sephadex G-50 (Sigma-Aldrich, Germany) columns. The average nanoparticle diameter was determined by dynamic light scattering using a Malvern Zetasizer Nano ZS instrument (Malvern Instruments, Worcestershire, UK). The particle size remained constant after incorporation of the DiI.

***In vitro* experiments.** To determine the uptake capacity for the prepared particles, and optimize the ^{19}F and DiI content, we labeled bone marrow derived dendritic cells (BMDC) with the PFCE-DiI nanoparticles. BMDC were prepared from BM suspensions as previously described[26]. Briefly, BM from femurs of C57BL/6 mice were grown in RPMI-1640 medium containing 10% FCS (Biochrom, Germany) and supplemented with 100 ng/ml of GM-CSF.

***In vivo* experiments.** Animal experiments were carried out in accordance to guidelines provided and approved by the Animal Welfare Department of the State Office of Health and Social Affairs Berlin (*LAGeSo*). For active EAE, female SJL/J mice (Janvier SAS, Le Genest-St-Isle, France) were immunized subcutaneously with 250 μg $PLP_{139-151}$ purity >95% (Pepceuticals Ltd., UK) together with Complete Freund's Adjuvant and heat-killed Mycobacterium tuberculosis (H37Ra, Difco). Bordetella pertussis toxin (250 ng; List Biological Laboratories, US) was administered intraperitoneally at days 0 and 2. On each day following immunization mice were weighed and scored as follows: 0, no disease; 1, tail weakness and righting reflex weakness; 2, paraparesis; 3, paraplegia; 4, paraplegia with forelimb weakness or paralysis; 5, moribund or dead animal. Five days following EAE induction, mice were administered with DiI-labeled nanoparticles containing 5 μmol PFCE.

For ^{19}F/^{1}H MRI, EAE mice were anesthetized using a mixture of isofluraneas inhalation narcosis (0.5–1.5%), pressurized air and oxygen shortly before and during the MR session. The mice were positioned prone on the mouse holder of a small animal MR scanner (Bruker Biospin USR 94/20, Bruker Biospin, Ettlingen, Germany) with the head inside the ^{1}H/^{19}F RF probe which was then moved to the isocenter of the magnet. Following acquisition of scout images using 2D FLASH (MRI Software Paravision 5.1, Bruker Biospin, Ettlingen, Germany), the RF head probe was tuned to both ^{1}H and ^{19}F resonance frequency and then matched to the characteristic impedance (50 Ohm) using the tuning monitor of the animal MR scanner. Following automatic system settings including 1st and 2nd order shimming to fine-tune the homogeneity of the magnetic field, we employed a TurboRARE 3D sequence for ^{1}H: TR = 1500 ms, TE = 53 ms, FOV = (40 × 16 × 16) mm^3, Matrix = 320 × 128 × 128, RARE Factor = 16, NEX = 1 (scan time ca. 25 min); for ^{19}F: TR = 1000 ms, TE = 6 ms, FOV = (40 × 16 × 16) mm^3, Matrix = 100 × 40 × 40, zero fill acceleration 2, RARE Factor = 40, NEX = 128 (scan time = 45 min). For overview scans and serving as a reference to the ^{19}F MRS, we used a 2D FLASH protocol for ^{19}F: TR = 15 ms, TE = 3.3 ms, one sagittol 3 mm slice, in-plane resolution (400 × 400) μm^2, NEX = 2048 (scan time = 15 min) and for ^{1}H: TR = 473 ms, TE = 13 ms, 22 slices, inplane resolution (73 × 73) μm^2, NEX = 16 (scan time = 25 min).

For quantification of the ^{19}F content in specified regions of the mouse brain, we employed single voxel spectroscopy (SVS), in particular Point RESolved Spectroscopy (PRESS). For this purpose we placed a (3 × 3 × 3) mm^3 voxel within the region of interest (here cerebellum and cortex) of the mouse-brain (Figure 4). Then we employed the FastMap[37] method from Paravision, for volume specific magnetic field (B_0) shimming. After shimming the spectra where acquired using a PRESS-protocol for ^{19}F MRS: TR = 1500 ms, TE = 11.6 ms, voxelsize (3 × 3 × 3) mm^3, NEX512 (scan time = 13 min). To quantify the ^{19}F signal we acquired a ^{19}F MRS calibration curve using the same PRESS protocol with three 15 ml Falcon tubes containing different concentrations of our PFCE Emulsion (10, 20 and 40 mM).

Post fixation experiments. For histological and immunohistochemistry investigations, EAE mice were transcardially perfused with 20 ml cold PBS following terminal anesthesia. Thereafter, perfusion was continued with 20 ml cold PFA (4% in PBS). Brain, spinal cord and secondary lymphoid organs were then extracted and subsequently post-fixed overnight in 4% PFA at 4°C. The tissue was then cryoprotected with sucrose (30% in PBS) at 4°C, sectioned in 50 μm thick slices on a cryostat at −20°C and processed on the same day. Free floating sections were washed and incubated with antibodies against Mac2 (ACRIS GmbH, Herford, Germany), CD4 (BD Pharmingen, Heidelberg, Germany), CD3 (Serotec, Düsseldorf, Germany), F4-80 (Biolegend, Fell, Germany) and MPO (Abcam, Cambridge, UK) overnight at 4°C, thereafter washed in PBS and incubated with secondary antibodies conjugated with Cy3 (Jackson, West Grove, Pennsylvania, USA) for 2 h at room temperature. Some sections were incubated with FITC-conjugated B220 (Biolegend, Fell, Germany). After antibody incubations, sections were mounted on standard glass slides and covered with Vectashield-DAPI (Vector Laboratories, Burlingame, California, USA) for fluorescence microscopy. Microphotographs were acquired using a fluorescence microscope (BZ-9000, Keyence, Neu-Isenburg, Germany).

For *flow cytometry* (FACS) experiments, mice were transcardially perfused with 20 ml cold PBS following terminal anesthesia. After extraction, organs (brain, spinal cord, lymph nodes, spleen) were mechanically dissociated through a 70 μm nylon cell strainer (BD Falcon, Heidelberg, Germany) into RPMI medium (containing 5% FCS) and centrifuged at 4°C. To remove contaminating erythrocytes from the dissociated tissue, a lysis buffer was employed. For the CNS, cells were separated from myelin and debris using a 37% Percoll gradient (1.125–1.135 g/ml; Sigma-Aldrich, Germany). The resulting cells were incubated with anti-CD16/32 Fc-receptor block (BD Pharmingen™, Heidelberg, Germany) for 15 min, washed in FACS buffer and prepared for FACS surface staining with APC-conjugated CD3, FITC-conjugated CD19, Pacific Blue-conjugated CD11b and APC-conjugated CD11c antibodies (eBioscience, Frankfurt, Germany).

For *electron microscopy*, mice underwent terminal anesthesia and were transcardially perfused with 4% formaldehyde and 0.5% glutaraldehyde prior to brain extraction. A 3 mm^3 cube (enclosing the PRESS-voxel used for spectroscopy) was dissected from cerebellum and post-fixed (for 24 h in 2% gluteraldehyde, thereafter for 4 h in 1% osmium tetroxide). Following dehydration, tissue was embedded in Poly/Bed 812 (Polysciences, Eppelheim, Germany). Semithin sections were stained with toluidine blue and ultrathin sections were stained with uranyl acetate/lead citrate. Sections were imaged using a FEI Morgagni electron microscope (FEI, Eindhoven, NL) and the iTEM software (Olympus-SIS, Münster, Germany).

1. Charil, A. & Filippi, M. Inflammatory demyelination and neurodegeneration in early multiple sclerosis. *J. Neurol. Sci.* **259**, 7–15 (2007).
2. Trapp, B. D. & Nave, K.-A. Multiple sclerosis: an immune or neurodegenerative disorder? *Annu. Rev. Neurosci.* **31**, 247–69 (2008).
3. Stadelmann, C. Multiple sclerosis as a neurodegenerative disease: pathology, mechanisms and therapeutic implications. *Curr. Opin. Neurol.* **24**, 224–9 (2011).
4. Dousset, V., Gomez, C., Petry, K. G., Delalande, C. & Caille, J. M. Dose and scanning delay using USPIO for central nervous system macrophage imaging. *Magma* **8**, 185–9 (1999).
5. Floris, S. *et al.* Blood-brain barrier permeability and monocyte infiltration in experimental allergic encephalomyelitis: a quantitative MRI study. *Brain* **127**, 616–27 (2004).
6. Tysiak, E. *et al.* Beyond blood brain barrier breakdown – in vivo detection of occult neuroinflammatory foci by magnetic nanoparticles in high field MRI. *J. Neuroinflamm.* **6**, 20 (2009).
7. Oude Engberink, R. D. *et al.* Dynamics and fate of USPIO in the central nervous system in experimental autoimmune encephalomyelitis. *NMR Biomed.* **23**, 1087–96 (2010).
8. Ruiz-Cabello, J., Barnett, B. P., Bottomley, P. a. & Bulte, J. W. M. Fluorine ((19)F) MRS and MRI in biomedicine. *NMR Biomed.* (2010).
9. Hoult, D. & Richards, R. The signal-to-noise ratio of the nuclear magnetic resonance experiment. *J. Magn. Reson.* **24**, 71–85 (1976).
10. Wong Ernest, W. H. Millipede Coils. *Encycl. Magn. Reson.* (2007).
11. Tomanek, B., Volotovskyy, V., Gruwel, M. L. H., McKenzie, E. & King, S. B. Double-frequency birdcage volume coils for 4.7T and 7T. *Concept. Magn. Reson. B* **26B**, 16–22 (2005).
12. Waiczies, H. *et al.* Identification of Cellular Infiltrates during Early Stages of Brain Inflammation with Magnetic Resonance Microscopy. *PLoS ONE* **7**, e32796 (2012).
13. Hornak, J. P., Szumowski, J. & Bryant, R. G. Magnetic field mapping. *Magn. Reson. Med.* **6**, 158–63 (1988).
14. Dowell, N. G. & Tofts, P. S. Fast, accurate, and precise mapping of the RF field in vivo using the 180 degrees signal null. *Magn. Reson. Med.* **58**, 622–30 (2007).
15. Holland, G. N. & Hinshaw, P. A. B. W. S. Communications 19F Magnetic Resonance Imaging. *J. Magn. Reson.* **136**, 133–136 (1977).
16. Liu, M. S. & Long, D. M. Perfluorooctylbromide as a diagnostic contrast medium in gastroenterography. *Radiology* **122**, 71–6 (1977).
17. Ahrens, E. T., Flores, R., Xu, H. & Morel, P. a In vivo imaging platform for tracking immunotherapeutic cells. *Nat. Biotechnol.* **23**, 983–7 (2005).
18. Srinivas, M., Morel, P. a., Ernst, L. A., Laidlaw, D. H. & Ahrens, E. T. Fluorine-19 MRI for visualization and quantification of cell migration in a diabetes model. *Magn. Reson. Med.* **58**, 725–34 (2007).
19. Partlow, K. C. *et al.* 19F magnetic resonance imaging for stem/progenitor cell tracking with multiple unique perfluorocarbon nanobeacons. *FASEB J.* **21**, 1647–54 (2007).
20. Srinivas, M. *et al.* In vivo cytometry of antigen-specific t cells using 19F MRI. *Magn. Reson. Med.* **62**, 747–53 (2009).
21. Waiczies, H. *et al.* Perfluorocarbon particle size influences magnetic resonance signal and immunological properties of dendritic cells. *PloS one* **6**, e21981 (2011).
22. Srinivas, M., Boehm-Sturm, P., Figdor, C. G., De Vries, I. J. & Hoehn, M. Labeling cells for in vivo tracking using 19F MRI. *Biomaterials* (2012).
23. Doty, F. D., Entzminger, G., Kulkarni, J., Pamarthy, K. & Staab, J. P. Radio frequency coil technology for small-animal MRI. *NMR Biomed.* **20**, 304–25 (2007).
24. Hill, H. D. W. & Richards, R. E. Limits of measurement in magnetic resonance. *J. Phys. E Sci. Instrum.* **1**, 977–983 (1968).
25. Crozier, S., Luescher, K., Forbes, L. K. & Doddrell, D. M. Optimized Small-Bore, High-Pass Resonator Designs. *Magn. Reson. Med., Series B* **109**, 1–11 (1995).
26. Mispelter, J. & Lupu, M. Homogeneous resonators for magnetic resonance: A review. *C. R. Chim.* **11**, 340–355 (2008).
27. Giovannetti, G., Hartwig, V., Landini, L. & Santarelli, M. F. Low-Field MR Coils: Comparison between Strip and Wire Conductors. *Appl. Magn. Reson.* **39**, 391–399 (2010).
28. Shen, G. X., Wu, J. F., Boada, F. E. & Thulborn, K. R. Experimentally verified, theoretical design of dual-tuned, low-pass birdcage radiofrequency resonators for magnetic resonance imaging and magnetic resonance spectroscopy of human brain at 3.0 Tesla. *Magn. Reson. Med.* **41**, 268–75 (1999).

29. Hu, L. *et al.* A generalized strategy for designing (19)F/(1)H dual-frequency MRI coil for small animal imaging at 4.7 Tesla. *J. Magn. Reson. Im.* **34**, 245–52 (2011).
30. Phillips, M. J., Needham, M. & Weller, R. O. Role of cervical lymph nodes in autoimmune encephalomyelitis in the Lewis rat. *J. Pathol.* **182**, 457–64 (1997).
31. Kaminski, M. *et al.* Migration of monocytes after intracerebral injection at entorhinal cortex lesion site. *J. Leukocyte. Biol.* **92**, 31–9 (2012).
32. Laman, J. D. & Weller, R. O. Editorial: route by which monocytes leave the brain is revealed. *J. Leukocyte. Biol.* **92**, 6–9 (2012).
33. Chin, C.-L., Collins, C. M., Li, S., Dardzinski, B. J. & Smith, M. B. BirdcageBuilder: Design of specified-geometry birdcage coils with desired current pattern and resonant frequency. *Concept. Magnetic. Res.* **15**, 156–163 (2002).
34. Jiru, F. & Klose, U. Fast 3D radiofrequency field mapping using echo-planar imaging. *Magn. Reson. Med.* **56**, 1375–9 (2006).
35. Seifert, F., Wübbeler, G., Junge, S., Ittermann, B. & Rinneberg, H. Patient safety concept for multichannel transmit coils. *J. Magn. Reson. Im.* **26**, 1315–21 (2007).
36. Bendix, I. *et al.* MAPK3 deficiency drives autoimmunity via DC arming. *Eur. J. Immunol.* **40**, 1486–95 (2010).
37. Gruetter, R. Automatic, localizedin Vivo adjustment of all first-and second-order shim coils. *Magn. Reson. Med.* **29**, 804–811 (1993).

Acknowledgments

This study was funded by the Deutsche Forschungsgemeinschaft to S.W. (DFG WA 2804) and a university grant to S.W. from the Experimental and Clinical Research Center, a cooperation of the Max Delbrück Center for Molecular Medicine and Charité Medical Faculty in Berlin. The funders had no role in study design, data collection and analysis, decision to publish, or preparation of the manuscript. We thank Ms. Julia Skodowski and Ms. Rita Geppert for technical support.

Author contributions

H.W., T.N. and S.W. conceived and designed the study. H.W., S.L., F.Q., B.P., A.P. and S.W. carried out the experiments and measurements. HW and WH developed the RF-Probe. A.K. and T.L. helped with EMF simulations and B_1^+ - mapping. S.D., S.W., K.S. and M.D. developed the ^{19}F/DiI-nanoparticles. S.W., H.W. and T.N. wrote the manuscript with the assistance of all other co-authors.

Additional information

Supplementary information accompanies this paper at http://www.nature.com/scientificreports

Competing financial interests: The authors declare no competing financial interests.

How to cite this article: Waiczies, H. *et al.* Visualizing Brain Inflammation with a Shingled-Leg Radio-Frequency Head Probe for ^{19}F/^{1}H MRI. *Sci. Rep.* **3**, 1280; DOI:10.1038/srep01280 (2013).

Curriculm Vitae

My curriculum vitae will not be published in the electronic version of my work for privacy reasons.

My curriculum vitae will not be published in the electronic version of my work for privacy reasons.

My curriculum vitae will not be published in the electronic version of my work for privacy reasons.

Complete list of publications

1. **Anchoring Dipalmitoyl Phosphoethanolamine to Nanoparticles Boost Cellular Uptake and Fluorine-19 Magnetic Resonance Signal**
   Waiczies S, Lepore S, Sydow K, Drechsler S, Ku MC, Martin C, Lorenz D, Schütz I, Reimann HM, Purfürst B, Dieringer MA, Waiczies H, Dathe M, Pohlmann A, Niendorf T;
   Scientific Reports, under review.

2. **Differential effect of Orexin-1 and CRF-1 antagonism on stress circuits: a fMRI study in the rat with the pharmacological stressor yohimibine.**
   Gozzi A, Lepore S, Vicentini E, Merlo-Pich E, Bifone A;
   Neuropsychopharmacology 2013 Oct;38(11):2120-30.

3. **Enlargement of cerebral ventricles as an early indicator of encephalomyelitis.**
   Lepore S, Waiczies H, Hentschel J. Yi J, Skodowski J, Pohlmann A, Millward JM, Paul F, Wuerfel J, Niendorf T, Waiczies S;
   PLoS One. 2013 Aug 22;8(8):e72841.

4. **Monitoring Dendritic Cell Migration using 19F / 1H Magnetic Resonance Imaging.**
   Waiczies H, Guenther M, Skodowski J, Lepore S, Andreas Pohlmann A, Niendorf T, Waiczies S;
   J. Vis. Exp. 2013 Mar 20; 73: e50251.

5. **Visualizing brain inflammation with a shingled-leg radio-frequency head probe for $^{19}F/^{1}H$ MRI.**
   Waiczies H, Lepore S, Drechsler S, Qadri F, Purfürst B, Sydow K, Dathe M, Kühne A, Lindel T, Hoffmann W, Pohlmann A, Niendorf T, Waiczies S;
   Sci Rep. 2013 Feb 15;3:1280.

6. **Identification of cellular infiltrates during early stages of brain inflammation with magnetic resonance microscopy.**

Waiczies H, Millward JM, Lepore S, Infante-Duarte C, Pohlmann A, Niendorf T, Waiczies S;
PLoS One. 2012;7(3):e32796. Epub 2012 Mar 12.

7. **Perfluorocarbon particle size influences magnetic resonance signal and immunological properties of dendritic cells.**
Waiczies H, Lepore S, Janitzek N, Hagen U, Seifert F, Ittermann B, Purfürst B, Pezzuto A, Paul F, Niendorf T, Waiczies S;
PLoS One. 2011;6(7):e21981. Epub 2011 Jul 19.

8. **GSK1614343, a Novel Ghrelin Receptor Antagonist, Produces an Unexpected Increase of Food Intake and Body Weight in Rodents and Dogs.**
Costantini VJ, Vicentini E, Sabbatini FM, Valerio E, Lepore S, Tessari M, Sartori M, Michielin F, Melotto S, Bifone A, Pich EM, Corsi M;
Neuroendocrinology. 2011;94(2):158-68. Epub 2011 Jul 22.

9. **Neuroimaging Evidence of Altered Fronto-Cortical and Striatal Function after Prolonged Cocaine Self-Administration in the Rat.**
Gozzi A, Tessari M, Dacome L, Agosta F, Lepore S, Lanzoni A, Cristofori P, Pich EM, Corsi M, Bifone A.;
Neuropsychopharmacology. 2011 Nov;26(12):2431-40.

International conferences

Joint ESMRMB-ISMRM 2014 Annual Meeting, Milan, Italy

- **Influence of phospholipid enriched ^{19}F nanoparticles on fluorine uptake in dendritic cells**
  Lepore S, Sydow K, Drechsler S, Ku MC, Waiczies H, Martin C, Schuetz I, Purfürst B,Dathe M, Niendorf T, Waiczies S.
- **Quantification of Dendritic Cells entering the Lymph Nodes in Mice using ^{19}F MRI**
  Martin C, Ku MC, Lepore S, Waiczies H, Pohlmann A, Hentschel J, Dieringer MA, Niendorf T, Waiczies S.
- **^{19}F MRI for Evaluating ERK1 as a Factor Regulating Dendritic Cell Migration in High Grade Glioma**
  Ku MC, Guenther M, Martin C, Lepore S, Waiczies H, Pohlmann A, Wolf SA, Kettenmann H, Niendorf T, Waiczies S.

ISMRM 2012 Annual Meeting, Melbourne, Autralia

- **Pre-Symptomatic Cerebellar Lesions and Ventricle Enlargement in an EAE Mouse Model Revealed by Microscopic MRI.**
  Lepore S, Waiczies H ,Hentschel J, Millward JM, Infante-Duarte C, Niendorf T, Waiczies S.
- **^{19}F/^{1}H MRI of Brain Inflammation in Experimental Autoimmune Encephalomyelitis**
  Waiczies H, Lepore S, Millward JM, Purfürst B, Niendorf T, Waiczies S.

ESMRMB 2011 Annual Scientific Meeting, Leipzig, Germany

- **Magnetic resonance microscopy reveals pre-symptomatic brain modification in a murine EAE model.** *Lepore S, Waiczies H, Millward JM, Infante-Duarte C, Paul F, Niendorf T, Waiczies S.*

Acknowledgments

I would like to thank my supervisor Prof. Dr. Thoralf Niendorf for his motivational support and inspiration for the accomplishment of this thesis.

I would like to thank particularly Dr. Sonia Waiczies that in all these years has always believed in my skill even when I was doubtful and she is at the basis of my education and personal growth that brought me this far.

I thank the entire team of the Berlin Ultrahigh Field Facility and especially Helmar who taught me to be independent in my experiments, Jason who demonstrated me what means passion for research, Jan for his friendship and his helpful suggestions and our long conversations about our research projects and Sabrina for her help with German language and bureaucracy.

Finally, I thank my family that, although I was far away, has always encouraged me and they never made me feel lonely.